Low-dose computational phase contrast transmission electron microscopy via electron ptychography

Dissertation
zur Erlangung des Doktorgrades
an der Fakultät für Mathematik, Informatik und Naturwissenschaften
Fachbereich Physik
der Universität Hamburg

vorgelegt von

Philipp M. Pelz

Hamburg

2018

Gutachter der Dissertation:	Prof. Dr. Dr. h.c. R. J. Dwayne Miller Prof. Dr. Dr. h.c. Henry Chapman
Zusammensetzung der Prüfungskommission:	Prof. Dr. Robin Santra Prof. Dr. Dr. h.c. R.J. Dwayne Miller Prof. Dr. Dr. h.c. Henry Chapman Prof. Dr. Christian Schroer Dr. Robert Bücker
Vorsitzender der Prüfungskommission	Prof. Dr. Robin Santra
Datum der Disputation	7.12.2018
Vorsitzender des Fach-: Promotionsausschusses PHYSIK	Prof. Dr. Wolfgang Hansen
Leiter des Fachbereichs Physik	Prof. Dr. Michael Potthoff
Dekan der Fakultät MIN	Prof. Dr. Heinrich Graener

Eidesstattliche Versicherung / Declaration on oath

Hiermit versichere ich an Eides statt, die vorliegende Dissertationsschrift selbst verfasst und keine anderen als die angegebenen Hilfsmittel und Quellen benutzt zu haben.

Die eingereichte schriftliche Fassung entspricht der auf dem elektronischen Speichermedium. Die Dissertation wurde in der vorgelegten oder einer ähnlichen Form nicht schon einmal in einem früheren Promotionsverfahren angenommen oder als ungenügend beurteilt.

Hamburg, den   Philipp Pelz

Low-dose computational phase contrast transmission electron microscopy via electron ptychography

Abstract

In the recent years, cryo-electron microscopy (cryo-EM) has evolved into a mainstream technique to decipher the structure-function relationship of biological specimens from single molecules to whole cells. Cryo-EM relies on the strong interaction of high-energy electrons with matter, which causes a measurable phase shift of the electron wave even for single small macromolecules. Experimental methods to measure this phase shift effectively are therefore the key to obtaining higher spatial resolution images or even movies before radiation damage destroys the molecule, yet current phase contrast methods suffer several limitations for biological electron microscopy. They are either impractical to implement, do not allow to deconvolve the influence of microscope optics from the image, or involve inelastic scattering events after the electron wave has passed the sample, which scramble the acquired phase information.

Ptychography creates a high-dimensional phase space map of the imaging process by scanning a spatially confined coherent wavefront over the sample and collecting a two-dimensional far-field diffraction pattern at each position. Both the complex-valued transmission function of the sample and the wave function of the incoming beam can be recovered from this dataset through deconvolution in phase space with a range of reconstruction methods.

Electron ptychography is easy to implement in a transmission electron microscope TEM but has so far only been applied to phase contrast imaging of samples in the field of materials science because of the high dose required for the reconstruction of a ptychographic dataset and the resulting high requirements on the sample for radiation damage tolerance. We propose the use of non-convex Bayesian optimization to overcome this limitation, and show via numerical simulations that one can reduce the dose required for successful ptychographic reconstruction by two orders of magnitude compared to previous experiments. This opens up the field of biological electron microscopy for computational phase contrast imaging via electron ptychography.

Using multi-slice simulations and our Bayesian reconstruction algorithm, we demonstrate imaging of single biological macromolecules and show 2D single-particle reconstructions from simulated data with a resolution up to 5.4 Å at a dose of $20\,e^-/\text{Å}^2$. When averaging 30 low-dose datasets, a 2D resolution around

3.5 Å is possible for macromolecular complexes with molecular weight even below 100 kDa.

Further, we present the open-source framework `scikit-pr`, a GPU-accelerated implementation of the proposed Bayesian algorithm based on the open-source neural network library `pytorch`. Through the use of *automatic differentiation*, `scikit-pr` allows the expression of the image formation process with a differentiable computational graph and makes it easy to exchange experimental forward models, loss functions, and optimization algorithms in a plug-and-play fashion.

We then discuss the practical aspects and technical requirements for implementing low-dose electron ptychography in a TEM. We show two proof-of-principle reconstructions from datasets collected on two different microscopes and detectors: one of a benchmark carbon sample obtained on a Titan Krios with a K2 Summit camera at a dose of $50\,e^-/\mathring{A}^2$, and one of horse-spleen apo-ferritin proteins obtained on a Tecnai F20 with a Medipix3 camera at a dose of $30\,e^-/\mathring{A}^2$.

Subsequently, we describe how the information contained in the ptychographic data set can be optimized by tailoring the illumination wavefront and show first results of creating a diffuse, speckled beam for electron ptychography by using a nanostructured mask in the condenser plane of a TEM.

We highlight several avenues of further investigations based on the developed methods in the conclusion: the possibility of measurement of additional incoherent signals, like energy-dispersive X-ray and annular dark field information, during a ptychography scan, the application of quantum tomography schemes to optimize the information content of the measurements and quantum state reconstruction from inelastic scattering processes.

Computergestützte Phasenkontrast-Elektronenmikroskopie bei niedrigen Dosen via Elektronen-Ptychographie

Kurzzusammenfassung

In den letzten Jahren hat sich Cryo-Elektronenmikroskopie (Cryo-EM) zu einer etablierten Technik entwickelt, um die Struktur-Funktions-Beziehung von biologischen Proben von einzelnen Molekülen zu ganzen Zellen zu entschlüsseln. Cryo-EM beruht auf der starken Wechselwirkung von hochenergetischen Elektronen mit Materie, die sogar für einzelne kleine Makromoleküle eine messbare Phasenverschiebung der Elektronenwelle bewirkt. Experimentelle Verfahren, um diese Phasenverschiebung effektiv zu messen, sind daher der Schlüssel dazu, um Bilder mit höherer räumlicher Auflösung oder sogar Filme zu erhalten, bevor eine Strahlungsschädigung das Molekül zerstört. Gegenwärtige Phasenkontrastverfahren jedoch unterliegen einigen Beschränkungen für die biologische Elektronenmikroskopie. Sie sind entweder unpraktisch zu implementieren, erlauben nicht, die optische Übertragungsfunktion des Mikroskops von dem Bild zu entfalten, oder involvieren inelastische Streuereignisse, nachdem die Elektronenwelle die Probe passiert hat.

Die Ptychographie erzeugt eine hochdimensionale Phasenraumabbildung des Bildgebungsprozesses durch Abrastern einer räumlich begrenzten kohärenten Wellenfront über die Probe und Aufnahme eines zweidimensionalen Fernfeldbeugungsmusters an jeder Position. Sowohl die komplexwertige Übertragungsfunktion der Probe als auch die Wellenfunktion des ankommenden Strahls können aus diesem Datensatz durch Entfaltung im Phasenraum mit einer Reihe von Rekonstruktionsverfahren wiederhergestellt werden.

Die Elektronenptychographie ist in einem Transmissionselektronenmikroskop (TEM) einfach zu implementieren, wurde aber bisher nur auf die Phasenkontrast-Bildgebung von Proben im Bereich der Materialwissenschaften angewendet, da die für die Rekonstruktion eines ptychographischen Datensatzes erforderliche hohe Dosis hohe Anforderungen an die Probe hinsichtlich der Strahlenschädigungstoleranz stellt. Wir schlagen die Verwendung von nicht-konvexer Bayesscher Optimierung vor, um diese Einschränkung zu überwinden, und zeigen über numerische Simulationen, dass man die für eine erfolgreiche ptychographische Rekonstruktion erforderliche Dosis um zwei Größenordnungen im Vergleich zu früheren Experimenten reduzieren kann. Dies erschließt das Feld der

biologischen Elektronenmikroskopie für die computergestützte Phasenkontrast-Bildgebung mittels Elektronen-Ptychographie.

Mit Multi-Slice-Simulationen und unserem Bayesschen Rekonstruktionsalgorithmus demonstrieren wir die Abbildung einzelner biologischer Makromoleküle und zeigen 2D-Einzelpartikel-Rekonstruktionen aus simulierten Daten mit einer Auflösung von bis zu 5.4 Å bei einer Dosis von $20\,e^-/\text{Å}^2$. Durch Mittelung von 30 niedrig dosierten Datensätzen ist eine 2D-Auflösung um 3.5 Å für makromolekulare Komplexe mit einem Molekulargewicht sogar unter 100 kDa möglich. Außerdem stellen wir das Open-Source-Framework *scikit-pr* vor, eine GPU-beschleunigte Implementierung des Bayesschen Algorithmus basierend auf der Open-Source-Bibliothek `pytorch` für neuronale Netzwerke. Durch die Verwendung von *automatische Differenzierung* ermöglicht *scikit-pr* den Ausdruck des Bilderzeugungsprozesses mit einem differenzierbaren Rechengraphen und erleichtert den Austausch experimenteller Vorwärtsmodelle, Verlustfunktionen und Optimierungsalgorithmen in einem plug-and-play Modus.

Anschließend diskutieren wir die praktischen Aspekte und technischen Voraussetzungen für die Implementierung von Elektronen-Ptychographie mit geringer Dosis in einem TEM. Wir zeigen zwei proof-of-principle Rekonstruktionen an zwei verschiedenen Mikroskopen und Detektoren: eine Rekonstruktion einer Benchmark-Kohlenstoffprobe, die auf einem Titan Krios Mikroskop mit einer K2-Summit-Kamera bei einer Dosis von $50\,e^-/\text{Å}^2$ erhalten wurde, und einer von apo-Ferritin-Proteinen aus der Pferde-Milz, die auf einem Tecnai F20 Mikroskop mit einer Medipix3-Kamera bei einer Dosis von $30\,e^-/\text{Å}^2$ erhalten wurden Anschließend beschreiben wir, wie die im ptychographischen Datensatz enthaltene Information optimiert werden kann, indem die Beleuchtungswellenfront maßgeschneidert wird. Wir zeigen erste Ergebnisse von der Erzeugung eines diffusen, gesprenkelten Strahls für die Elektronenptychographie unter Verwendung einer nanostrukturierten Maske in der Kondensorebene eines Elektronenmikroskops.

Wir heben mehrere Möglichkeiten weiterer Untersuchungen auf der Grundlage der entwickelten Methoden in der Schlussfolgerung hervor: die Möglichkeit der Messung von zusätzlichen inkohärenten Signalen, wie energiedispersiver Röntgen- und ringförmiger Dunkelfeldinformation, während eines Ptychographiescans. Die Anwendung von Quantentomographie-Schemata zur Optimierung des Informationsgehalts der Messungen. Und Quantenzustandsrekonstruktion aus inelastischen Streuprozessen.

Contents

Acknowledgments

I would like to thank all members of the Coherent Electron Imaging and Source Development group for being a good environment to live through all the ups and downs of the Ph.D. life, in particular ...

... Dwayne Miller, for sharing his enthusiasm for science and always encouraging to think big, and giving me the opportunity to explore all ideas I had. I am also very grateful for the freedom that I had, to work where and when I wanted, focusing on results rather on attendance, which made the family life with two little kids so much easier and having kids during the Ph.D. a wonderful experience.

... Robert Bücker, for being my go-to person for discussions about phase space, anything quantum, and for providing the necessary experimental reality checks for all the crazy ideas. Thank you for getting the Tecnai microscope up and running so quickly and accompanying me on all the beam times. Thanks for saving me from being run over on an Australian expressway after long days of experiments.

... Günther Kassier, for always being there for discussion, throwing around ideas about single-shot experiments and helping with the cryo-ptychography experiments at Tecnai microscope in Hamburg.

... Dennis Eggert, for preparing and ordering all the bio-samples for the experiments in Hamburg.

... Michiel de Kock, for helping convert the `scikit-pr` code to Python3 and the new `pytorch` release, and proof-reading my thesis.

... Sebastian Kruber, for being my feel-home Bavarian office mate and friend, helping me through the ups and downs of the thesis.

... Gopal, Lindsay, Sana, Julian, Eike, Pascal, Chiwon, Albert, Salvador, it was always a pleasure to work with you.

I would like to thank the crew at the Ramaciotti Center for Cryo-EM at Monash, where they had the patience to try my experiment, especially ...

... Georg Ramm for organizing the sessions with me, operating the microscope,

and discussing all the options to make it work,

... Hariprasad Venugopal for preparing our cryo-samples at Monash, and discussing about cryo-EM best practices.

I would like to thank the group of Rafal Dunin-Borkowski at the Ernst Ruska-Center in Juelich, especially Penghan Lu, who invested much time in preparing the experiments and discussing the design of the diffuser phase plates for ptychography, and performing experiments in Juelich at the Titan Holo microscope.

I would also like to thank Vincenzo Grillo for advising on the design of the phase plates, and providing his expertise in fabricating them.

I would also like to thank Prof. Pete Nellist and Prof. Angus Kirkland from the University of Oxford for sharing some ptychography data from the JEOL GrandARM at Harwell, and for discussions about low-dose reconstructions.

From the organizational side I would like to thank ...

... the IMPRS-UFAST graduate school for the great curriculum and extracurricular activities, and the mentoring and help with administrative issues, especially Julia Quante.

... Christine Fricke, for helping with letters and signatures.

... Prof. Henry Chapman for reviewing this thesis and being on the committee as one of the pioneers of ptychography and phase retrieval. Thank you for the occasional discussions during the CFEL symposia, they were very helpful for me.

Finally, thank you Tia, Toni and Theo, Jutta, Christiane, Arne-Christian, Jannschi for lovingly supporting me throughout this thesis, and for everything else.

Introduction

The loss of phase information of a wave function due to the measurement process has been identified as an important problem in the early days of quantum mechanics [1]. The question of how one can recover the lost phase most efficiently and uniquely has since occupied many generations of scientists and has spurred advances in many fields of physics.

In 1942 Frits Zernike discovered that the phases could be made to contribute linearly to the measured amplitude by placing a phase-shifting plate in the back-focal plane of a microscope which shifts the phase of the unscattered beam by $\pi/2$ to the scattered beam [2, 3]. This rather simple principle to directly measure phase without any post-processing is used in nearly all fields of microscopy today. Its implementation in the electron microscope however turned out to be nontrivial, and a practical implementation was only achieved recently [4]. Therefore research was also directed to other interference techniques.

In 1948, Dennis Gabor's original idea that the phase may be measured by interfering an undisturbed reference wave and a diffracted wave created the field of holography [5, 6].

While this first, inline holographic setup suffers the so-called twin-image problem, i.e., two conjugate terms forming the interference term need to be separated, soon a large number of different setups emerged which alleviated the problem, facilitating the separation of a unique wave function [7].

Leith & Upatnieks [8, 9] showed in their seminal contribution in 1962 that off-axis holography, i.e., the interference of an off-axis reference-wave with a modulated object wave, resolves the twin-image problem, with the presumptions that the object's spatial frequency spectrum is bandwidth-limited and the experimental requirement of superb coherence of the particle source. In the following decades, off-axis holography evolved into a widely-used technique in the electron microscope. In some cases, however, it is experimentally difficult to provide an undisturbed reference wave, and therefore, researchers developed variations of the original inline scheme of Gabor, which recover the phase from multiple measurements where the defocus is varied. These are usually referred to as focal series inline holography or transport of intensity reconstruction [10].

Around the same time, Walther Hoppe, an X-ray crystallographer turned electron microscopist, was working on the structural analysis of biological macromolecules at the Max Planck Institute for Protein and Leather Research in Dresden. In 1969, he invented yet another method to solve the phase problem [11, 12], which he dubbed ptychography. Initially looking at crystal diffraction, he realized that interference measurements could also be performed by sending a convergent electron beam through the crystal. He observed interference between the diffraction orders of a crystal if the half-convergence angle of the beam was larger than half the scattering angle of the first diffraction peak. While this interference alone is not enough to solve unambiguously for the phase, he realized that one could resolve the ambiguities when the beam is shifted in real space and a diffraction pattern at each shift position is recorded. Unfortunately, the idea was well ahead of instrument development in electron microscopy at that time, and neither the microscopes, nor the cameras, nor the computers were suitable for an experimental demonstration. It slumbered some years without much notice until John Rodenburg realized its potential in 1989 and, together with Richard Bates, extended its applicability to non-periodic samples. They developed a general theory of ptychography, which describes a ptychographic data set as the convolution of the Wigner function of the object and the Wigner function of the beam [13]. The process of phase retrieval is then the deconvolution of these functions in phase space.

This deconvolution process implies the riddance of most instrument-related resolution limitations such as partial coherence and information limits imposed by the lenses, such that the ultimate resolution is only limited by the maximum angle under which diffraction is observed. This super-resolution feature of ptychography was demonstrated soon after by Nellist and Rodenburg [14], and a year later the method was also applied to X-ray microscopy by Chapman [15]. While the first demonstrations of ptychography were very impressive, it was also clear that the detectors were orders of magnitude too slow to record this amount of data quickly enough, and the experimental stability in the electron microscope did not allow stable acquisitions that took tens of minutes. The protagonists moved to other fields, Rodenburg to X-ray and light microscopy, and Nellist to incoherent imaging, waiting for the technology to catch up. Only recently, fast detectors with frame rates in the kHz range have become available, and ptychography is developing into a practical technique for electron microscopy.

As already hinted at by the example of Hoppe, the use of electrons for structural investigations of biological specimens is attractive because of their strong interaction with matter and a favorable ratio of elastic to inelastic scattering events. In the last years, imaging of vitrified biological specimens from single macromolecules to whole cells by cryo-EM has developed into a mainstream technique [16, 17]. Single-particle cryo-EM allows us to reconstruct a three-dimensional atomic potential map from an ensemble of identical particles with resolutions up to 1.6 Å [18]. Until recently, the phase contrast mechanism these reconstructions relied on was provided by aberrations in the imaging system, and therefore the contrast transfer and the information provided by each electron was far from optimal.

It took over 60 years from the initial idea of a Zernike phase plate for electrons in 1947 [19] to a working implementation. Since 2014, the so-called Volta phase plate [4] provides improved phase contrast, so that even particles with molecular weights as small as 64 kDa can be observed in the TEM [20]. While most of the other above mentioned methods for phase recovery described above have been tried and tested for the imaging of biological specimens, electron ptychography has not been considered so far for imaging of biological macromolecules.

This thesis aims to establish electron ptychography as a practical method for low-dose phase contrast imaging of biological macromolecules and therefore close the circle that started with Hoppe. We show via simulations that ptychography in combination with a Bayesian reconstruction algorithm is more dose-efficient than both Zernike phase contrast and conventional defocus-based phase contrast in cryo-EM by achieving two orders of magnitude better signal to noise ratio at high spatial frequencies. This tremendous improvement naturally raises the question of whether there is an optimal phase retrieval technique that extracts the maximum amount of information of each electron.
This question is of particular interest when biological dynamics become the matter of interest, as the sample then needs to withstand enough dose to be able to capture several exposures without significant damage. The application of electron ptychography to liquid phase electron microscopy may, therefore, be particularly promising if the overall thickness requirements for ptychography can be achieved. The structure of this work is as follows:

Chapter 1 treats the physics necessary for the understanding of image formation of biological specimens in cryo-EM. We discuss electron microscope layout (section 1.1), scattering cross sections (section 1.2.1), radiation damage processes (section 1.2.1) and electron propagation through the sample (sections 1.2.2 and 1.2.3). Then we extend the wave function formalism to a full description of arbitrary quantum states (sections 1.2.8 and 1.2.9), show how arbitrary quantum states can be recovered from a set of measurements (section 1.2.11), and relate the original phase retrieval problem for wave functions to this description (section 1.2.12).
We then discuss most of the above mentioned holographic techniques as quantum state reconstruction techniques, describe experimental obstacles for low-dose imaging of biological macromolecules, and the history of the application of the different techniques to biological electron microscopy in section 1.3.

Chapter 2 discusses the a general mathematical description of ptychography in linear algebra terms and the limitations of existing algorithms for ptychographic phase retrieval regarding low-dose imaging (sections 2.1, 2.2). We then introduce a non-convex Bayesian algorithm which recovers phases also at the low doses needed when imaging biological macromolecules and extend it to so-called blind ptychography, which simultaneously recovers the probe function (sections 2.3, 2.4). Section 2.6 then discusses the application to single-particle cryo-EM and compares the algorithm with bright-field TEM and Volta phase-plate TEM. Section 2.7 describes an efficient GPU-accelerated implementation of the algorithm and develops a computational framework for the generalized phase-retrieval problem.

Chapter 3 discusses practical considerations for implementing low-dose electron ptychography in a scanning transmission electron microscope (STEM). We discuss the necessary equipment (3.1.1), the sample thickness limits (3.1.2), sampling considerations (3.1.3), reconstruction ambiguities (3.1.4), the choice of detectors (3.1.5), data preprocessing strategies (3.1.6), and show two proof-of-principle experiments. Section 3.3 discusses electron ptychography on a Titan Krios microscope with a K2 camera and section 3.4 discusses electron ptychography on a Tecnai F20 microscope with a Medipix3 camera.

Chapter 4 makes the point that introducing a strongly varying local phase structure in the probe wave function leads to reconstruction with higher signal-to-noise ratio (section 4.1), and discusses the design of phase masks that can be placed in the condenser aperture of a microscope to create structured illumination in the STEM (section 4.2). We show a first attempt at performing low-dose ptychography with such a diffuser and discuss experimental difficulties (section 4.3).

Chapter 5 summarizes the findings and discusses future avenues of research.

This thesis contains material which is published or in preparation to be published in peer-reviewed journals as first author:

- Pelz, P. M., Qiu, W. X., Bücker, R., Kassier, G. & Miller, R. J. D. *Low-dose cryo electron ptychography via non-convex Bayesian optimization.* Scientific Reports 7, 9883 (2017)
  Material appears in chapters 2 and 4
- Pelz, P. M., Bücker, R., Ramm, G., Kassier, G., Eggert, D., Lu, P. & Miller, R. J. D. *Single-particle electron ptychography.* In preparation
  Material appears in chapters 3 and 4

1 Fundamentals for imaging weakly scattering objects in transmission electron microscopy

This thesis is dedicated to the development of phase contrast techniques in the TEM. For a thorough understanding of the physical effects encountered when working with high-energy electrons, the following chapter provides a mathematical description of the interaction of electrons with matterand propagation of electrons. Furthermore, we give an introduction into the description of general quantum states with different representations of phase space, and show how a full phase space picture can be recovered from multiple measurements.

1.1 Layout of a conventional TEM

The transmission electron microscope is an indispensable tool in todays materials and life sciences. The short wavelength of electrons and the strong interaction with matter are a unique combination that has lead to widespread adoption across the sciences. Historically, the capability of a TEM to analyze the scattered electrons was given by its optical components, and much effort has been invested to improve and perfect them, resulting the development of field emission sources [21, 22], hardware aberration correctors [23, 24], monochromators and energy-filters [25] in the last decades. The optical layout of a state-of-the-art TEM typically involves more then 15 electron optical elements, which must be aligned and tuned according to the planned experiment. Here, we confine us to the description of a conventional TEM with a field emission source similar to the one that is installed at the Max Planck Institute for the Structure and Dynamics of Matter in Hamburg and sketched in Fig. 1.1. After the electrons leave the gun, the gun lenses and deflection coils are adjusted to center the beam in the column and the first condenser lens creates a cross-over, whose vertical position can be adjusted to regulate the current transmitted through the 2nd condenser aperture. This setting is usually called ’spot size’ and a large spot size corresponds to a large beam on the aperture and a resulting small current through the aperture and large coherence length. Below the aperture is a set of beam deflection coils which can shift the beam over the sample. The sample itself sits in between two objective lenses, and in the back focal plane of the second lens its is possible to insert an aperture to block electrons scattered to high angles when the microscope is operated in imaging mode.

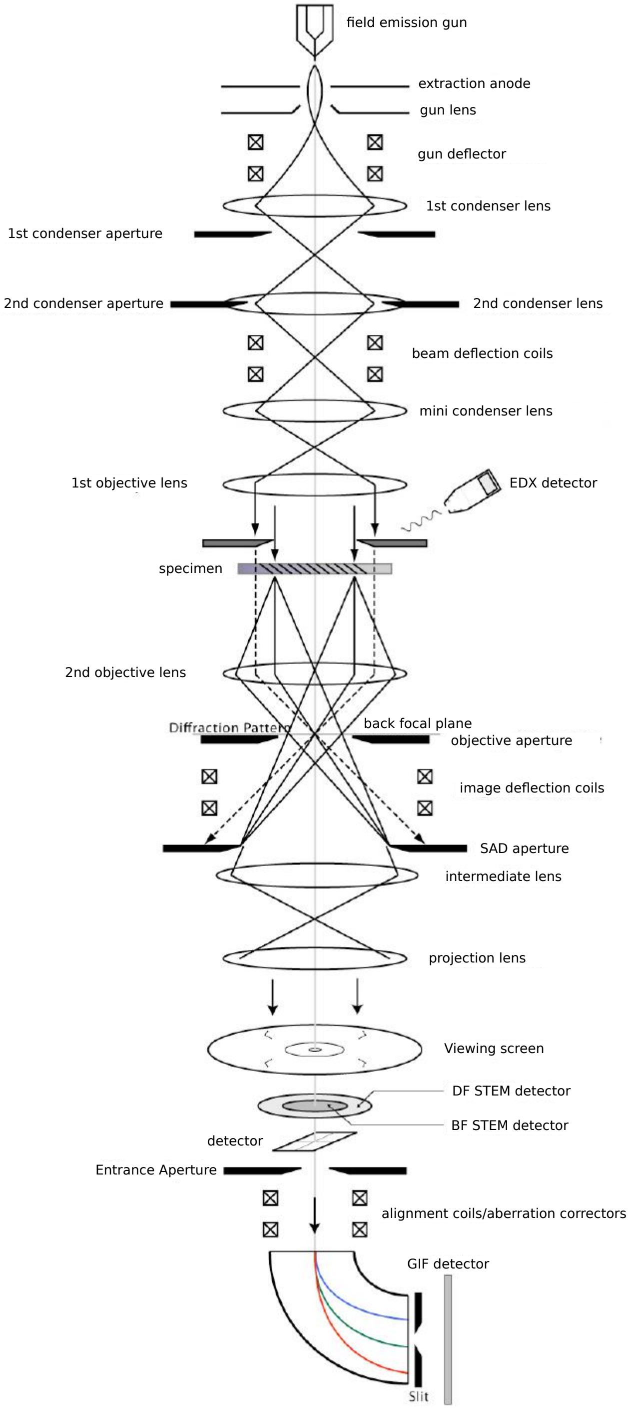

Figure 1.1: Layout and imaging-mode ray paths of a conventional TEM with two condenser lenses, here a FEI Tecnai F20 with an energy filter. Adapted from Bayou [26].

Depending on the imaging mode, a set of intermediate and projection lenses then either magnifies the back focal plane of the objective lens on the detector, creating a diffraction pattern, or it magnifies the image plane, creating a real-space image on the detector. In STEM mode, which is the mode usually used for ptychography, a set of annular detector can also be inserted, which incoherently detect all electrons scattered to high angles. Depending on the range scattering angles they detect, they are either called annular dark field (annular dark field (ADF), 10 mrad to 50 mrad) or high angle annular dark field (HAADF), >50 mrad) detectors. Additionally, it is possible to collect the X-rays generated from inelastic scattering processes with an energy-dispersive X-ray (EDX) detector. The detector usually sits below the HAADF detectors, but it is also possible to install an energy-filter before the detector. This is currently only possible with Gatan cameras with the so-called Gatan Imaging Filter (GIF) or in microscopes of the manufacturer Nion.

1.2 Image formation in the TEM

On the next pages we describe how the intensity is calculated that is recorded on an electron detector, after the electrons have propagated through the sample and the optics of the microscope.

1.2.1 Electron-specimen interactions

Elastic scattering, elastic cross section and scattering factors

The traditional quantum mechanical description of electron scattering starts with a plane wave incident on an atom which, after scattering, gives rise to an outgoing plane wave and an outgoing spherical wave with amplitude $f_e(q)$.

$$\psi(x) = \exp(2\pi i k_z z) + f_e(q)\frac{\exp(2\pi i \mathbf{q}\cdot\mathbf{r})}{r}, \tag{1.1}$$

where $\mathbf{q}$ is the difference between the incident and scattered wave vectors. 2,he complex scattering amplitude $f_e(q)$ can also be referred to as the scattering factor. The simplest method to calculate the scattering factor is the first Born approximation, in which it is the Fourier transform of the atomic potential [27].

$$f_e(\mathbf{q}) = \frac{1}{2\pi e a_0}\int V_a(\mathbf{r})\exp(2\pi i \mathbf{q}\cdot\mathbf{r})d^3r, \tag{1.2}$$

where $V_a(\mathbf{r})$ is the 3D atomic potential of the atom , e is the electron charge, h is Planck's constant and $a_o = 0.5292\,\text{Å}$ is the Bohr radius. The first Born approximation is only valid for a weak phase object, and therefore inadequate for directly calculating electron scattering in an image, but the simple relation between scattering factors and potentials makes it useful for the calculation of specimen potentials from scattering factors obtained with more exact methods. Together with the Fourier projection theorem (Appendix 6.1), the projected potential of a thin slice can easily be calculated by a 2D Fourier transform.

Effective wave vector in material and interaction parameter

The wavelength of a relativistic electron in vacuum is given by

$$\lambda = \frac{hc}{\sqrt{2EE_0 + E^2}}, \tag{1.3}$$

where E_0 is the rest energy of the electron $E_0 = mc^2 = 511\,\text{keV}$. If electrons are subjected to a potential $E_s = eV_s$ inside a material, they gain or lose energy with respect to the vacuum. This effect can be described by defining an effective wave vector k_m inside the material [28]. If E_s is the additional potential energy of the electron while inside the specimen, then the change in wave vector is

$$k_m = \frac{1}{\lambda_m} = \frac{\sqrt{(E+E_s)(2E_0+E+E_s)}}{hc} \simeq k_z + \frac{V_s(E_0+E)}{\lambda V(2E_0+E)}, \tag{1.4}$$

where we Taylor expanded and kept only the lowest order terms in V_s/V. Therefore, the electron wave function passing through the specimen is:

$$\psi(x) = \exp(2\pi i k_m z) \approx \exp(2\pi i k_z z)\exp(2\pi\sigma v_z(x) z), \tag{1.5}$$

where we have introduced the interaction parameter

$$\sigma = \frac{2\pi m e\lambda}{h^2} = \frac{2\pi}{\lambda V}\left(\frac{E_0+E}{2E_0+E}\right), \tag{1.6}$$

with $m = \gamma m_0$ the relativistic mass, and $v_z(x)$ the projected potential. This is subject to the assumption that the potential inside the specimen produces a phase shift $\phi \ll 1$ and the accumulated effect of the specimen can be described by an integral of the scattering potential along z, i.e. if the first Born approximation is fulfilled.

Atomic potential

The atomic potential is usually obtained in a roundabout manner from the Mott-Bethe formula:

$$f_e(q) = \frac{2m_0e^2}{h^2}\left(\frac{Z - f_x(q)}{q^2}\right), \tag{1.7}$$

where $f_x(q)$ is the X-ray scattering factor usually obtained from Hartree-Fock calculations. The Mott-Bethe formula can be derived from Eq. (1.2) by inserting $V_a(\mathbf{r}) = 2\pi/\lambda \int(n-1)dz$ [29] and a Coulomb potential term given by

$$V(r_i) = -\frac{e^2}{4\pi\epsilon_0}\int \frac{\rho(r_j)}{|r_i - r_j|}d^3r_j, \tag{1.8}$$

where $\rho(r_j)$ is the charge distribution in an atom. This means that an error is introduced when the charge distribution is not spherically symmetric. This error may vary between 5 % to 10 % at low scattering angles in aspherical atoms. Bonding in the solid should produce a similar error [28], and if bonding effects are being studied explicitly [30], density functional theory calculations have to be performed to include bonding effects in the potential calculations.
For the investigation of radiation sensitive materials at typical cryo-EM resolutions larger than 2 Å, these effects are negligible and we use here the independent atomic potentials, computed directly from the scattering factor via the inverted Eq. (1.2). To gain an intuition for the range of validity of the weak phase approximation, we show the interaction parameter and the projected atomic potential for a range of elements in Fig. 1.2. The interaction parameter σ for 200 keV electrons is $0.7\,\mathrm{rad(kVÅ)}^{-1}$ and for 300 keV electrons it is $0.65\,\mathrm{rad(kVÅ)}^{-1}$. This means that a carbon atom produces a phase shift of 0.15 rad at 200 keV and 0.17 rad at 300 keV, therefore still constitutes a weak phase object. A gold atom produces a phase shift of 1 rad at 200 keV and 0.94 rad at 300 keV, therefore the first Born approximation breaks down for heavy atoms.

Inelastic scattering

High-energy electrons lose a broad range of energies when scattering inelastically. The following excitations can be distinguished [29]:

1. vibrational excitations in molecules or solids are typically of the order of 20 meV to 1 eV and can only be observed spectroscopically after monochromatization of the electron beam

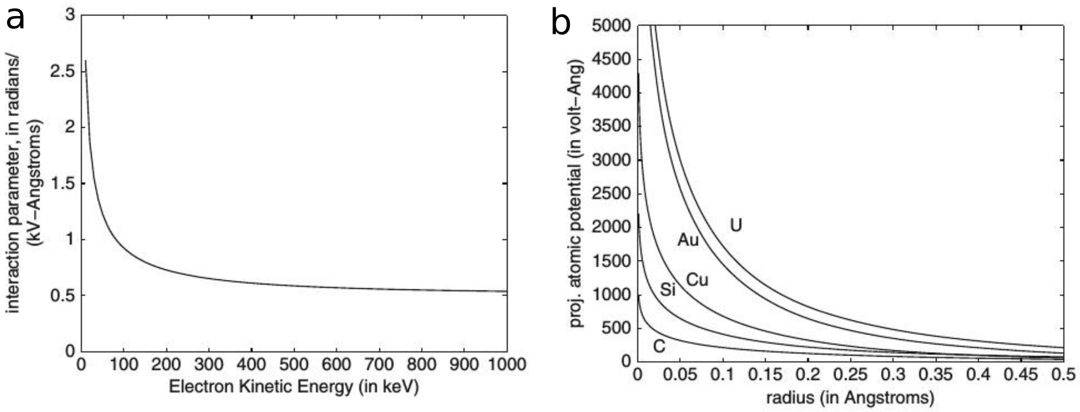

Figure 1.2: a) Plot of the interaction parameter σ vs. electron energy. b) Plot of the projected atomic potential for carbon, silicon, copper, gold, and uranium. Both plots are taken from Kirkland [28].

2. intra- and inter-band excitations of the outer shell atomic electrons and collective excitations (plasmons) of the valence and conduction electrons. The plasmon losses show broad maxima in the energy-loss range of 3 eV to 25 eV. Plasmon losses depend on the concentration of valence and conduction electrons and are influenced by chemical bonds and the band-structure.

3. ionization of core electrons. The energy losses depend on the ionization shell and are typically on the order of several keV

The ratio of elastic to inelastic scattering cross sections can be derived as [29]

$$\nu = \frac{\sigma_{el}}{\sigma_{inel}} = \frac{Z}{4} \ln\left(\frac{h^2}{\pi m_0 J R \lambda} \right)^{-1} \simeq \frac{Z}{26}, \tag{1.9}$$

where Z is the atomic number and J is the mean ionization energy of the atom. Experimentally it was found [31] that

$$\nu \simeq \frac{Z}{20}. \tag{1.10}$$

This means that for elements lighter than calcium, the inelastic scattering cross section is larger than the elastic scattering cross section. For carbon, the factor is roughly 3. Most of the inelastic processes scatter to very low angles smaller than 0.1 mrad [29]. In imaging mode, they hardly mix with the elastic signal in the diffraction plane. It is also important to mention that this ratio is largely independent of energy up to electron energies of 1 MeV, when atomic displacement scattering effects become stronger [32]. Therefore, one is relatively free to choose the electron energy to optimize experimental parameters, without having to worry about a change in the ratio of useful scattering events per unit of radiation damage.

A more intuitive quantity to estimate when inelastic scattering becomes important is the inelastic mean free path Λ_{in}, which can be defined with the help of the total inelastic scattering cross section, the molar mass M_W, the mass density ρ and Avogadro's number N_A:

$$\Lambda_{in} = \frac{M_W}{\rho N_A \sigma_{inel}} = \frac{M_W \beta^2 \cdot 10^{10}}{9.03\, \rho\, Z^{\,0.5}\, \ln\left(\frac{\beta^2 (U_0 - mc^2)}{10}\right)} [\mathrm{nm}]. \tag{1.11}$$

Inserting an average density of protein into Eq. (1.11) yields a mean free path $\Lambda_{in} \sim 190$ nm for 300 keV electrons and $\Lambda_{in} \sim 110$ nm for 100 keV electrons. The mean free path in water or ice can be calculated as $\Lambda_{in} \sim 340$ nm for 300 keV electrons and $\Lambda_{in} \sim 210$ nm for 100 keV electrons [33]. This shows that inelastic scattering plays a minor role for thin samples of water and proteins and can be neglected in image simulations without major effect. [33] estimates that the contribution of inelastic intensity is smaller than 1 % for 100 keV electrons.

Radiation damage processes of organic specimens

Radiation damage in organic materials is caused by all kinds of ionizing irradiation. Most radiation damage in electron microscopy occurs due to electron energy losses between ~5 eV and ~100 eV, which are due to ionization of valence electrons which make up chemical bonds, producing free radicals and causing emission of secondary electrons. The cross-section for ionization of K-shell electrons and knock-on collisions are much lower so that they can be regarded as an irrelevant damage source in biological EM with high-energy electrons.
The damage is quantified by the energy dissipated per unit volume, which is proportional to the number of incident electrons $n = j\tau/e$ per unit area, where τ is the irradiation time in seconds. The incident fluence $q = j\tau = en$ (Cm^{-2}) can therefore be used to quantify irradiation conditions. q is usally called *electron dose* in the TEM community, although, in radiation chemistry, dose is defined as energy dissipated per unit mass, and measured in grays: 1 gray (Gy) $=$ 1j/kg. This misnomer has gained a foothold in the electron microscopy community, and the step of quantifying the radiation damage in units gray in cyo-EM of has until recently usually been skipped, because the achievable resolutions did not

allow conclusions about structural damage. We stick to the term *dose* throughout this thesis to describe the time-integrated electron flux on the sample. Baker & Rubinstein [34] assess comprehensively the radiation damage processes for frozen biological specimens. They tabulate the dose for a given charge density and we give here a few exemplary values: a charge density of $1\,e^-/\mathrm{\AA}^2$ corresponds to a dose of 6.6 MGy for 100 keV electrons and 3.7 MGy for 300 keV electrons. A charge density of $25\,e^-/\mathrm{\AA}^2$ corresponds to a dose of 160 MGy for 100 keV electrons and 92 MGy for 300 keV electrons. Recently, as the resolution is in cryo-EM is getting closer to resolutions achieved in X-ray crystallography, molecule-, residue- and amino-acid specific radiation damage are starting to be studied in cryo-EM. As an example, G. McMullan, Vinothkumar & Henderson show that exposure of $1\,e^-/\mathrm{\AA}^2$ with 300 keV electrons causes water molecules in pure amorphous ice to move by 1 Å [35]. Matthies *et al.* [36] show that negatively charged residues exhibit more pronounced effects of radiation damage in structures solved by cryo-EM.

Tertiary damage to proteins during electron irradiation

Tertiary or global damage as an accumulation of the previously mentioned damage effects leads to bubble formation and distortion due to the production of gas within the sample. Bubbling of samples is due to buildup of hydrogen gas in specimens in aqueous environment. It has been suggested that the free radicals produced by radiolysis of water may recombine to H_2O in bulk water [37], and in our group it has been observed that in the liquid phase some biological function is still retained after high doses of irradiation, but for a detailed evaluation the resolution of liquid-phase microscopy needs to be increased.

The cryo-freezing of the samples mitigates this tertiary radiation damage by mechanically restraining the molecular fragments by the ice matrix, preventing their movement so that imaging can occur for a longer time. A detailed evaluation of the choice of freezing temperature and other experimental parameters can be found in [34].

1.2.2 The paraxial wave equation for high-energy electrons

As mentioned in section 1.2.1, the Born approximation breaks down if the sample becomes too thick or the phase shift due to the atoms in the sample becomes too strong. To properly account for these effects, a more general solution to the Schrödinger equation has to be derived. We start with the Schrödinger equation for free electrons,

$$\left[-\frac{\hbar^2}{2m}\nabla^2 - eV(\mathbf{r})\right]\psi_f(\mathbf{r}) = E\,\psi_f(\mathbf{r}) \tag{1.12}$$

where $\mathrm{m} = \gamma \mathrm{m}_0$ is the relativistic mass of the electron, $e = |e|$ is the magnitude of the charge of the electron, E is the kinetic energy of the electron and $-eV$ is the potential energy of the electron. The energy of the incident high-energy electrons is much greater than the additional energy they gain or lose in the specimen, it is therefore useful to write the wave function of the electrons as a plane wave traveling in z direction and a factor that varies slowly with z:

$$\psi_f(x,y,z) = \psi(x,y,z)\exp(2\pi iz/\lambda), \tag{1.13}$$

where λ is the electron wavelength. For now, we consider only elastic processes, so the total kinetic energy of the electron is:

$$E = \frac{h^2}{2m\lambda^2}, \tag{1.14}$$

Because the electrons travel predominantly in the forward direction, and the wavelength λ is very small, we can assume $\left|\frac{\partial^2\psi}{\partial z^2}\right| << \left|\frac{1}{\lambda}\frac{\partial\psi}{\partial z}\right|$. By putting Eq. (1.13) in Eq. (1.12) and further simplifying with the above approximation, a short calculation [28] yields the paraxial approximation to the Schrödinger equation:

$$\left[\frac{i\lambda}{4\pi i}\nabla^2_{xy} + i\sigma V(x,y,z)\right]\psi(x,y,z) = \frac{\partial\psi(x,y,z)}{\partial z}, \tag{1.15}$$

which ignores backscattered electrons and inelastic processes. Here, σ is the interaction parameter (see Eq. 1.6).

1.2.3 Multislice solution to the wave equation for fast electrons

Eq. (1.15) has a formal operator solution of [28]

$$\psi(x, y, z + \Delta z) = \exp\left(\frac{i\lambda\Delta z}{4\pi}\nabla^2_{xy}\right)T(x, y, z)\psi(x, y, z) + \mathcal{O}\left(\Delta z^2\right), \tag{1.16}$$

where $T(x, y, z)$ is a complex transmission function for the portion of the specimen between z and $z + \Delta z$

$$T(x, y, z) = \exp\left(i\sigma\int_z^{z+\Delta z} V(x, y, z')dz'\right). \tag{1.17}$$

The slice thickness Δz is chosen such that each slice is approximately a weak phase object. The factor $\exp\left(\frac{i\lambda\Delta z}{4\pi}\nabla^2_{xy}\right)$ can be evaluated in Fourier space [28] to yield:

$$\mathcal{F}\left[\psi(x, y, z + \Delta z)\right] = \exp\left(-i\pi\lambda\Delta z(k_x^2 + k_y^2)\right)\mathcal{F}\left[T \cdot \psi\right]. \tag{1.18}$$

This leads to the solution

$$\psi(x, y, z + \Delta z) = p(x, y, \Delta z) \otimes (T(x, y, z)\psi(x, y, z)) + \mathcal{O}\left(\Delta z^2\right), \tag{1.19}$$

with $p(x, y, \Delta z) = \frac{1}{i\lambda\Delta z}\exp\left(\frac{i\pi}{\lambda\Delta z}(x^2 + y^2)\right)$ being the Fresnel propagator, which is the basis of the multi-slice simulations performed in this thesis. The convolution operator $\otimes$ is usually evaluated in Fourier space.

1.2.4 Transmission function from atomic potentials

As discussed in section 1.2.1, the case of purely elastic axial scattering of electrons the complex transmission function mentioned in Eq. (1.16) can be described as:

$$T(x, y) = \exp(i\sigma v_z(x, y)), \tag{1.20}$$

where σ is the interaction constant and $v_z(x, y)$ is the total projected atomic potential of the specimen. We discussed in 1.2.1 that the isolated atom superposition approximation (IASA) is a reasonably good approximation to compute the atomic potential of proteins for high energy electrons. This means that the main contribution to the potential comes from the electrostatic potential of the isolated atoms.

$$v(x,y) = \sum_{j=1}^{N} v_{Z_j}(\mathbf{r} - \mathbf{R}_j), \tag{1.21}$$

where $v_{z_j}(\mathbf{r} - \mathbf{R}_j)$ is the electrostatic potential of an isolated neutral atom with atomic number Z_j centered at $\mathbf{R}_j$, as calculated in section 1.2.1. The IASA ignores the potential due to charge redistributions, which accounts for the interaction with neighboring atoms, solvent and ions. Biological specimens are embedded in an amorphous solvent and the potential distribution depends on the dielectric and ionic properties of the solvent. This potential change can be accounted for via a continuum electrostatics approach as done in [33]. Inelastic scattering is usually modeled as the imaginary part of the interaction potential.

$$v_{tot} = v_{ph} + i v_{ab}, \tag{1.22}$$

where v_{ph} is the interaction potential as described before. v_{ab} contributes the amplitude contrast as it would appear in a zero-loss filtered image. For an amorphous solvent and a certain incident electron energy, the inelastic contributions can be described via the inelastic mean free path Λ_{in} (1.11).

$$v_{ab}(x,y,z) = \frac{1}{2\sigma\Lambda_{in}}, \tag{1.23}$$

where σ is the interaction constant defined above.

1.2.5 Optical transfer function of electron lenses

Aberrations are inherent to round lenses, and the electron wave function exiting the specimen is therefore subject to a frequency dependent phase shift introduced by the defocus δf and the aberrations such as spherical aberration C_s and 2-fold astigmatism (A_1, α_1) of the objective lens. The contrast transfer function (CTF) of the lens system in polar spatial frequency coordinates is [29]:

$$\begin{aligned} B &= (\Delta z - A_1 \cos(2(\alpha - \alpha_1))) \\ CTF(q,\alpha) &= K A_p \exp\left(-2\pi i k \left(0.25 C_s q^4 \lambda^4 + 0.5 q^2 \lambda^2 B\right)\right), \end{aligned} \tag{1.24}$$

with $k = 2\pi/\lambda$ the reciprocal wavelength, $\mathrm{C_s}$ the coefficient of spherical aberration of the objective lens, z the defocus of the objective lens, A_p the objective aperture function. The prefactor K decribes spatial and chromatic envelopes

[33]. The transmission through the optical system to the detector can then be described by a transmission through the in the back focal plane of the sample:

$$I_0(\mathbf{r}) = \left|\mathcal{F}^\dagger\left[\mathcal{F}\left[\psi_{exit}(\mathbf{r})\right] CTF(q,\alpha)\right]\right|^2. \tag{1.25}$$

If the microscope is run in diffraction or STEM mode, the influence of the objective lens is negligible, because the beam in the back focal plane is very small and is influenced very little by the phase shift. Therefore the diffraction pattern intensity is just the Fourier transform of the exit wave

$$I_0(\mathbf{q}) = \left|\mathcal{F}\left[\psi_{exit}(\mathbf{r})\right]\right|^2. \tag{1.26}$$

.

1.2.6 Detector response

Capturing the final image involves conversion of the intensity distribution into a digital signal via an electron detector. Electron detectors are characterized by parameters such as conversion factor CF in $[ADU/e^-]$, modulation transfer function (MTF), and detective quantum efficiency (DQE). The measurement process obeys Poisson statistics, unless complicated entanglement schemes are implemented to reach Heisenberg statistics [38–41], none of which has been demonstrated yet and all of which involve significant advances in current microscope hardware. The detector adds readout noise I_m and dark current I_{dc} to the final image, and blurs the image with a detector point spread function, whose Fourier transform is the MTF.

The MTF describes the signal amplitude for different spatial frequencies. However, the signal and the noise in an electron detector are not tranferred in the same way. Therefore, one defines noise transfer function (NTF)

$$NTF^2(q) = \frac{NPS_{out}}{CF^2\Phi_e}, \tag{1.27}$$

where NPS is the noise power spectrum and Φ_e the incident electron flux in e^-/area. The intensity after detection is modeled as [33]:

$$I(\mathbf{q}) = \mathcal{F}^\dagger\left[\mathcal{F}\left[\text{Poisson}\left(\mathcal{F}^\dagger\left[\mathcal{F}\left[I_0(\mathbf{q})\right]\cdot\sqrt{\text{DQE}(\mathbf{q})}\right]\right)\right]\cdot\text{NTF}(\mathbf{q})\right], \tag{1.28}$$

where NTF and DQE are properties of the detector [42, 43] and Poisson(x) samples from a Poisson distribution with mean x.

1.2.7 *slice++* - an open-source GPU-accelerated implementation of the multislice algorithm

At the beginning of the work for this thesis, all available open-source multi-slice implementations were CPU-based, and the necessity to be able to simulate an electron ptychography experiment quickly became clear. Therefore, some effort in creating a fast, GPU-accelerated version of the multi-slice algorithm was invested.

The development was based on the stable and accurate open-source package QSTEM [44], written in C++. The code was first modularized into classes, and then all array computations were replaced with GPU operations based on the open-source GPU acceleration library ArrayFire [45]. The summer student Wen Qiu helped with the refactoring of the code to transition from CPU to GPU arrays. We describe shortly the code structure of *slice++*. Fig. 1.3 shows a simplified class diagram of the main classes in *slice++*.

The code is structured into class hierarchies, which implement several functionalities needed for the simulation. First, a `json` configuration file is read which contains all the simulation parameters. Based on the configuration, an incoming wave class inherited from `CBaseWave` is created. Depending on the file ending of the structure file, a file reader inherited from `IStructureReader` is created, which then reads the structure input file with atomic coordinates. The structure file reader is based on the open-source package OpenBabel [46], which supports all major structure file formats, including cif and pdb formats. Then, a class inherited from `IStructureBuilder` is created which builds the atomic structure from the structure file. This can either be a crystal (`CrystalBuilder`), or a larger superstructure (`SuperStructureBuilder`), defined from multiple structure files. After this, a class inherited from `CPotential` is created, which creates the potential slices from the atomic coordinates and the scattering factors, and converts them into phase gratings.

In a last step, a class inherited from `BaseExperiment` is created, which contains a wave function, the created potential, a `PersistenceManager` class which can save the computed images to disk, and a class inherited from `IDetector`, which computes the noise effects after the exit wave is propagated to the detector plane. When the `Run()` method of the experiment is called, the wave function is propagated through the the sample slices given by the `CPotential` class, through the optical system after the sample, and then `IDetector::RecordImage(wave)` is called on the resulting wave function at the detector. This structures enables an easy implementation of new experimental schemes or detector configurations, since the propagation, structure building, and detection are decoupled into dif-

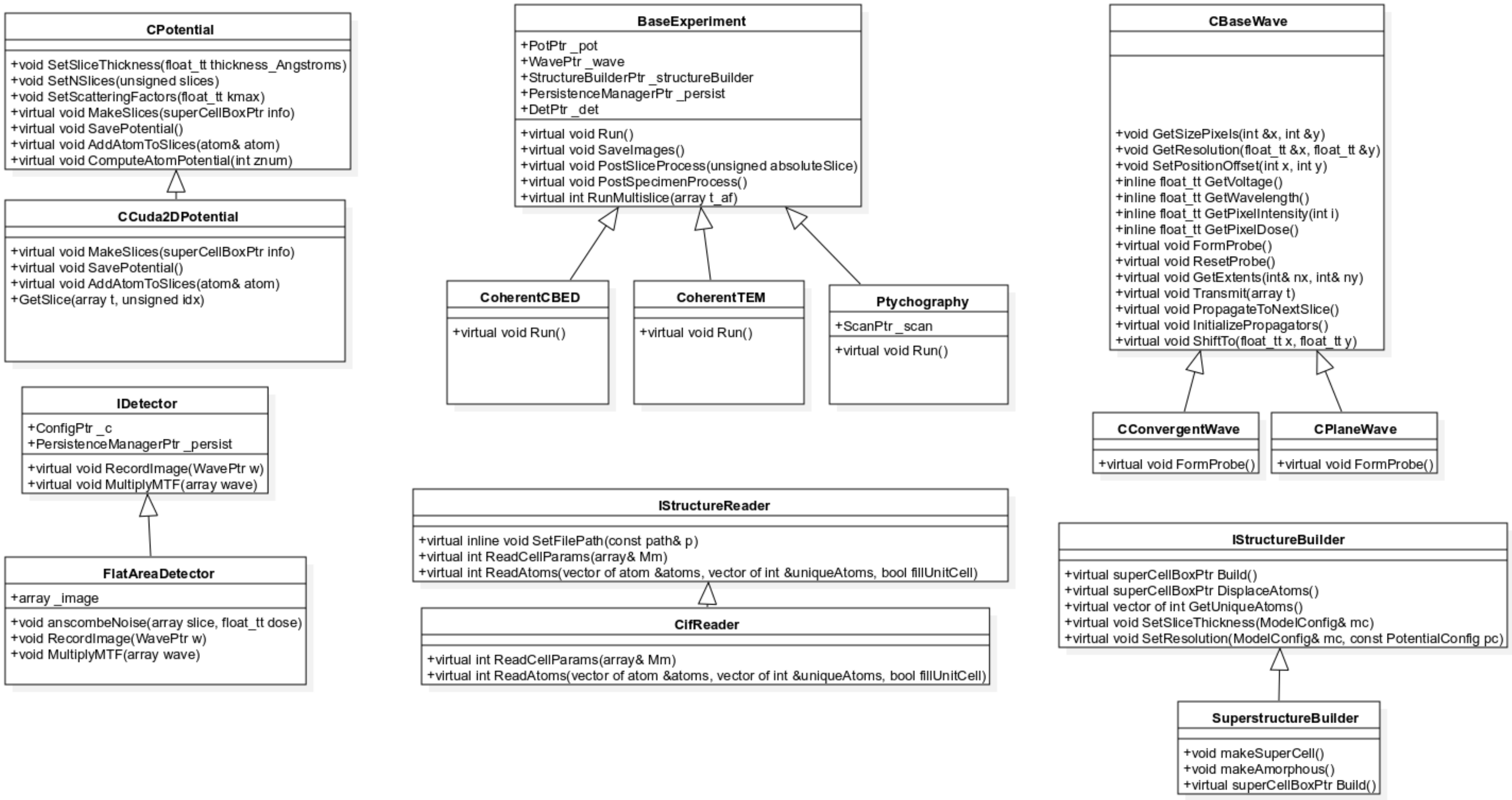

Figure 1.3: Simplified class diagram of *slice++*

ferent classes, and only the interface of the respective base class needs to be implemented.
slice++ is available as open source under `https://github.com/PhilippPelz/slicepp` under a GPLv2 license.

1.2.8 Density operator

Above, we ignored the fact that the electrons produced by realistic electron sources are generally not fully coherent, i.e. cannot be described by a single wave function. Also if inelastic processes are studied, the wave function formalism is not expressive enough and must be extended, because the beam electrons become entangled with a multitude of object states due to the inelastic interaction, leading to decoherence of its single-particle state.
One can model such systems with the help of the hermitian, positive semidefinite density operator $\hat{\rho}$. The aforementioned properties mean that $\hat{\rho}$ may be diagonalized in some basis

$$\hat{\rho} = \sum_{\mathsf{m}} |c_{\mathsf{m}}|^2 \, |\psi_{\mathsf{m}}\rangle \, \langle\psi_{\mathsf{m}}| \,. \tag{1.29}$$

We define the purity of a quantum state as

$$\zeta = \mathrm{tr}\big(\hat{\rho}^2\big) \leq 1. \tag{1.30}$$

A pure quantum state obeys $\zeta = 1$. The most important basis representation for the density operator in the context of this work are be the spatial

$$\hat{\rho} = \iint_{-\infty}^{\infty} \mathrm{d}x \, \mathrm{d}x' \, |x\rangle \; \langle x|\hat{\rho}|x'\rangle \tag{1.31}$$

$$= \iint_{-\infty}^{\infty} \mathrm{d}x \, \mathrm{d}x' \, |x\rangle \, \rho(x, x') \, \langle x'| \tag{1.32}$$

and momentum

$$\hat{\rho} = \iint_{-\infty}^{\infty} \mathrm{d}q \, \mathrm{d}q' \, |q\rangle \; \langle q|\hat{\rho}|q'\rangle \tag{1.33}$$

$$= \iint_{-\infty}^{\infty} \mathrm{d}q \, \mathrm{d}q' \, |x\rangle \, \rho(q, q') \, \langle q'| \tag{1.34}$$

representations. The matrix elements in position $\rho(x, x')$ and momentum $\rho(q, q')$ representation are usually referred to as *density matrix*. As a consequence of the definition of the density operator, they are symmetric in their arguments, e.g.

$$\begin{aligned} \rho(x, x') &= \langle x|\hat{\rho}|x'\rangle \\ &= \sum_m |c_m|^2 \langle x|\psi_m\rangle \langle\psi_m|x'\rangle \\ &= \sum_m |c_m|^2 \langle x'|\psi_m\rangle^* \langle\psi_m|x'\rangle^* \\ &= \rho^*(x', x) \end{aligned} \tag{1.35}$$

The computation of the outcome of a measurement with an observable $\hat{\mathrm{A}}$ in a partially coherent system can then be performed by taking the following trace:

$$\langle A\rangle_{\hat{\rho}} = \mathrm{tr}\left(\hat{\rho}\hat{A}\right). \tag{1.36}$$

In particular, in the spatial representation of the density matrix, the detected intensity in the image plane lies on the diagonal

$$I(r) = \rho(x = r, x' = r). \tag{1.37}$$

The paraxial dynamics of the density operator are governed by the paraxial von Neumann equation in the Heisenberg picture [47]:

$$\begin{aligned} \frac{\partial\hat{\rho}}{\partial z} &= \sum_m \quad |c_m|^2 \left(\frac{\partial\,|\psi_m\rangle}{\partial z}\langle\psi_m| + |\psi_m\rangle\frac{\partial\,\langle\psi_m|}{\partial z}\right) \\ &= \sum_m \quad |c_m|^2 \left(-i\hat{H}\,|\psi_m\rangle\langle\psi_m| + i\,|\psi_m\rangle\langle\psi_m|\,\hat{H}\right) \\ &= -i\left[\hat{H}, \hat{\rho}\right], \end{aligned} \tag{1.38}$$

where $[\bullet, \bullet]$ is the quantum mechanical commutator. To solve the complete dynamical scattering problem of a mixed quantum state, including inelastic scattering, one typically resorts to perturbation schemes facilitating approximate solutions [48–50]. The topics discussed in this thesis can be approximately treated by single elastic axial scattering of a nearly pure, or low-rank state of free electrons, and as discussed in section 1.2.1, also the inelastic contributions in the sample are negligible. In this case, the Hamiltonian does not depend on m and we can write

$$\frac{\partial\rho(\mathbf{r}, \mathbf{r}', z)}{\partial z} = -i(H_{ax}(\mathbf{r}, z) - H_{ax}(\mathbf{r}', z))\rho(\mathbf{r}, \mathbf{r}', z), \tag{1.39}$$

which has the solution

$$\frac{\partial\rho(\mathbf{r},\mathbf{r}',z)}{\partial z} = T_{el}(\mathbf{r},\mathbf{r}',z)\rho(\mathbf{r},\mathbf{r}',z). \tag{1.40}$$

The function T_{el}, depending on two spatial coordinates, is called mutual object transparency [51]. In the case of purely elastic axial scattering, the transparency

$$\begin{aligned} T_{el}(\mathbf{r},\mathbf{r}') = &\exp\left(\frac{ie}{v}\int_{-\infty}^{z} \mathrm{d}z\,(\Phi(\mathbf{r},z') - \Phi(\mathbf{r}',z'))\right) \\ &\times \exp\left(-i\int_{-\infty}^{z} \mathrm{d}z\,(A_z(\mathbf{r},z') - A_z(\mathbf{r}',z'))\right) \\ &\times \exp\left(-\frac{1}{2}\int_{-\infty}^{z} \mathrm{d}z\,(\mu_{el}(\mathbf{r},z') + \mu_{el}(\mathbf{r}',z'))\right) \end{aligned} \tag{1.41}$$

contains the projected electrostatic (first term) and magnetostatic (second term) potentials as phase and the projected elastic damping coefficient as amplitude argument.

1.2.9 Wigner Function

We now introduce another, equally powerful representation of a quantum state - the *Wigner function* representation of quantum mechanical phase space. The Wigner function of a one-dimensional electron wave function, i.e. a pure quantum state, is defined as

$$W_\psi(r,k) := \frac{1}{2\pi}\int_{-\infty}^{\infty} \mathrm{d}r\,\psi^*\left(r - \frac{1}{2}r'\right)\psi\left(r + \frac{1}{2}r'\right)\exp(-ikr'), \tag{1.42}$$

where the normalization guarantees

$$\iint_{-\infty}^{\infty} \mathrm{d}r\,\mathrm{d}q\,W_\psi(r,k) = 1 \tag{1.43}$$

for normalized wave vectors ψ.

The Wigner function has the following properties: Because it is the Fourier transform of the hermitian function $\psi^*\left(r - \frac{1}{2}r'\right)\psi\left(r + \frac{1}{2}r'\right)$, it is always real.

It is not necessarily non-negative, and the existence of negative values is the result of coherent effects.

The integral over one set of variables gives the square modulus of the function in the representation of the remaining variable

$$\int W_{\psi}(r,k)dr = |\psi(k)|^2 \tag{1.44}$$

$$\int W_{\psi}(r,k)dq = |\psi(r)|^2, \tag{1.45}$$

i.e. the marginal of the Wigner function along r yields the far-field intensity, while the marginal along q yields the real-space image. This makes it especially useful for discussing the optical transfer in the TEM.
The purity of a quantum state, already defined in Eq. (1.30) for the density matrix, is the integral over the squared Wigner function:

$$\zeta = 2\pi \iint dr\, dk W_{\psi}^2(r,k) \leq 1 \tag{1.46}$$

1.2.9.1 Linear mappings of the Wigner function

The Wigner function has the convenient property that the effects of propagation through free space and through optical systems can be expressed as linear transformations in phase space.

Fractional Fourier transform

The fractional Fourier transform can be associated with a clockwise rotation of phase space [52]

$$W_{\mathcal{F}_{\theta}[\psi]}(r,k) = W_{\psi}(r\cos(\theta) - k\sin(\theta), k\cos(\theta) + r\sin(\theta)). \tag{1.47}$$

Free-space propagation and defocus

The free-space dynamics of of the Wigner function in the paraxial regime are governed by the free-space Liouville-equation [53]

$$\left(\frac{\partial}{\partial z} + \frac{1}{k_0}\mathbf{k}\cdot\nabla\right) W_{\psi}(\mathbf{r},\mathbf{k},z) = 0. \tag{1.48}$$

Accordingly, the Wigner function of a propagated quantum state reads

$$W_{\psi}(\mathbf{r},\mathbf{k},z) = W_{\psi}(\mathbf{r} - \frac{z}{q_0}\mathbf{k},\mathbf{k},0). \tag{1.49}$$

This means, free-space propagation corresponds to a shear in phase space. Because the free-space Fresnel propagator, as well as the action of a defocusing lens, modulate the wave function in Fourier space with a phase profile $\propto k^2$, also the action of a defocus can be described by a shear in phase space.

Wigner function of mixed states

For mixed states, the Wigner function can be computed from the density matrix

$$\begin{aligned} W_\rho(r,k) &= \frac{1}{2\pi}\int_{-\infty}^{\infty} \mathrm{d}r' \sum_m |c_m|^2 \psi_m^* \left(r - \frac{1}{2}r'\right) \psi_m^* \left(r + \frac{1}{2}r'\right) \exp(-ikr') \\ &= \frac{1}{2\pi}\int_{-\infty}^{\infty} \mathrm{d}r'\, \rho \left(r + \frac{1}{2}r', r - \frac{1}{2}r'\right) \exp(-ikr'), \end{aligned} \tag{1.50}$$

i.e. it can be synthesized from a set of pure-state Wigner functions of the coherent modes of a quantum state.

1.2.10 Ambiguity function

The Fourier transform of the Wigner function along both phase space coordinates

$$\mathcal{F}_{(r,k),(q,p)}\left[W\right](q,p) = \iint_{-\infty}^{\infty} \mathrm{d}k\, \mathrm{d}r\, W(r,k)\exp(-2\pi iqr)\exp(-2\pi ikp) \tag{1.51}$$

is referred to as *ambiguity function*. It is defined as

$$\chi_\psi(q,p) \equiv \int \psi^*(q' - \frac{q}{2})\psi(q' + \frac{q}{2})e^{-2\pi iq'\cdot p}\,\mathrm{d}q' \tag{1.52}$$

and can also be obtained by a Fourier transform of the density matrix along the main diagonal

$$\chi_\psi(q,p) = \frac{1}{2\pi}\int \rho(r - \frac{1}{2}p, r + \frac{1}{2}p)e^{-2\pi iqr}\,\mathrm{d}r\,. \tag{1.53}$$

Instead of the marginal property, the ambiguity function of a pure state satisfies cross-section relations

$$\mathcal{F}\left[|\psi(q)|^2\right] = \chi_\psi(q, p = 0) \qquad \text{and} \tag{1.54}$$

$$\mathcal{F}^\dagger\left[|\tilde{\psi}(p)|^2\right] = \chi_\psi(q = 0, p). \tag{1.55}$$

This means, that the Fourier transform of the real-space intensity is a cross section of the ambiguity function. Note that, unless the Wigner function is symmetric around two axes, the ambiguity function is complex. Ambiguity function, Wigner function, and density matrix represent three equivalent representations of a quantum state and may therefore be used interchangeably.

1.2.11 Quantum state reconstruction in the TEM - algorithmic methods for phase contrast

We have discussed in the last sections that the measurement of an observable always involves a reduction in dimensionality, either by a projection along an axis, a trace or a cross section. The field of *quantum state reconstruction* or *quantum state tomography* deals with the recovery of the quantum state from a series of measurements that completely describe the quantum state. The term tomography can be visualized best with the Wigner representation of a quantum state.

If a quantum state is propagated in free-space from the near field to the far field and measurements at different propagation distances are taken, a shear-series of the Wigner function is collected as depicted in Fig. 1.4. It can be shown that this shear series corresponds to a tilt-series of phase space, where each shear can be described by a tilt by an angle α and an additional scaling of he coordinate system [53]. The angle $\alpha = \arctan(1/F)$ is equal to the arctan of the inverse Fresnel number. The Fresnel number $F = \frac{a^2}{z\lambda}$, with a the real-space extension of

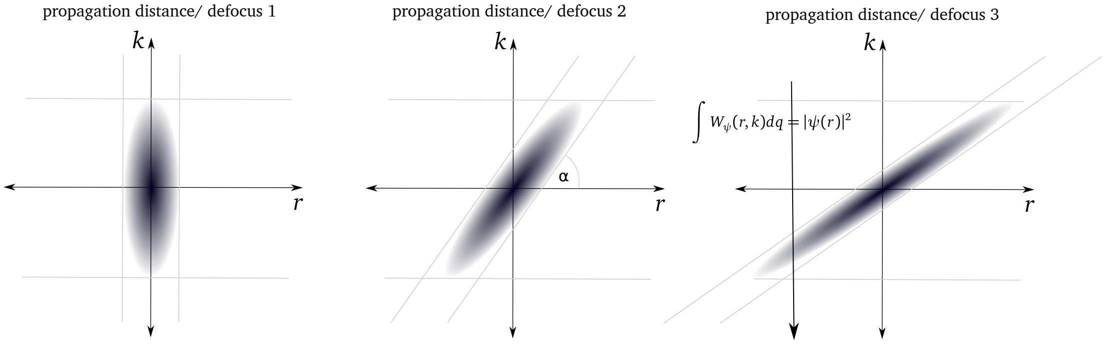

Figure 1.4: Quantum tomography explained with the example of free-space propagation and measurement at different propagation distances. As a quantum state propagates, its phase space distribution is sheared along the horizontal axis. A measurement corresponds to projection along the vertical/momentum axis. A shear can be equivalently described by a rotation by an angle α, and subsequent scaling. Tomography the involves measurements at rotation angles $] - \pi/2, \pi/2]$, i.e. from the far-field to the real space to the far field again.

the state, serves to distinguish near-field ($F \gg 1$) and far-field ($F \ll 1$) propagation, and therefore gives an intuitive explanation of the phase space picture of propagation.

Therefore one way to synthesize the phase space from its projections is by propagating or defocusing a quantum state from its current z position to the far field in both directions. Then, traditional methods of tomography can be used to recover the state. This principle to recover quantum states from projections of their phase space was pioneered in quantum optics [54, 55], and has since been applied and generalized to many other areas of physics.

1.2.12 The phase retrieval problem: a special case of quantum state reconstruction

The *phase retrieval problem* for wave functions mentioned in the introduction can be shown to be a special case of the more general quantum state reconstruction problem. Describing a quantum state with a wave function implies a pure quantum state, i.e. $\hat{\rho} = |\psi\rangle\langle\psi|$. In the case of single elastic scattering, the transmission through the sample can be described as a simple multiplication, and can therefore be expressed by a rank 1 measurement operator $\mathcal{I}_\mathsf{k} = |\mathbf{i}_\mathsf{k}\rangle\langle\mathbf{i}_\mathsf{k}|$. The measurement process can then be written as

$$I_\mathsf{k} = \mathsf{tr}(|\psi\rangle\langle\psi|\,|\mathbf{i}_\mathsf{k}\rangle\langle\mathbf{i}_\mathsf{k}|), \quad \mathsf{k} = 1, ..., \mathsf{m}. \tag{1.56}$$

This is equivalent to writing

$$I_\mathsf{k} = |\langle\mathbf{i}_\mathsf{k}|\psi\rangle|^2, \quad \mathsf{k} = 1, ..., \mathsf{m}. \tag{1.57}$$

Due to the nature of the measurement process, the wave function or quantum state is usually reconstructed in a discrete Hilbert space. Then, the above equation can be conveniently written in matrix form.

We define the discretely sampled wave function $\psi^\vee \in \mathbb{C}^\mathsf{n}$ and the discretely sampled measurement vectors $\mathbf{i}_\mathsf{k} \in \mathbb{C}^\mathsf{m}$. Then Eq. (1.57) can be rewritten as

$$\mathbf{I} = |\mathcal{A}\psi^\vee|^2, \tag{1.58}$$

where $\mathcal{A} : \mathbb{C}^\mathsf{n} \to \mathbb{C}^{\mathsf{km}}$ is a linear operator and the vectors $\mathbf{i}_\mathsf{k}$ are the row vectors of $\mathcal{A}$. We call the problem of finding the phases of $\psi^\vee$ the *generalized phase retrieval problem*. We note that the multiplicative nature of the model allows to swap $\psi^\vee$ and $\mathbf{i}_\mathsf{k}$, which means that the measurement vectors can also be the quantity that

is reconstructed, instead of the wave function.
This means that, if the measurement vectors $\mathbf{a}_k$ represent a quorum [56, 57], Eq. (1.58) is formally equivalent to Eq. (1.36), which means that the generalized phase retrieval problem is equivalent to quantum state tomography with a rank 1 density matrix and rank 1 measurements, i.e. applies only to the reconstruction of pure states. Due to the experimental limitations in the electron microscope, the choice of the measurement vectors $\mathbf{a}_k$ is quite limited and we discuss possible experimental realizations in the following sections.

1.3 Phase-contrast methods in transmission electron microscopy

This chapter treats most of the main phase contrast methods used in electron microscopy today, namely phase contrast from coherent aberrations, Zernike phase contrast, and several methods for computational recovery of phase contrast. We discuss focal series inline-holography, off-axis holography, STEM ptychography and Fourier ptychography. We do not discuss differential phase contrast and the various solutions of the transport-of-intensity equation (TIE), as they do not allow to recover the full quantum state. A discussion of these techniques can be found in Lubk [10]. In the last section we consider several possible experimental implementations for single-shot phase-retrieval with electrons.

1.3.1 Phase contrast transfer in conventional transmission electron microscopy

The phases in the object transfer like the imaginary part of the [29], and therefore undergo a sinusoidal modulation in Fourier space, which define the CTF

$$\begin{aligned} B &= (\Delta z - A_1 \cos(2(\alpha - \alpha_1))) \\ PCTF_{zernike}(q,\alpha) &= KA_p \sin\big(-2\pi i k \left(0.25 C_s q^4 \lambda^4 + 0.5 q^2 \lambda^2 B\right)\big). \end{aligned} \tag{1.59}$$

The sinusoidal form of the phase contrast transfer function means that low spatial frequencies are transmitted poorly by the lenses in the electron microscope. Because the low spatial frequencies are important to identify single particles in the first place, this effect must be counteracted by applying a large amount of defocus. Two exemplary phase contrast transfer function (PCTF) functions with

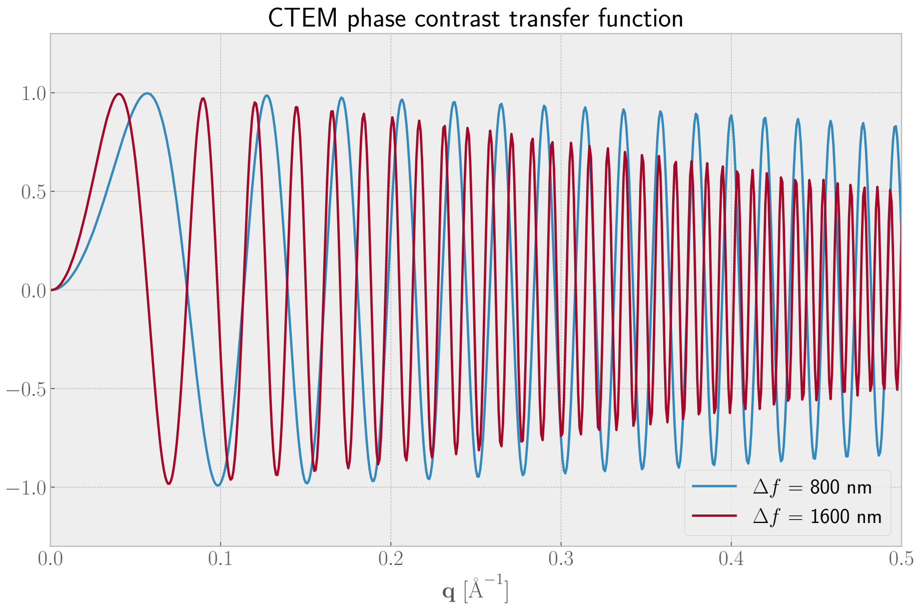

Figure 1.5: Phase contrast transfer function for two different defocus values. By using a range of defoci for data collection, all spatial frequencies are represented in a large data set.

typical defocus values used in cryo-EM are plotted in Fig. 1.5. The large defocus introduces contrast reversals already at low spatial frequencies, and therefore a large data set with a range of defoci needs to be collected to cover the whole Fourier space with information.

1.3.2 Zernike-type phase contrast

Zernike discovered in 1942 [2, 3] that by applying a 90° phase shift to the unscattered beam in the back focal plane of the objective aperture, it is possible to achieve linear phase contrast in the image for low spatial frequencies. This can be easily seen by multiplying Eq. (1.24) by $e^{i\pi/2}$: the phase contrast transfer now has a cosinusoidal form:

$$\begin{aligned} B &= (\Delta z - A_1 \cos(2(\alpha - \alpha_1))) \\ PCTF_{zernike}(q, \alpha) &= KA_p \cos\left(-2\pi ik\left(0.25C_s q^4 \lambda^4 + 0.5q^2\lambda^2 B\right)\right). \end{aligned} \tag{1.60}$$

The PCTF for bright-field TEM with a Zernike phase plate is shown for two examples in Fig. 1.6. Judging from the PCTF plot it is clear that the optimum contrast

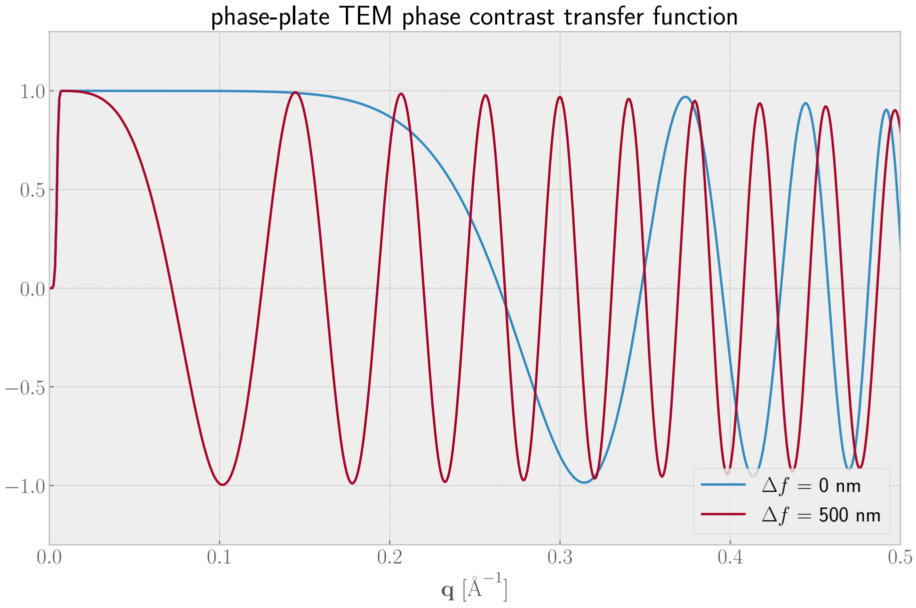

Figure 1.6: Phase contrast transfer function with Zernike phase plate for two different defocus values.

transfer happens at zero defocus. Practically, however, it is very hard to exactly determine the zero defocus position at low electron doses, because usually the radial intensity modulation in the Fourier transform of the image (Thon rings) is used to fit the defocus value. At very low defocus, defocus determination with this method becomes very imprecise, and therefore the Volta phase plate is always used at a few 100 nm defocus [20]. In the following sections, we discuss the possibilities and attempts to realize a Zernike phase plate for electrons.

Thin-film quarter-wave phase plates

Soon after Zernike's idea, in 1947 Boersch proposed to use a thin carbon film as a Zernike phase plate in an electron microscope [19]. In the following decades, a number of unsuccessful attempts at creating such a thin-film phase plate were made. Since most of the results were unsatisfactory, only few papers were published about it [58, 59]. Only recently, Danev *et al.* have succeeded in creating a practical and simple design [4], which is now used by the majority of the cryo-EM community. It is based on a surface chemical effect which creates a phase advance of the central beam relative to the scattered beam in the presence of strong irradiation of an amorphous carbon film in the central diffraction spot in the back focal plane. The effect is dependent on the total dose and on residual gases in the vacuum, but the exact physics and chemistry leading to the effect are unclear. Consequently, an optimal phase shift of 90° can not be guaranteed.

In addition to the not precisely controllable phase shift, the insertion of material in the path of the electrons behind the sample causes additional elastic and inelastic scattering, which reduces the contrast slightly. Danev *et al.* report a 18 % signal reduction compared to imaging without the Volta phase-plate at 200 keV.

While these inefficiencies point at areas where improvement is possible, the cryo-EM community has adopted this device broadly for the lack of a better alternative.
A series of other phase plate design have been proposed in the past with limited success. We only mention them briefly here and point the interested reader to the excellent review article [60].

Phase plates based on the electrostatic effect

An electrostatic field causes a phase shift to a passing free electron. Another option is therefore to create a local electric field in the center of the back-focal plane of the objective lens that corresponds to a phase shift of $\pi/2$. A few promising designs fabricate a miniaturized electrostatic einzel lens via focused ion beam (FIB) milling [61] or by lithographic means [62, 63], to allow mass production and reproducibility. The gained flexibility of tunable phase comes at the cost of blocking parts of the beam completely, therefore resulting in loss of information at low spatial frequencies, decoherence, inelastic losses and charging issues.

Phase plates based on magnetic fields

A magnetic vector potential A_z in the path of a free electron exhibits a phase shift of

$$\phi(x,y) = \frac{e}{\hbar}\int_{-\infty}^{+\infty} A_z(x,y,z)dz, \tag{1.61}$$

where e and $\hbar$ are the absolute values of the electron charge and the reduced Planck constant, respectively. Two designs were proposed to achieve an appropriate configuration of the magnetic vector field: The first[64] proposes the use of ferromagnetic rings of a radial thickness of 30 nm in the back focal plane of the objective lens. If the magnetic fluence in such a ring forms a continuous loop, the magnetic vector potential inside and outside the loop points in opposite directions. In this way, an arbitrary phase shift is realizable which is independent of the electron energy. The disadvantage of this design again is the obstruction of parts of the beam by the ring holder and the ring itself.

The second design was proposed recently and makes use of Ampere's law to create the magnetic vector potential [65]. It creates a magnetic field circulating around a vertical segment of a current-carrying wire, which adds a position-dependent phase shift to the electron wave. When placed in the back-focal plane of the objective aperture, it provides a phase shift of

$$\phi(q) = \frac{e}{\hbar}\frac{\mu_0}{4\pi}\log\left(\frac{(q_x - q_c)^2 + q_y^2}{q_c^2}\right). \tag{1.62}$$

This comes very close to the ideal step-function phase shift of a Zernike phase plate, while only obstructing a very thin section which holds the current-carrying wire. Due to the tuneability of the phase shift via the current flowing through the wire, this design has a clear advantage over the Volta phase plate and might also be easier to handle.

1.3.3 Experimental implementations for quantum state reconstruction in the TEM

In the language of quantum mechanics and phase space introduced in sections 1.2.8 and 1.2.9 it is immediately clear that the methods described above are far from optimal to recover phase. We have discussed that measurement always implies taking a trace, cross-section or projection, depending on the state representation, such that the optical transfer through the microscope cannot be disentangled from a single measurement. This manifests itself in the contrast transfer functions discussed above. Even worse, any use of material behind the sample involves another scattering process, which means information loss into inelastic channels.

The remedy for this problem is to collect a number of measurements with identical incoming quantum states and no obstruction to the beam behind the sample, to then synthesize the quantum state from this set of measurements. This is the quantum state reconstruction procedure described in section 1.2.11. We now describe four possible and popular experimental implementations of quantum state reconstruction in the TEM, and describe the history of application and their suitability for low-dose imaging of biological samples.

1.3.3.1 Focal series inline holography

Focal series inline holography intends to recover the quantum state from a set of defocused images taken over a large focal range. In a TEM, typically the object plane and the image plane remains fixed. Thus, focal series are usually acquired by varying the lens excitation of a single lens above the sample. A sketch of the experimental setup is show in Fig. 1.7. In its phase space formulation [53], as it was described in section 1.2.11 it becomes evident that, if the focal series reaches from the far-field to the near field to the far field, the full dataset represents a tomography of the corresponding Wigner function of the free electrons in phase space. It is however far from trivial to acquire a large range focal series in a TEM that is free from variations other than defocus. Changing the electron optical system induces additional image rotations, distortions, shifts and at high resolution parasitic aberrations. Disentangling all these effects has thus far proved too large of a hurdle for a full phase space tomography in the TEM. It has nevertheless been successfully employed for visible light [55] and X-rays [66]. Focal series reconstructions of pure states are, however, widely-used to reconstruct wave functions with atomic resolution [67–72] and at medium resolution [73]. In these experiments, the focus is typically varied only in the near field, such that quantification is relatively straightforward. The reconstruction of a unique wave function from such a set of images remains somewhat elusive. Questions regarding the required focal range, coherence, noise or spurious aberrations are not answered conclusively as of today. Indeed, non-unique reconstructions, e.g. depending on the starting guess or other parameters in reconstruction algorithms are reported in the literature [74–76].

1.3.3.2 Off-axis holography

Off-axis electron holography allows to reconstruct the phase of the sample by interfering a reference plane wave with the wave scattered by the object. Usually, the electron beam is split above the sample with an electron biprism and then re-interfered in the image plane on the detector. Fig. 1.8 shows an optical setup in the electron microscope. The resulting image intensity, if the plane waves are

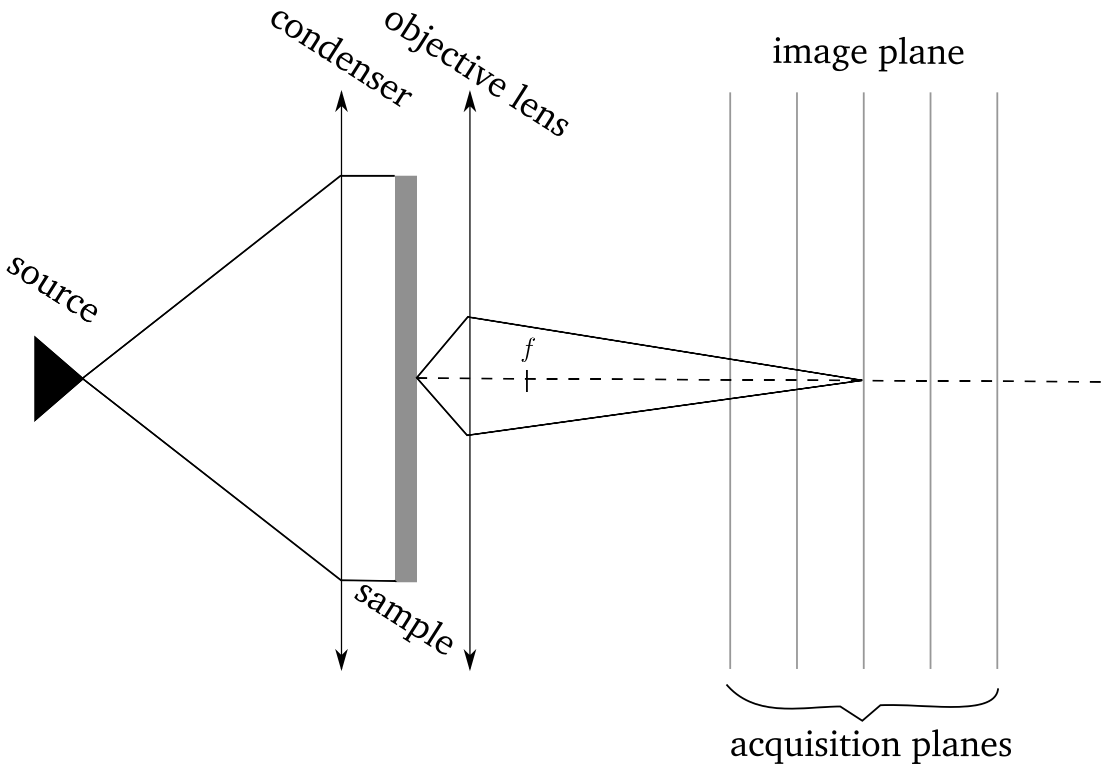

Figure 1.7: Simplified optical setup for inline electron holography. The defocus of the objective lens is varied and at each defocus an image is taken.

mutually inclined under an angle β, is an interference pattern with the carrier frequency $\mathbf{q}_c = k_0\beta$

$$I_h(\mathbf{r}) = I_0 + A^2(\mathbf{r}) + 2\,\mu_c A(\mathbf{r})\cos(2\pi\mathbf{q}_c\mathbf{r} + \phi(\mathbf{r})) \tag{1.63}$$

where $\mu_c \leq 1$, the degree of coherence, dampens the fringe contrast of the sinusoidal interference term. The amplitude and phase terms in the hologram can be easily separated by a Fourier transform of the hologram, yielding

$$\begin{aligned}\mathcal{F}[I_h(\mathbf{r})] = I_0\delta(\mathbf{q}) + \mathcal{F}[A^2(\mathbf{r})] + \delta(\mathbf{q} - \mathbf{q}_c) \otimes \mathcal{F}[A(\mathbf{r})\exp(i\phi(\mathbf{r}))] \\ + \delta(\mathbf{q} + \mathbf{q}_c) \otimes \mathcal{F}[A(\mathbf{r})\exp(-i\phi(\mathbf{r}))],\end{aligned} \tag{1.64}$$

a center band and two sidebands. The sidebands contain the full phase information of the sample, thus enabling simple phase recovery for a pure state. This becomes clear when calculating the ambiguity function of the off-axis hologram

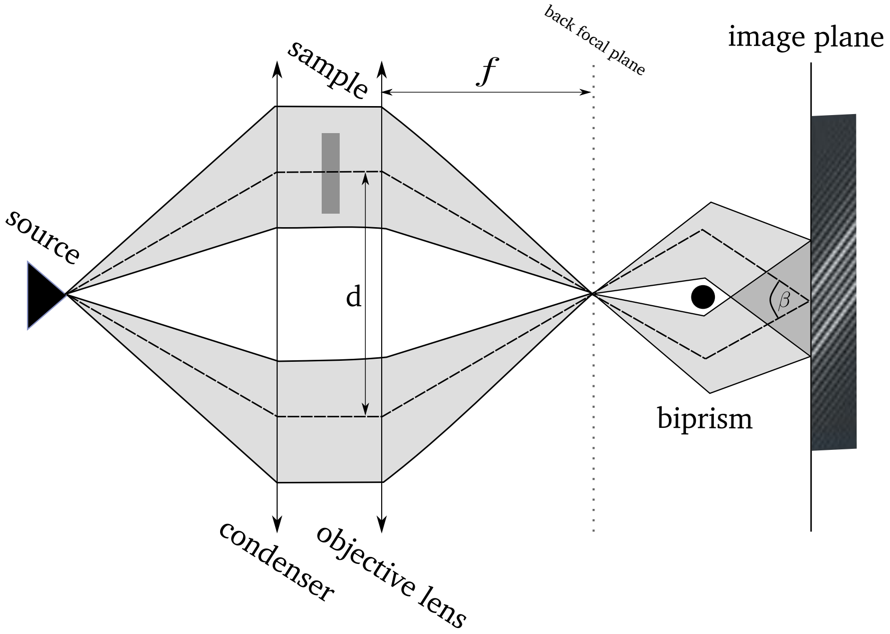

Figure 1.8: Simplified optical setup for off-axis electron holography. The electron beam is split by a biprism into a reference wave and the wave that traverses the sample. Behind the sample, the wave are re-interfered in the image plane of the objective lens.

[53]. As mentioned in section 1.2.10, the hologram's Fourier spectrum is the cross section of the ambiguity function at $\mathbf{p} = 0$:

$$\begin{aligned}\chi(\mathbf{q},\mathbf{p}) = {} & \chi_{++}(\mathbf{q},\mathbf{p}) e^{\frac{i}{2}(\mathbf{qd}+\mathbf{pq}_c)} + \chi_{--}(\mathbf{q},\mathbf{p}) e^{-\frac{i}{2}(\mathbf{qd}+\mathbf{pq}_c)} \\ & + \chi_{+-}(\mathbf{q}+\mathbf{q}_c,\mathbf{p}+\mathbf{d}) + \chi_{-+}(\mathbf{q}-\mathbf{q}_c,\mathbf{p}-\mathbf{d}).\end{aligned} \tag{1.65}$$

This is depicted in Fig. 1.9. The separation of the sidebands from the center band is given by the incidence angle β on the detector, which determines the carrier frequency. The holographic shear $\mathbf{d}$ is then used to perform the quantum state reconstruction. The terms with subscript $++$ and $--$ are the center band terms, while the terms with subscript $+-$ and $-+$ are the sideband terms. The sideband terms are shifted by $\mathbf{q}_c$ in Fourier space and $\mathbf{d}$ in real space, respectively, therefore the a pure state can be recovered from a single cross-section of the ambiguity function when the shift is larger than the bandwidth limit of the object Fourier spectrum.

The reasons why off-axis electron holography is not used today for imaging of biological specimens are rather of practical nature. The need for a vacuum area for the reference wave to pass through close to the region of interest complicates sample preparation, and in the worst case a thin area of specimen support

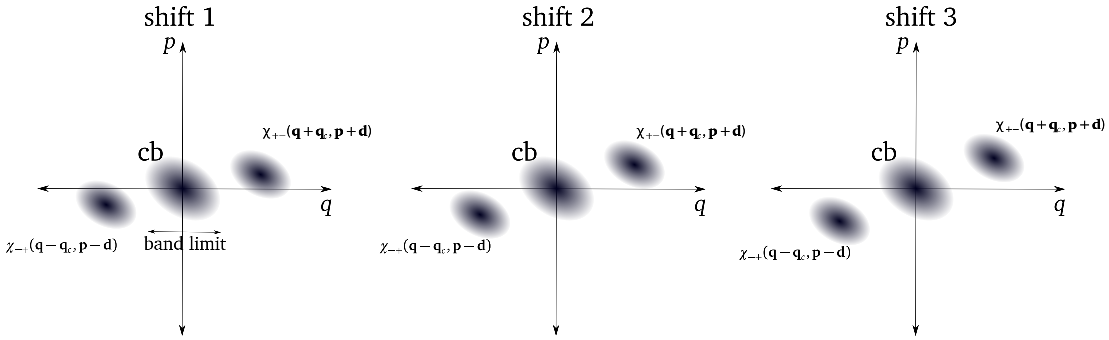

Figure 1.9: Quantum state reconstruction by off-axis holography by measuring the cross-section $\chi(\mathbf{q}, \mathbf{p} = 0)$ of the ambiguity function and varying the holographic shear $\mathbf{d}$. Covering the whole space of $\mathbf{d}$ requires not only changing the biprism voltage but also its position and orientation. Additionally, for shears larger than the coherence length, the interference term strongly attenuates.

must be used. This increases the phase error in the image because it breaks the plane wave assumption. Additionally, at least two electron biprisms need to be inserted into the column, which further increases the cost of already expensive cryo-EM equipment. The first demonstration of off-axis electron holography of a biological specimen was performed by Kawasaki *et al.* with ferritin proteins in 1986 [77]. The scarcity of successful experiments thereafter hints at the experimental difficulty. The next successful experiments were performed by Aoyama, Lai & Ru on bacterial flagellum [78] and tobacco mosaic virus. Since the introduction of direct electron detectors there have been no additional experimental attempts at applying the technique on biological samples.

1.3.3.3 STEM Ptychography

Ptychography, first proposed in 1969 [11, 12], solves the phase retrieval problem by collecting a set of far-field diffraction patterns at a multitude of overlapping probe positions. A simplified optical setup is depicted in Fig. 1.10. If the object is scanned with an evenly spaced lattice, this results an a 4-dimensional data array, which can be mathematically expressed as:

$$M(\mathbf{q}, \mathbf{x}) = \left| \int \psi(\mathbf{r}) T(\mathbf{r} - \mathbf{x}) e^{2\pi i \mathbf{r}\mathbf{q}} \, \mathrm{d}\mathbf{r} \right|^2, \tag{1.66}$$

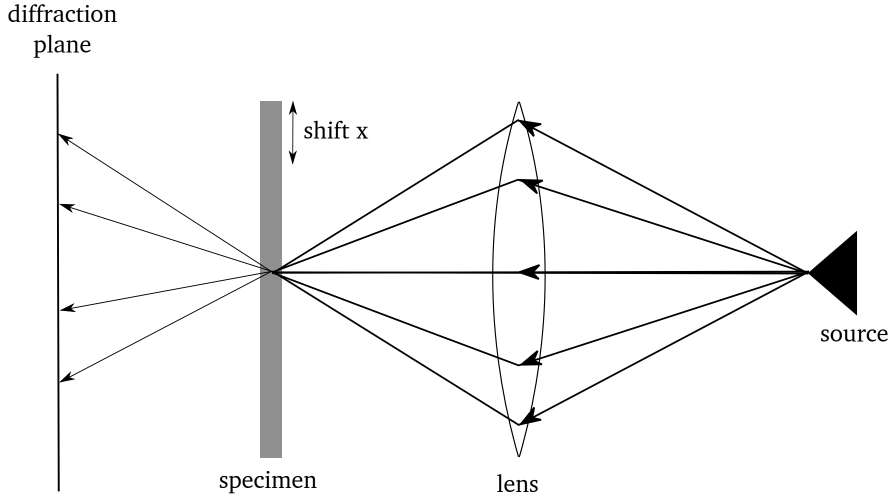

Figure 1.10: Simplified optical setup for ptychography. The beam is shifted over the object in the sample plane over the object or vice versa, depending on the experimental feasibility. In the STEM, the beam can be scanned over the sample with dwell times of a few μs

where $\mathbf{q}$, $\mathbf{r}$ and $\mathbf{x}$ are the coordinates in the detector plane, the sample plane, and of the probe scan position respectively. Expanding the above equations into integral form yields

$$M(\mathbf{q},\mathbf{x}) = \iint \tilde{\psi}(\mathbf{r})\tilde{\psi}^*(\mathbf{r})\tilde{T}(\mathbf{r}-\mathbf{x})\tilde{T}^*(\mathbf{r}-\mathbf{x}) \exp(2\pi i\mathbf{q}\cdot(\mathbf{r}_1-\mathbf{r}_2))\,\mathrm{d}\mathbf{r}_1\,\mathrm{d}\mathbf{r}_2 \tag{1.67}$$

Taking the Fourier transform with respect to $\mathbf{q}$ and the inverse Fourier transform with respect to $\mathbf{x}$ yields

$$\mathcal{F}_{\mathbf{q}}\left[\mathcal{F}_{\mathbf{x}}\left[M\right]\right](\mathbf{r},\mathbf{v}) \equiv H(\mathbf{r},\mathbf{v}) \tag{1.68}$$

$$H(\mathbf{r},\mathbf{v}) = \int \psi(\mathbf{b}-\mathbf{r})\psi(\mathbf{b})e^{-2\pi i\mathbf{bv}}\,\mathrm{d}\mathbf{b} \tag{1.69}$$

$$\cdot\int T(\mathbf{c}-\mathbf{r})T(\mathbf{c})e^{2\pi i\mathbf{cv}}\,\mathrm{d}\mathbf{c}\,. \tag{1.70}$$

This equation, in turn, can be written as a product of two ambiguity functions (Eq. (1.52))

$$H(\mathbf{r},\mathbf{v}) = \chi_\psi(\mathbf{r},-\mathbf{v})\chi_T(\mathbf{r},\mathbf{v}), \tag{1.71}$$

or equivalently, as a convolution of the probe and transmission function Wigner functions along all phase space dimensions,

$$H(\mathbf{r},\mathbf{v}) = W_\psi(\mathbf{r},\mathbf{v}) \otimes W_T(\mathbf{r},\mathbf{v}). \tag{1.72}$$

This means, if the Wigner function of the incoming electron wave is known, it can be deconvolved from the 4-dimensional dataset and the Wigner function of the transmission function *T* recovered. Thus this method of reconstruction was termed Wigner Distribution Deconvolution (WDD) [13]. It was first described in 1989 by Bates & Rodenburg [13, 79] and demonstrated with electrons for a crystalline sample in 1995 [14] and with X-rays for a non-crystalline sample in 1996 [15]. Acquiring a ptychographic dataset for WDD requires the instrument to be stable during the acquisition and for the scanning to be precise within the sub-pixel range, because errors in the positions or sample drift can not be corrected after the fact. It took until the arrival of fast pixelated electron detectors, before the technique became practicable for electron microscopy.
Typically, WDD dataset is collected with a step size that equals the maximum transferred resolution, which is twice the half-convergence angle of the condenser aperture. Because the 4-dimensional data set encodes only two 2 dimensional functions, it is highly redundant and the sampling may be reduced without hampering the reconstruction as discussed in the following chapter.

1.3.3.4 Fourier Ptychography

The reciprocity principle [80] states that a STEM can be regarded as a conventional TEM (CTEM) run in reverse, i.e. any particular point in the diffraction plane of the specimen corresponds to an angular position of the source in CTEM, while the source in STEM lies at the same position as one point int the image plane of CTEM. This is of course only the case of the scattering within the sample obeys time reversal symmetry, which is valid when the first Born approximation holds [81].
Therefore, an equivalent experiment to STEM ptychography can be obtained if the ray paths are inverted. This corresponds to an experiment where the sample is illuminated with a tilted plane wave, and an aperture is placed in the back focal plane of the objective lens to cut off electron that are scattered outside a maximum angle. This was is pictured in Fig. 1.11. This type of experiment was described by Rodenburg & Bates in 1992 [13], and has recently become very popular in the field of light microscopy [82, 83]. In the TEM this type of experiment has been pioneered by the group of Angus Kirkland in Oxford [84–86], where it was mainly applied to atomic resolution imaging. A problem for the implementation of Fourier ptychography in the TEM is that usually an objective aperture cannot be used because it charges up asymmetrically when it is illuminated by a tilted beam, and therefore introduces asymmetric phase changes which vary during the experiment and need to be accounted for. Also the de-

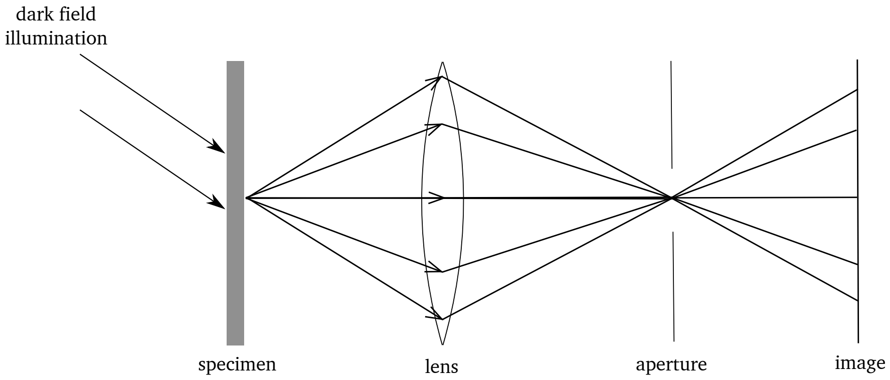

Figure 1.11: Simplified optical setup for Fourier ptychography. The object is illuminated with tilted plane waves and a set of dark field real-space images is recorded on the detector.

termination of aberration parameters of the imaging system is important in this setup, and the determination of these parameters become difficult at low electron doses. The phase space description of Fourier Ptychography was analyzed in [82] and it was shown that the Fourier ptychographic data set is rotated by 90° with respect to the conventional ptychography dataset. Therefore, the same methods of deconvolution as discussed for conventional ptychography can be applied for Fourier ptychography.

1.3.3.5 Possible single-shot experiments for low-dose quantum state reconstruction

As mentioned in the introduction, a very impactful possible application of a low-dose phase contrast method is to study dynamics of biological specimens in the liquid environment. The completion of a pulsed cold field emission diffraction setup in the Miller group in the near future will allow to perform time-resolved experiments with computational phase contrast techniques. We therefore discuss the possibilities for single-shot phase retrieval that were considered as part of this thesis regarding coherence requirements and difficulty of implementation.

Single-shot off-axis holography

In principle, single-shot off-axis holography is possible with a pulsed electron source and the same experimental configuration as discussed in section 1.3.3.2. Due to too high coherence requirements, this experiment has so far only been performed in the visible light regime [87, 88]. For an experiment with electrons, the requirement of a fully coherent beam across the field of view would mean to choose either a small field of view or to cut off most of the electrons directly after the source to increase the coherence of the beam. Besides, the number of electron optical elements needed increases the amount of experimental development needed for the use in self-built electron microscopes or diffraction setups. It is however pursued in some ultrafast TEMs with Schottky or cold field emitters [89, 90].

Single-shot inline holography with a phase modulation

Single-shot coherent diffractive imaging with nearly plane-wave illumination is popular in the X-ray community because of its simple experimental implementation. However, the high dynamic range requirements on detectors and the relative susceptibility to noise compared to other techniques do not make it attractive for low-dose imaging with electrons. Furthermore, electron optics allow easy manipulation of the convergence angle, such that more traditional inline holography schemes become feasible. Nevertheless, traditional inline holography also suffers from uniqueness problems and relies on a fully coherent electron beam.

A scheme that might be attractive for low-dose inline holographic phase retrieval was demonstrated by Zhang *et al.* [91, 92], where a phase mask is inserted behind the sample to impose additional phase profile on the diffracted wave and distribute the intensity more evenly over the whole detector.

Introducing material behind the sample was already considered suboptimal for low-dose imaging in section 1.3.2, therefore a dose-efficient way of performing a similar experiment would be to insert a phase mask before the sample, i.e., in the aperture plane of an electron microscope. An application of this scheme to electron ptychography is discussed in chapter 4.

A downside of this scheme is that the phase mask must be characterized before the single-shot experiment, either by ptychography or other methods. If the electron source is very stable, it could also be characterized beforehand, such that the reconstruction amounts to a simple phase retrieval of the object transmission function.

Single-shot ptychography

Single-shot ptychography was first proposed and demonstrated in 2014 by Pan, Liu & Zhu to overcome the scanning time limitation of ptychography [93]. In the original proposal, a diffraction grating was used to split the beam into many identical copies, differing only by a linear phase gradient. A second paper [94, 95] introduced more variants, e.g. the combination of a pinhole array and a focusing lens, depicted in Fig. 1.12. This implementation is particularly attractive for electron diffraction experiments, as it only requires the beam to coherently fill a single pinhole because no coherent interference is required between the beams from different pinholes, as they constitute distinct measurements. By varying the pinhole size, the experiment can be adjusted to the lateral coherence properties of the electron source. The experiment does, however, require a detector with a large number of pixels, as one records multiple, spatially separated diffraction patterns at once. It is also for the promising properties for future single-shot experiments at pulsed electron diffractometers that we selected ptychography as the method of choice for further investigations.

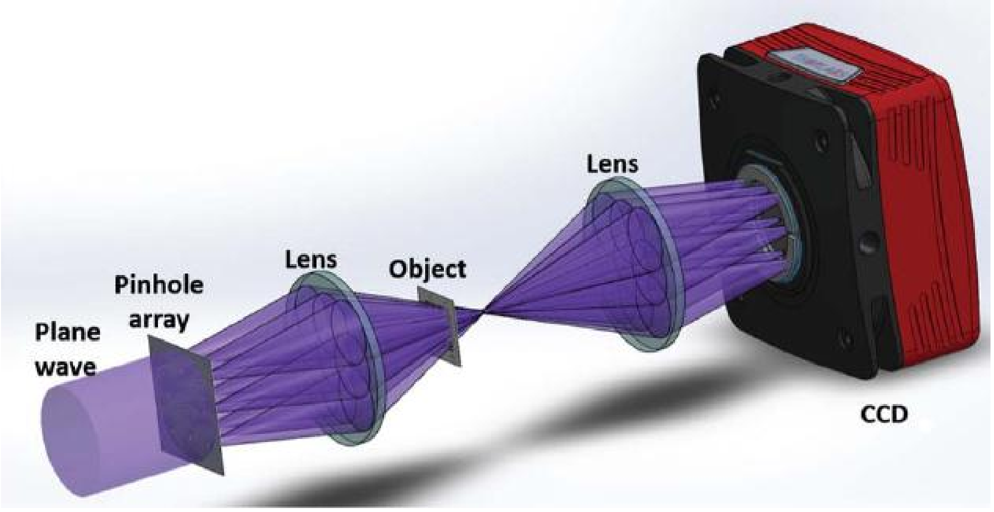

Figure 1.12: Simplified optical setup for single-shot ptychography. Reproduced from Sidorenko & Cohen [95]

2 Low-dose electron ptychography via non-convex Bayesian optimization

In this chapter we connect ptychographic reconstruction to the *generalized phase retrieval problem* defined in the previous chapter. We discuss the shortcomings of existing algorithms with respect to low-dose experiments and present a Bayesian algorithm thats solves the ptychographic phase retrieval problem efficiently at low doses. We then extend this algorithm to the case when the probe wave function is unknown, and the case when the probe wave function is unknown and partially coherent.

2.1 Mathematical formulation of ptychographic phase retrieval

We now give a more general definition of ptychography in the formalism of generalized phase retrieval, to allow for arbitrary scan patterns. We define the two-dimensional grid with size $n_1 \times n_2 \in \mathbb{N} \times \mathbb{N}$ and length scale $r > 0$ as $D_r^{n_1 \times n_2} := (r\alpha, r\beta)_{\alpha,\beta=0}^{n_1,n_2} \subset \mathbb{R}^2$. The two-dimensional complex transmission function of the object is discretized as a $n_1 \times n_2$ matrix and denoted as $T : D_{r_\mathrm{d}}^{n_1 \times n_2} \to \mathbb{C}$, where $r_\mathrm{d} > 0$ is the diffraction-limited length scale as introduced above. The object is illuminated by a small beam with known distribution, and discretized as a $m_1 \times m_2$ matrix, denoted as $\psi : D_{r_\mathrm{d}}^{m_1 \times m_2} \to \mathbb{C}$. For simplicity, in this thesis we only consider the case $n_1 = n_2$ and $m_1 = m_2$, i.e. a uniform discretization in both axes. The experiment is depicted in Fig. 2.1. In the experiment, the beam is moved over the sample to positions $\mathbf{r}_i$, and illuminates $K > 1$ subregions to obtain K diffraction images. The far-field intensity measured for position i is then

$$I_{i\,\mathbf{q}} = |\mathcal{F}[\phi_{i\,\mathbf{r}}]|^2 = |\mathcal{F}[\psi(\mathbf{r} + \mathbf{r}_i) \cdot T(\mathbf{r})]|^2, \qquad i \in \{0, ..., K\}, \tag{2.1}$$

where the real-space coordinates are discretized in steps of r_d, and reciprocal-space coordinates in steps of $(m_{\{1,2\}} r_\mathrm{d})^{-1}$. Mathematically, ptychographic reconstruction can be understood as a special case of the *generalized phase retrieval problem* defined in 1.2.12. We follow the notations in [97] to write the ptychographic phase retrieval problem in this form. First, we vectorize the transmission function and the incoming wave function as $\mathbf{T}^\vee \in \mathbb{C}^N$ with $N = n_1 \cdot n_2 \in \mathbb{N}$ and $\psi^\vee \in \mathbb{C}^M$ with $M = m_1 \cdot m_2 \in \mathbb{N}$ by stacking the entries of the 2D arrays row by row. We introduce the matrix $R_{(i)} \in \mathbb{R}^{M \times N}$, which extracts an $M = m_1 \times m_2$ sized

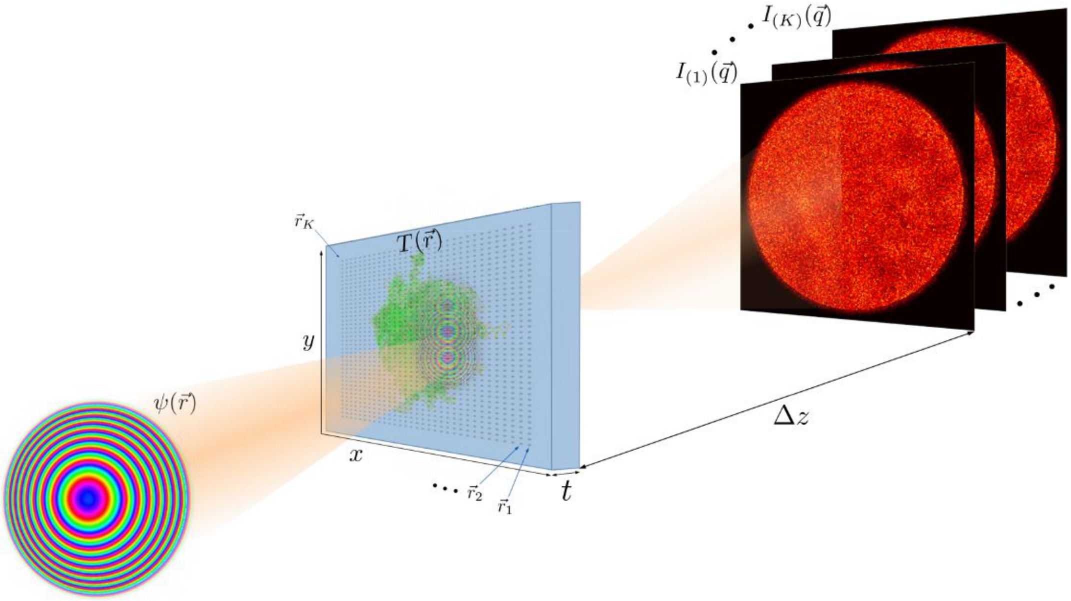

Figure 2.1: Simplified optical setup for ptychography with arbitrary scan positions $\{\mathbf{r}_i\}$. The coherent wave function $\psi(\mathbf{r})$ is shifted over the sample, which in the previously described approximations can be treated as as complex transmission function $T(\mathbf{r})$. At positions $\mathbf{r}_i$, a far-field diffraction pattern $I_{i\mathbf{q}} = |\mathcal{F}[\psi(\mathbf{r}+\mathbf{r}_i)\cdot T(\mathbf{r})]|^2$ is recorded by a detector placed a distance Δz away from the sample. The sample thickness t must fulfill the thickness requirements discussed in section 3.1.2. (from Pelz *et al.* [96])

area centered at position $\mathbf{r}_i$ from $\mathbf{T}^\vee$. With these notations in place, the relation between the noise-free diffraction measurements collected in a ptychography experiment and $\mathbf{T}^\vee$ can be represented compactly as

$$\mathbf{I} = |\mathbf{F}\Phi(\mathbf{T}^\vee, \psi^\vee)|^2. \tag{2.2}$$

$\Phi(\mathbf{T}^\vee, \psi^\vee)$ is a linear operator that generates K exit waves from the incoming wave function and the complex transmission function and $\mathbf{F}$ is a block-diagonal matrix with th 2D discrete Fourier transform (DFT) matrix as the block. It can be expressed as

$$\Phi(\mathbf{T}^\vee, \psi^\vee) = \operatorname{diag}(\mathbf{S}\psi^\vee)\,\mathbf{R}\mathbf{T}^\vee = \operatorname{diag}(\mathbf{R}\mathbf{T}^\vee)\,\mathbf{S}\psi^\vee \tag{2.3}$$

where $\mathbf{R} = \left(R_{(1)}R_{(2)}\ldots R_{(K)}\right)^T \in \mathbb{R}^{KM\times M}$ is the matrix that crops out all illuminated regions from the transmission function. $\mathbf{S} \in \mathbb{R}^{KM\times M}$ is a $K\times 1$ block matrix with the $M \times M$ identity matrix as the block that stacks K exit waves on top of each other. The action of the different operators is depicted in Fig. 2.2. We further

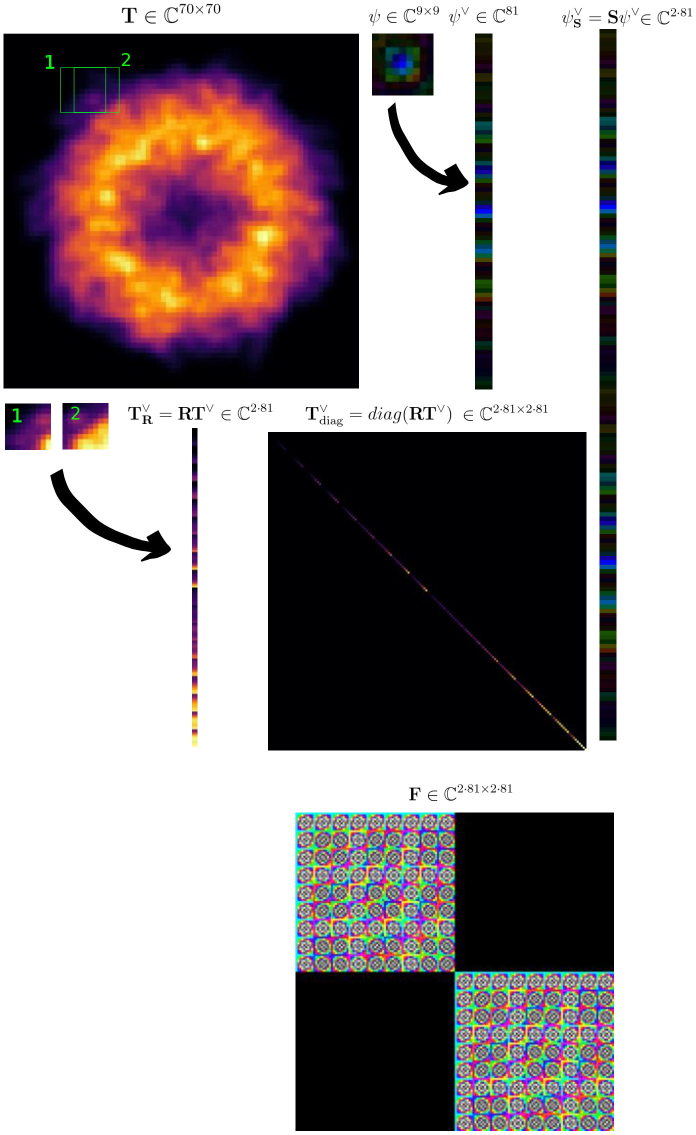

Figure 2.2: Depiction of the ptychographic operators. A transmission function of a proteasome particle $\mathbf{T}$ with 70 × 70 pixels is cropped at two positions with 9 × 9 pixels. The outcome of the operation $\mathbf{RT}^{\vee}$ is therefore a 162-dimensional vector. For the multiplication with the wave function, the vector is written in the matrix diagonal, such that the multiplication with the wave function ψ is the matrix multiplication of the stacked wave function $\mathbf{S}\psi^{\vee}$ with this diagonal matrix. The operator $\mathbf{F}$ for the case of two positions is a 2M × 2M block diagonal matrix with the 2D DFT matrix as the block. Because of the sparsity of the involved matrices, the operations are usually performed directly on the non-zero entries to save memory and computation.

define the matrices $\mathbf{P} := \mathbf{F}\mathrm{diag}\left(\mathbf{S}\psi^{\vee}\right)\mathbf{R} \in \mathbb{C}^{KM\times N}$ and $\mathbf{Q} := \mathbf{F}\mathrm{diag}\left(\mathbf{R}\mathbf{T}^{\vee}\right)\mathbf{S} \in \mathbb{C}^{KM\times N}$ to abbreviate the gradient calculations in the next chapter.
Comparing $\mathbf{P}$ and $\mathbf{Q}$ with Eq. (1.58) makes clear that these are the quantum mechanical measurement operators for probe and object respectively.

$$\mathbf{I} = |\mathbf{P}\mathbf{T}^{\vee}|^2 = |\mathbf{Q}\psi^{\vee}|^2, \tag{2.4}$$

In the last decades many algorithms to solve this problem have been devised, only a few of which we review with regards to low-dose reconstruction in the following section. For the subsequent analysis, we denote the KM row vectors of $\mathbf{P}$ and $\mathbf{Q}$ as $\mathbf{p}_{\mathsf{k}}$ and $\mathbf{q}_{\mathsf{k}}$ respectively, so that for a single intensity measurement

$$I_{\mathsf{k}} = \left|\langle \mathbf{q}_{\mathsf{k}}|\psi^{\vee}\rangle\right|^2 = \left|\langle \mathbf{p}_{\mathsf{k}}|\mathbf{T}^{\vee}\rangle\right|^2, \quad \mathsf{k} = 1, ..., \mathsf{KM}. \tag{2.5}$$

2.2 Discussion of existing algorithms

The most prominent iterative algorithms to solve the ptychographic phase retrieval problems are the difference map (DM) algorithm [98], and the extended ptychographic iterative engine (ePIE) [99]. The difference map belongs to the family of algorithms which use projections onto non-convex sets to reach a fixpoint, i.e., the solution lying at the intersection of the two sets. Both algorithms use the following amplitude projection to constrain the model intensities to the measurements:

$$P_{\mathbf{a}}\phi = \mathcal{F}^{\dagger}\left[\frac{\mathcal{F}[\phi]}{|\mathcal{F}[\phi]|}\mathbf{a}\right], \tag{2.6}$$

where $\mathbf{a} = \sqrt{\mathbf{I}}$ are the measured amplitudes and ϕ is the exit wave. This projection is only exact in the noiseless case, and in the presence of noise introduces errors which usually average out over the high number of measurements at the high counts at which diffraction patterns are recorded, or are explicitly averaged by performing many reconstructions with different starting points and then averaging the result of these reconstructions. The problem with the exact projection at low counts becomes clear when looking at the measurements with zero intensity. At the low doses needed for cryo-EM, the diffraction patterns contain many pixels with zero intensity even in the bright field. The exact projection sets the intensity of the wave function to zero at spatial frequencies where the probe has the highest probability density although single measurements may contain zero intensity, therefore phase retrieval fails with the DM and ePIE if the bright field intensities become very low [100, 101], and statistical reconstruction methods have to be used. Thibault & Guizar-Sicairos [102] have analyzed maximum likelihood methods in conjunction with a conjugate gradient update rule as a refinement step, after the DM algorithm has converged. They demonstrate an improvement by two orders of magnitude of the signal-to-noise ratio (SNR) of the reconstructions, compared to a reconstruction using the DM algorithm alone. They note, however, that starting directly with maximum likelihood optimization often poses convergence problems.

If noise needs to be accounted for in projection-based algorithms, the exact projection of DM and ePIE can be replaced by a proximal projection, as has been done by more recent algorithms [103, 104].

2.3 Non-convex Bayesian optimization for ptychography

Due to the lack of phase retrieval algorithms with convergence guarantees, the mathematical community has recently picked up the problem, and a host of new algorithms with provable convergence have been developed. While we do not elaborate on them here we point the interested reader to the review articles [105, 106] and the article [107], which refers to the most recent developments. Here, we focus on developments which specifically target low-dose applications. Notable in this area is the work by Katkovnik & Astola [108], which in addition to the maximum likelihood estimate introduces a transform-domain sparsity constraint on the object and optimizes two objective functions in an alternating fashion: one for the maximizing the likelihood, and one for obtaining a sparse representation of the transmission function. However, instead of including the Poisson likelihood directly, an observation filtering step is performed with a Gaussian likelihood. To obtain a sparse representation of the object, the popular BM3D denoising filter is used [109]. During the writing of this thesis, Yang *et al.* suggested using the Wigner Distribution Deconvolution technique for low-dose ptychography [110], however no statistical treatment of the measurement process is included so far.

A detailed evaluation of all the different algorithms treating noisy phase retrieval proposed so far, including noise suppression in Wigner deconvolution [111], would be very interesting, however because iterative ptychography has been patented and open-source implementations of ptychographic reconstruction algorithms are aggressively prosecuted, reproducing the results of each publication is a major endeavor that we leave as future work.

In this work, we formulate ptychographic phase retrieval as a Bayesian inference problem, by rewriting the probability of the transmission function $\mathbf{T}^\vee$ given a set of measurements $\mathbf{y} = (y_1, y_2, \ldots, y_{KM})^T \in \mathbb{R}_+^{KM}$ according to Bayes' rule:

$$P(\mathbf{T}^\vee|\mathbf{y}) = \frac{P(\mathbf{y}|\mathbf{T}^\vee)\,P(\mathbf{T}^\vee)}{P(\mathbf{y})}. \tag{2.7}$$

It relates the probability a value of the transmission function T before collecting a measurement, $P(\mathbf{T}^\vee)$, to the probability after performing a measurement $\mathbf{y}$, $P(\mathbf{T}^\vee|\mathbf{y})$. $P(\mathbf{T}^\vee)$ is therefore called *prior probability*, while $P(\mathbf{T}^\vee|\mathbf{y})$ is called the *posterior probability*. The factor that relates the two quantities, $\frac{P(\mathbf{y}|\mathbf{T}^\vee)}{P(\mathbf{y})}$ is called *likelihood ratio*. It is the quotient of the *conditional probability* $P(\mathbf{y}|\mathbf{T}^\vee)$ of a measurement given a certain transmission function, and the *marginal probability* $P(\mathbf{y})$ of a measurement. In the literature, $P(\mathbf{y}|\mathbf{T}^\vee)$ is often called *likelihood*. Since the measurements y_i are independent and follow the Poisson distribution

$$y_i \sim \text{Poisson}(I_i(\mathbf{T}^\vee)), \tag{2.8}$$

the likelihood of the measurements $\mathbf{y}$ given a certain transmission function $\mathbf{T}^\vee$ is given by

$$P(\mathbf{y}|\mathbf{T}^\vee) = \prod_{i=0}^{KM} \frac{I_i(\mathbf{T}^\vee)^{y_i}}{y_i!} e^{-I_i(\mathbf{T}^\vee)}. \tag{2.9}$$

The prior distribution $P(\mathbf{T}^\vee)$ is usually chosen such that it favors realistic solutions, so that noise is suppressed in the reconstructed image. Here we evaluate two different models. A simple prior, suggested in [112], penalizes large gradients in the image with a Gaussian distribution on the gradient of the transmission function, which is also known as Tikhonov regularization:

$$P_{\text{Tikhonov}}(T) = \exp\left\{\left(-\frac{\mu_0}{\kappa}||\nabla T(\mathbf{r})||^2\right)\right\} = \exp\left\{\left(-\frac{\mu_0}{\kappa}\sum_{i=1}^{N}(\mathrm{D}_x\mathbf{T}^\vee)_i^2 + (\mathrm{D}_y\mathbf{T}^\vee)_i^2\right)\right\} \tag{2.10}$$

with $\kappa = 8\frac{N_{pix}^2}{N_\mathrm{m}||I||_1}$ chosen as in [112]. N_m is the total number of valid measurements, $N_{pix} * K$ in the case when the detector has no hot pixels. This scales the numerical value of the prior to be close to the likelihood, such that the weight μ_0 can take values between 1×10^{-1} and 1×10^{-2}. The effect of a strong Tikhonov regularization is a damping of strong gradients in the transmission function, therefore smoothing the image. D_x and D_y are the discrete forward difference operators. The second prior we evaluate is based on the work by Katkovnik *et al.* [108] and uses sparse modeling to denoise the transmission function:

$$P_{\text{sparse}}(\mathbf{T}^\vee) = \exp\left\{\left(-\mu||\mathbf{T}^\vee - \mathbf{T}_{\text{sparse}}^\vee||^2\right)\right\} \tag{2.11}$$

Here, $\mathbf{T}^{\vee}_{\text{sparse}}$ is built up by applying the BM3D collaborative filtering algorithm [109, 113]. As the BM3D algorithm was initially designed for natural real-valued images, we decompose the complex transmission function into real and imaginary part for the best denoising results [114]. The prior $P_{\text{sparse}}(T)$ reduces the difference between the denoised version of the current transmission function and the transmission function itself. We note that an extensive comparison of denoising phase retrieval algorithms was published in [113], which also evaluates BM3D denoising using an algorithm similar to the one presented here, and finds superior performance compared to other denoising strategies such as total variation or nonlocal means. We do not take into account the marginal likelihood $P(\mathbf{y})$ because it involves integrating over all possible values of the transmission function and would increase the computational load by a large amount. Because we aim for real-time reconstruction, we set the marginal likelihood of the measurements constant. Given the likelihood function $P(\mathbf{y}|\mathbf{T}^{\vee})$ and the prior distribution $P(\mathbf{T}^{\vee})$, we can now write the objective function for the maximum-a-posteriori (MAP) estimate:

$$\mathbf{T}^{\vee}_{\text{MAP}} := \underset{\mathbf{T}^{\vee}}{\operatorname{argmin}}\ \mathcal{L}_{\text{MAP}}(\mathbf{T}^{\vee}) = \underset{\mathbf{T}^{\vee}}{\operatorname{argmin}} \left(-\log\left(\frac{P(\mathbf{y}|\mathbf{T}^{\vee})P(\mathbf{T}^{\vee})}{P(\mathbf{y})} \right) \right). \tag{2.12}$$

The log-likelihood is given as

$$\mathcal{L}(\mathbf{T}^{\vee}) = \sum_{i=1}^{KM} \left[|\mathbf{p}_i\, \mathbf{T}^{\vee}|^2 - y_i \log(|\mathbf{p}_i\, \mathbf{T}^{\vee}|^2) \right], \tag{2.13}$$

with the row vectors $\mathbf{p}_i$ of the design matrix $\mathbf{P}$. The MAP objective functions are

$$\mathcal{L}_{\text{Tikhonov}-\text{MAP}}(\mathbf{T}^{\vee}) = \mathcal{L}(\mathbf{T}^{\vee}) + \frac{\mu_0}{\kappa} ||\nabla T(\mathbf{r})||^2 \tag{2.14}$$

and

$$\mathcal{L}_{\text{BM3D}-\text{MAP}}(\mathbf{T}^{\vee}) = \mathcal{L}(\mathbf{T}^{\vee}) + \mu_1 ||\mathbf{T}^{\vee} - \mathbf{T}^{\vee}_{\text{sparse}}||^2, \tag{2.15}$$

for the two prior models, respectively. We calculate the gradients of both expressions:

$$\nabla\mathcal{L}_{\text{Tikhonov}-\text{MAP}}(T) = \sum_{i=1}^{KM} \mathbf{p}_i\, \mathbf{T}^{\vee} \left(1 - \frac{y_i}{|\mathbf{p}_i\, \mathbf{T}^{\vee}|^2} \right) \mathbf{p}_i^{\dagger} + 2\frac{\mu_0}{\kappa} \sum_{i=1}^{N} (\mathrm{D}_x \mathbf{T}^{\vee})_i + (\mathrm{D}_y \mathbf{T}^{\vee})_i, \tag{2.16}$$

$$\nabla\mathcal{L}_{\text{BM3D}-\text{MAP}}(T) = \sum_{i=1}^{KM} \mathbf{p}_i\, \mathbf{T}^{\vee} \left(1 - \frac{y_i}{|\mathbf{p}_i\, \mathbf{T}^{\vee}|^2} \right) \mathbf{p}_i^{\dagger} + \mu_1 \left(\mathbf{T}^{\vee} - \mathbf{T}^{\vee}_{\text{sparse}} \right) \tag{2.17}$$

Since equations 2.14 and 2.15 are non-convex functions, there is no guarantee that standard gradient descent converges to a global minimum. Recently, a non-convex algorithm for the generalized phase retrieval problem with Poisson noise was presented [115], that provably converges to a global minimum with suitable initialization. It introduces an iteration-dependent regularization on the gradients of the likelihood to remove terms which have a negative effect on the search direction. Therefore it introduces a truncation criterion

$$\mathcal{E}^i(\mathbf{T}^\vee) = \left\{ \left| y_i - |\mathbf{p}_i\mathbf{T}^\vee|^2 \right| \leq \frac{\alpha_h}{KM} \|\mathbf{y} - \mathbf{I}\| 1 \frac{|\mathbf{p}_i\mathbf{T}^\vee|}{\|\mathbf{T}^\vee\| 2} \right\}, \tag{2.18}$$

that acts on the gradient of the likelihood and suppresses the gradient of measurements that are too incompatible with the reconstruction. The truncation parameter $\alpha_h \geq 5$ is described in [115]. The regularized likelihood gradient is then

$$\nabla \mathcal{L}_{\mathcal{E}^i}(\mathbf{T}^\vee) = \sum_{i \in \mathcal{E}^i(\mathbf{T}^\vee)}^{KM} \left[|\mathbf{p}_i \, \mathbf{T}^\vee|^2 - y_i \log(|\mathbf{p}_i \, \mathbf{T}^\vee|^2) \right]. \tag{2.19}$$

We compute the next step using conjugate gradient descent [116, 117], since this leads to much faster convergence compared to the update procedure described in Chen & Candes [115].

2.3.1 Initialization

Truncated spectral initialization for ptychography was first proposed by Marchesini *et al.* [97], based on the notion that the highest intensities in the diffraction pattern carry the strongest phase information. They compute the phase of the largest eigenvector of the following hermitian operator:

$$1_{|y_i|>\epsilon} \mathbf{F}\mathbf{P}(\mathbf{P}^\dagger\mathbf{P})^{-1}\mathbf{P}^\dagger\mathbf{F}^\dagger 1_{|y_i|>\epsilon}, \tag{2.20}$$

where ϵ is chosen such that the largest 20 percent of the intensities are allowed to contribute and **F** and **P** are defined as above. The largest eigenvalue of a sparse hermitian matrix can be efficiently computed either with power iterations [118], or with the Arnoldi method [119]. In [115], truncated spectral initialization with a truncation rule with $1_{|y_i|<\alpha_0^2\lambda_0^2}$ is used, with $\lambda_0 = \sqrt{\sum_{i=1}^{KM} y_i}$ and α_0 a free parameter. It is also important to note that the truncated spectral initialization only produces visually correct initial phase to a dose of roughly $100\, e^-/\text{Å}^2$. Fig. 2.3 a) shows the convergence behavior of different gradient update rules as a

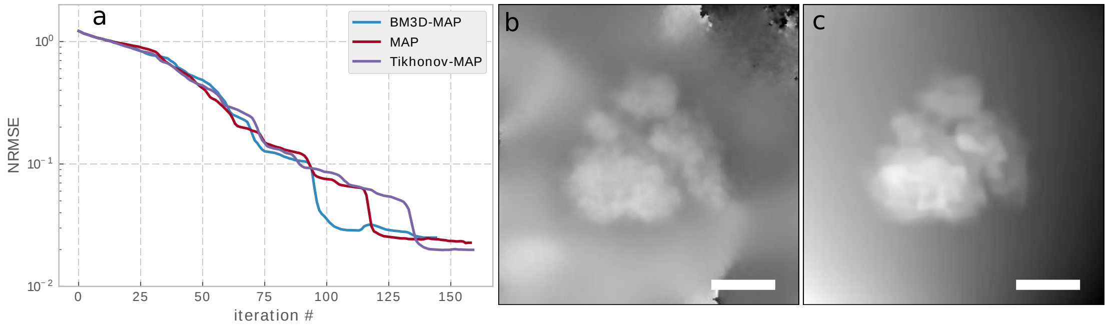

Figure 2.3: a) Normalized root mean square error (NMSR) of different gradient update rules as a function of iterations. The is defined in the Supplementary material. MAP refers to a constant prior. b) Example for the transmission function initialization T^0 after 70 power iterations, for an electron dose of $100\,e^-/\mathring{A}^2$, intensities were truncated at the 80th percentile. c) $\mathbf{T}^V_{\text{sparse}}$ for human ribosome after 60 iterations of BM3D-MAP. Scale bar is 10 nm (from [96]).

function of the normalized root mean square error. The normalized root mean square error is defined as

$$NMSR = \min_{\xi\in\{\xi\in\mathbb{C}:|\xi|=1\}} \frac{||\xi\mathbf{T}-\mathbf{T}_{model}||_2}{||\mathbf{T}||_2} \tag{2.21}$$

Fig. 2.3 b) shows an example initialization for a dose of $100\,e^-/\mathring{A}^2$. For doses below this value, we initialized the transmission function with unity transmission and normal-distributed phase with mean 0.1 and variance of 0.1. Even with random initialization we found no problem of convergence for all algorithms tested in this thesis. The full algorithm is described in Algorithm 1.

Algorithm 1 Truncated conjugate gradient descent for ptychography (TCG-PR)

```
Require: Set $\mathbf{T}_0^{\vee}$ by computing the largest eigenvector of Equ. 2.20, $\psi$, $\mathbf{I}$, maximum iteration number $Iter_{Max}$, and parameters $\square = \{\text{BM3D}, \text{Tikhonov}\}, s_0 = -\boldsymbol{\nabla}\mathcal{L}_{\square-MAP}(\mathbf{T}_0^{\vee}) * 10^{-2}$
Ensure: $\mathbf{T}_{\star}^{\vee} := T_{Iter_{Max}}^{\vee}$
for $k = 0$ to $Iter_{Max} - 1$ do
    Compute $l_k := \boldsymbol{\nabla}\mathcal{L}_{\square-MAP}(\mathbf{T}_k^{\vee})$
    Truncate $l_k$ according to equ. 2.18
    Compute $\beta_k = \frac{l_k^{\dagger}(l_k - l_{k-1})}{l_{k-1}^{\dagger} l_{k-1}}$
    Compute new search direction $s_k = l_k + \beta_k s_{k-1}$
    Line search $\alpha_k = \underset{\alpha}{\operatorname{argmin}}\,(\mathbf{T}_k^{\vee} + \alpha s_k)$
    $\mathbf{T}_{k+1}^{\vee} = \mathbf{T}_k^{\vee} + \alpha_k s_k$
end for
```

2.4 Bayesian optimization for blind ptychography - simultaneous probe reconstruction

The reconstruction and initialization routines discussed in the section above assumed that the probe wave function is known a priori. This is rarely the case in real experiments, unless one uses a probe aberration corrected STEM instrument and determines the aberration coefficients of the probe by other means [120]. Fortunately, a ptychographic data set provides enough information to simultaneously reconstruct the probe wave function. This has first been demonstrated in the X-ray community [121] and is since being used extensively in X-ray ptychography experiments. The derivation of the Bayesian reconstruction of the probe has been given in [102]. To extend our previous algorithm to include probe reconstruction, we include the wave function $\psi^\vee$ as a free parameter in the MAP objective function (2.13):

$$\mathcal{L}_{\text{MAP}}(\mathbf{T}^\vee, \psi^\vee) = -\log\left(\frac{P(\mathbf{y}|\mathbf{T}^\vee, \psi^\vee)P(\mathbf{T}^\vee)P(\psi^\vee)}{P(\mathbf{y})}\right). \tag{2.22}$$

Now, $P(\mathbf{y}|\mathbf{T}^\vee, \psi^\vee)$ is given by

$$P(\mathbf{y}|\mathbf{T}^\vee, \psi^\vee) = \prod_{i=0}^{KM} \frac{I_i(\mathbf{T}^\vee, \psi^\vee)^{y_i}}{y_i!} e^{-I_i(\mathbf{T}^\vee, \psi^\vee)}. \tag{2.23}$$

and the log-likelihood can be written as

$$\begin{aligned}\mathcal{L}(\mathbf{T}^\vee, \psi^\vee) &= \sum_{\text{i}=1}^{\text{KM}} \left[|\mathbf{p}_i\,\mathbf{T}^\vee|^2 - y_i \log(|\mathbf{p}_i\,\mathbf{T}^\vee|^2)\right] \\ &= \sum_{\text{i}=1}^{\text{KM}} \left[|\mathbf{q}_i\,\psi^\vee|^2 - y_i \log(|\mathbf{q}_i\,\psi^\vee|^2)\right].\end{aligned} \tag{2.24}$$

Then the derivative of the log-likelihood with respect to the probe wave function is

$$\frac{\partial \mathcal{L}}{\partial \psi^\vee} = \sum_{\text{i}=1}^{\text{KM}} \mathbf{q}_i \psi^\vee \left(1 - \frac{y_i}{I_i}\right) \mathbf{q}_i^\dagger \tag{2.25}$$

We found that doing a full gradient update for probe and object with all available data does not converge well, and therefore adapted batch-wise updates and a momentum-based optimization scheme. We also found that truncated gradients do not help the convergence in a blind ptychography setting, and therefore abandoned them for blind ptychography reconstructions. We define batch-wise operators in the following way: we divide the K diffraction patterns into n_{batch} batches, such that each batch has $\#_{batch} = \lceil K/n_{batch} \rceil$ diffraction patterns with indices $b_j = \{i_0, i_1, ..., i_{\#_{batch}}\}$. We define the partial operator $\mathbf{R}_{b_j} = (\mathbf{R}_{i_0} \mathbf{R}_{i_1} \ldots \mathbf{R}_{i_{\#_{batch}}}) \in \mathbb{R}^{n_{batch}M \times N}$, which crops the corresponding areas of the transmission function; and the partial operator $\mathbf{S}_{b_j} \in \mathbb{R}^{n_{batch}M \times N}$ which stacks n_{batch} wave functions on top of each other. This leads to partial operators $\mathbf{P}_{b_j} := \mathbf{F}\mathrm{diag}\left(\mathbf{S}_{b_j}\psi^{\vee}\right)\mathbf{R}_{b_j} \in \mathbb{C}^{n_{batch}M \times N}$ and $\mathbf{Q}_{b_j} := \mathbf{F}\mathrm{diag}\left(\mathbf{R}_{b_j}\mathbf{T}^{\vee}\right)\mathbf{S}_{b_j} \in \mathbb{C}^{n_{batch}M \times N}$. We denote the row-vectors of these matrices $\mathbf{p'}_i$ and $\mathbf{q'}_i$. We can then define a partial log-likelihood

$$\begin{aligned} \mathcal{L}_{b_j}(\mathbf{T}^{\vee}, \psi^{\vee}) &= \sum_{i=1}^{n_{batch}M} \left[|\mathbf{p'}_i \mathbf{T}^{\vee}|^2 - y_i \log(|\mathbf{p'}_i \mathbf{T}^{\vee}|^2) \right] \\ &= \sum_{i=1}^{n_{batch}M} \left[|\mathbf{q'}_i \psi^{\vee}|^2 - y_i \log(|\mathbf{q'}_i \psi^{\vee}|^2) \right] . \end{aligned} \tag{2.26}$$

With these definitions in place, the algorithm for blind ptychography is described as:

Algorithm 2 Stochastic accelerated gradient descent for blind ptychography (SAGD-BPR)

```
Require: Set $\mathbf{T}_0^\vee$, $\psi_0^\vee$, $\mathbf{I}$, maximum iteration number $Iter_{Max}$, and parameters
    $\square = \{\text{BM3D}, \text{Tikhonov}\}$, $n_{batch}$, momenta $\rho_{\psi^\vee}, \rho_{\mathbf{T}^\vee}$, learning rates $\gamma_{\psi^\vee}, \gamma_{\mathbf{T}^\vee}$,
    initial directions $b_{\psi^\vee} = \frac{\partial \mathcal{L}_{b_j}(\mathbf{T}_0^\vee, \psi^\vee)}{\partial \psi^\vee}, b_{\mathbf{T}^\vee} = \frac{\partial \mathcal{L}_{b_j}(\mathbf{T}^\vee, \psi_0^\vee)}{\partial \mathbf{T}^\vee}$
Ensure: $\mathbf{T}_\star^\vee := T_{Iter_{Max}}^\vee$
for $k = 0$ to $Iter_{Max} - 1$ do
    for $j = 0$ to $n_{batch}$ do
        Compute stochastic gradient $g_{\mathbf{T}^\vee} \leftarrow \frac{\partial \mathcal{L}_{b_j}(\mathbf{T}^\vee, \psi^\vee)}{\partial \mathbf{T}^\vee}$ with Eq. (2.16) or Eq. (2.17)
        $b_{\mathbf{T}^\vee} \leftarrow \rho_{\mathbf{T}^\vee} b_{\mathbf{T}^\vee} + g_{\mathbf{T}^\vee}$
        $\mathbf{T}^\vee \leftarrow \mathbf{T}^\vee - \gamma_{\mathbf{T}^\vee} b_{\mathbf{T}^\vee}$
        Compute stochastic gradient $g_{\psi^\vee} \leftarrow \frac{\partial \mathcal{L}_{b_j}(\mathbf{T}^\vee, \psi^\vee)}{\partial \psi^\vee}$ with Eq. (2.25)
        $b_{\psi^\vee} \leftarrow \rho_{\psi^\vee} b_{\psi^\vee} + g_{\psi^\vee}$
        $\psi^\vee \leftarrow \psi^\vee - \gamma_{\psi^\vee} b_{\psi^\vee}$
    end for
end for
```

2.5 Decoherence in ptychography

As discussed in section 1.2.8, as soon as a source with finite size is used, or instrumental instabilities introduce partial coherence in the measurement, the wave-function formalism has to be abandoned in favor a mixed-state description in terms of the density matrix $\hat{\rho}$. Thibault & Menzel [112] introduced the reconstruction of state mixtures into ptychography, so that a rank-L approximation of the density matrix of the incoming electron state can be reconstructed. This means that the measured intensity is now the incoherent sum of the coherent states transmitted through the sample and propagated to the far field:

$$I_{\mathsf{k}} = \mathrm{tr}\left(\sum_{\mathsf{l}=1}^{\mathsf{L}} \left|\psi_{\mathsf{l}}\right\rangle \left\langle\psi_{\mathsf{l}}\right| \left|\mathbf{q}_{\mathsf{k}}\right\rangle \left\langle\mathbf{q}_{\mathsf{k}}\right| \right), \quad \mathsf{k} = 1, ..., \mathsf{KM}. \tag{2.27}$$

For the formulation where the transmission function is the measured quantity, we define a new set of measurement matrices $\mathbf{P}_{\mathsf{l}}$ as follows:

$$\mathbf{P}_{\mathsf{l}} := \mathbf{F}\mathrm{diag}\left(\mathbf{S}\psi_{\mathsf{l}}^{\vee}\right)\mathbf{R} \in \mathbb{C}^{KM\times N}, \tag{2.28}$$

and we denote the KM row vectors of $\mathbf{P}_{\mathsf{l}}$ as $\mathbf{p}_{\mathsf{k},\mathsf{l}}$. We can then write the KM measured intensities as

$$I_{\mathsf{k}} = \sum_{\mathsf{l}=1}^{\mathsf{L}} \left|\langle\mathbf{q}_{\mathsf{k}}|\psi_{\mathsf{l}}{}^{\vee}\rangle\right|^2 = \sum_{\mathsf{l}=1}^{\mathsf{L}} \left|\langle\mathbf{p}_{\mathsf{k},\mathsf{l}}|\mathbf{T}^{\vee}\rangle\right|^2, \quad \mathsf{k} = 1, ..., \mathsf{KM}, \tag{2.29}$$

or in linear algebra formulation

$$\mathbf{I} = \sum_{\mathsf{l}=1}^{\mathsf{L}} |\mathbf{P}_{\mathsf{l}}\mathbf{T}^{\vee}|^2 = \sum_{\mathsf{l}=1}^{\mathsf{L}} |\mathbf{Q}\psi_{\mathsf{l}}^{\vee}|^2. \tag{2.30}$$

We can then write the log-likelihood as

$$\begin{aligned} \mathcal{L}(\mathbf{T}^{\vee}, \psi^{\vee}) &= \sum_{\mathsf{k}=1}^{KM} \sum_{\mathsf{l}=1}^{\mathsf{L}} \left[|\mathbf{p}_{\mathsf{k},\mathsf{l}}\,\mathbf{T}^{\vee}|^2 - y_i \log(|\mathbf{p}_{\mathsf{k},\mathsf{l}}, \mathbf{T}^{\vee}|^2) \right] \\ &= \sum_{\mathsf{k}=1}^{KM} \left[|\mathbf{q}_k\,\psi_{\mathsf{l}}^{\vee}|^2 - y_k \log(|\mathbf{q}_k\,\psi_{\mathsf{l}}^{\vee}|^2) \right]. \end{aligned} \tag{2.31}$$

The derivative with respect to the wave functions $\psi_{\mathsf{l}}^{\vee}$ and the transmission function $\mathbf{T}^{\vee}$ are then

$$\frac{\partial \mathcal{L}}{\partial \psi_{\mathsf{l}}^{\vee}} = \sum_{\mathsf{k}=1}^{\mathsf{KM}} \mathbf{q}_{\mathsf{k}} \psi_{\mathsf{l}}^{\vee} \left(1 - \frac{y_{\mathsf{k}}}{I_{\mathsf{k}}}\right) \mathbf{q}_{\mathsf{k}}^{\dagger}, \tag{2.32}$$

and

$$\frac{\partial \mathcal{L}}{\partial \mathbf{T}^{\vee}} = \sum_{\mathsf{k}=1}^{\mathsf{KM}} \sum_{\mathsf{l}=1}^{\mathsf{L}} \mathbf{p}_{\mathsf{k},\mathsf{l}}\, \mathbf{T}^{\vee} \left(1 - \frac{y_{\mathsf{k}}}{|\mathbf{p}_{\mathsf{k},\mathsf{l}}\, \mathbf{T}^{\vee}|^2}\right) \mathbf{p}_{\mathsf{k}}^{\dagger}, \tag{2.33}$$

With the new gradients in place, we can define the mixed-state extension of Algorithm 2 as follows in Algorithm 3. Reconstruction of the coherent modes of an electron wave has been demonstrated by Cao *et al.* [122] on a JEOL R005 microscope with cold field emission gun. To create a partially coherent beam, Cao *et al.* used a low spot size setting such that a large current passed through the condenser, and then used the selected area aperture with diameter 130 nm behind the sample to create a virtually confined, partially coherent beam. This setting is very impractical for low-dose ptychography, because electrons are blocked behind the sample and not all electrons collected.

Algorithm 3 Stochastic accelerated gradient descent for blind multi-mode ptychography (SAGD-BMMPR)

```
Require: Set $\mathbf{T}_0^{\vee}$, $\psi_{\mathsf{l}}^{\vee} \forall \mathsf{l} = 1, ..., \mathsf{L}$, $\mathbf{I}$, maximum iteration number $Iter_{Max}$, and parameters $\square = \{\text{BM3D}, \text{Tikhonov}\}$, $n_{batch}$, momenta $\rho_{\psi^{\vee}}, \rho_{\mathbf{T}^{\vee}}$, learning rates $\gamma_{\psi^{\vee}}, \gamma_{\mathbf{T}^{\vee}}$, initial directions $b_{\psi_{\mathsf{l}}^{\vee}} = \frac{\partial \mathcal{L}_{b_j}(\mathbf{T}_0^{\vee}, \{\psi_{\mathsf{l}}^{\vee}\})}{\partial \psi_{\mathsf{l}}^{\vee}}$, $b_{\mathbf{T}^{\vee}} = \frac{\partial \mathcal{L}_{b_j}(\mathbf{T}^{\vee}, \{\psi_{\mathsf{l}}^{\vee}\}}{\partial \mathbf{T}^{\vee}}$
Ensure: $\mathbf{T}_{\star}^{\vee} := T_{Iter_{Max}}^{\vee}$
for $k = 0$ to $Iter_{Max} - 1$ do
    for $j = 0$ to $n_{batch}$ do
        Compute stochastic gradient $g_{\mathbf{T}^{\vee}} \leftarrow \frac{\partial \mathcal{L}_{b_j}(\mathbf{T}^{\vee}, \{\psi_{\mathsf{l}}^{\vee}\})}{\partial \mathbf{T}^{\vee}}$ with Eq. (2.33)
        $b_{\mathbf{T}^{\vee}} \leftarrow \rho_{\mathbf{T}^{\vee}} b_{\mathbf{T}^{\vee}} + g_{\mathbf{T}^{\vee}}$
        $\mathbf{T}^{\vee} \leftarrow \mathbf{T}^{\vee} - \gamma_{\mathbf{T}^{\vee}} b_{\mathbf{T}^{\vee}}$
        Compute stochastic gradient $g_{\psi_{\mathsf{l}}^{\vee}} \leftarrow \frac{\partial \mathcal{L}_{b_j}(\mathbf{T}^{\vee}, \{\psi_{\mathsf{l}}^{\vee}\})}{\partial \psi^{\vee}}$ $\forall \mathsf{l} = 1, ..., \mathsf{L}$ with Eq. (2.32)
        $b_{\psi_{\mathsf{l}}^{\vee}} \leftarrow \rho_{\psi^{\vee}} b_{\psi_{\mathsf{l}}^{\vee}} + g_{\psi_{\mathsf{l}}^{\vee}}$    $\forall \mathsf{l} = 1, ..., \mathsf{L}$
        $\psi_{\mathsf{l}}^{\vee} \leftarrow \psi_{\mathsf{l}}^{\vee} - \gamma_{\psi^{\vee}} b_{\psi_{\mathsf{l}}^{\vee}}$    $\forall \mathsf{l} = 1, ..., \mathsf{L}$
    end for
end for
```

For low-dose ptychography, the gun lenses are usually tuned to a very coherent setting, and the current is still too high for the current generation of detectors to comfortably perform low-dose ptychography, as discussed in section 3.1.5. We illustrate this with a reconstruction from a dataset from a JEOL GrandARM microscope from the ePSIC facility in Harwell. The dataset was kindly shared by Prof. Pete Nellist and Prof. Angus Kirkland. The reconstruction of a graphene sample with Algorithm 3 at a dose of $1 \times 10^5\, e^-/\text{Å}^2$ is shown in Fig. 2.4. The reconstruction parameters were $Iter_{Max} = 20$, $\square =$ BM3D, $n_{batch} = 30$, $\rho_{\psi^\vee} = 0.7, \rho_{\mathbf{T}^\vee} = 0.5$ and learning rates $\gamma_{\psi^\vee} = 10^{-3}, \gamma_{\mathbf{T}^\vee} = 10^{-3}$. The data set was collected with a Medipix3 detector with a frame rate of 1 kHz at 80 keV with a focused beam of convergence half-angle $\alpha = 24.8$ mrad and with a step size of 20.5 pm. We see that even at high doses one usually does not have to worry about partial coherence, therefore we usually use only a single mode for the reconstruction of the experimental data sets. When detectors become faster over time and more of the available electron current can be used, the application of multi-mode reconstructions in electron ptychography could become important.

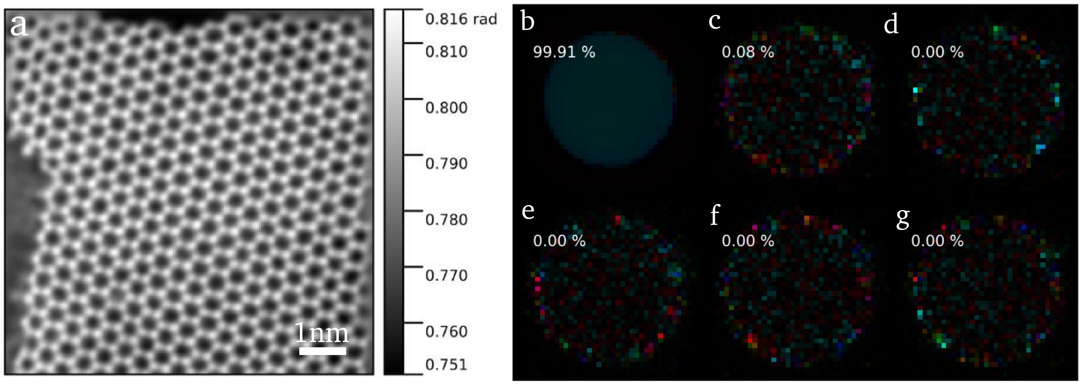

Figure 2.4: 6-mode reconstruction of single layer graphene. a) Reconstructed phase of the graphene sheet. b)-g) 6 reconstructed modes of the probe wave function in the aperture plane. The percentage displayed is the relative power of the mode $|c_m|^2$ (Eq. (1.29)). Nearly all the power is in the first mode and the higher modes seem to model detector inconsistencies rather than actual coherent modes of the beam.

2.6 Low-dose electron ptychography for single-particle cryo-EM

Having adapted and described the reconstruction algorithms for low-dose conditions, we now turn to analyzing one of many interesting applications: the application to structure determination of single particles. We perform multislice simulations with *slice*++ of three different biological macromolecules with molecular weights ranging from 64 kDa to 4 MDa. We choose the 64 kDa hemoglobin [123], the 706 kDa 20S proteasome from yeast [124], and the 4 MDa human ribosome [125]. Hemoglobin is one of the smallest proteins imaged to date with cryo-EM, 20S proteasome is a typical test-sample because of its symmetry, and the ribosome is an example for a large non-symmetric particle in the MDa range. We create atomic potential maps using the Matlab code InSilicoTem [33], with a thickness of 50 nm and at an electron energy of 300 keV. We use the isolated atom superposition approximation, without solving the Poisson-Boltzmann equations for the interaction between the molecule and the ions. We also do not model the amorphousness of the solvent, which was performed in [33] using molecular dynamics simulations, but was seen to have a negligible effect at very low doses. As described in [33], we model the imaginary part of the potential via the inelastic mean free path, creating a minimal transmission contrast between the vitreous ice and the protein. Using these potential maps, we simulate a ptychography experiment by cropping three-dimensional slices from the potential at several positions and propagate a coherent incoming wave through the slices using the methods described in [28] in the *slice*++ code. The final model for the formation of the intensity on the detector is described in section 1.2.

A notable difference both in simulation and practice is the fact that for cryo-EM, usually no pixel binning is applied to maximize the imaged area and increase throughput. Therefore, also high spatial-frequency regions with low values of DQE and NTF are used for image formation [126]. For ptychography, on the other hand, the detector can be heavily binned, as long as the real-space patch given by $\lambda \Delta z / d_{\mathrm{pix}} \equiv r_{\mathrm{d}} \cdot N_{\mathrm{pix}}$ still encompasses the probe beam on the sample and the sampling requirements discussed in section 3.1.3 are met. For typical detectors used in cryo-EM, this condition is fulfilled at bin sizes equivalent to a few percent of the Nyquist frequency. This leads to a near-constant DQE and a near-unity NTF, such that they can be omitted in the ptychography reconstructions, whereas we still include them in the simulation of the diffraction data. We note, however, that a convolution with a detector transfer function can be modeled with a partially coherent beam if necessary, as demonstrated in [112, 127].

We choose the Gatan K2 Summit as the detector for our simulations because it has the highest published DQE and MTF values at low spatial frequencies at 300 keV [126]. We note that direct detection cameras with frame rates of 1 kHz and above may be more suitable for high-throughput scanning experiments [43, 128, 129], but characteristics for these cameras at 300 keV are either not published or inferior to the K2 Summit. Assuming the K2 Summit for both ptychography and phase-contrast TEM simulations also simplifies a direct comparison between the two methods.

2.6.1 2D single-particle imaging: low-dose ptychography vs. Zernike phase contrast vs. phase contrast from defocus

Fig. 2.5 shows a comparison of low-dose ptychography reconstructions with currently used methods for single-particle imaging with electrons: defocus-based cryo-EM, and Zernike phase contrast cryo-EM with a Volta phase-plate.

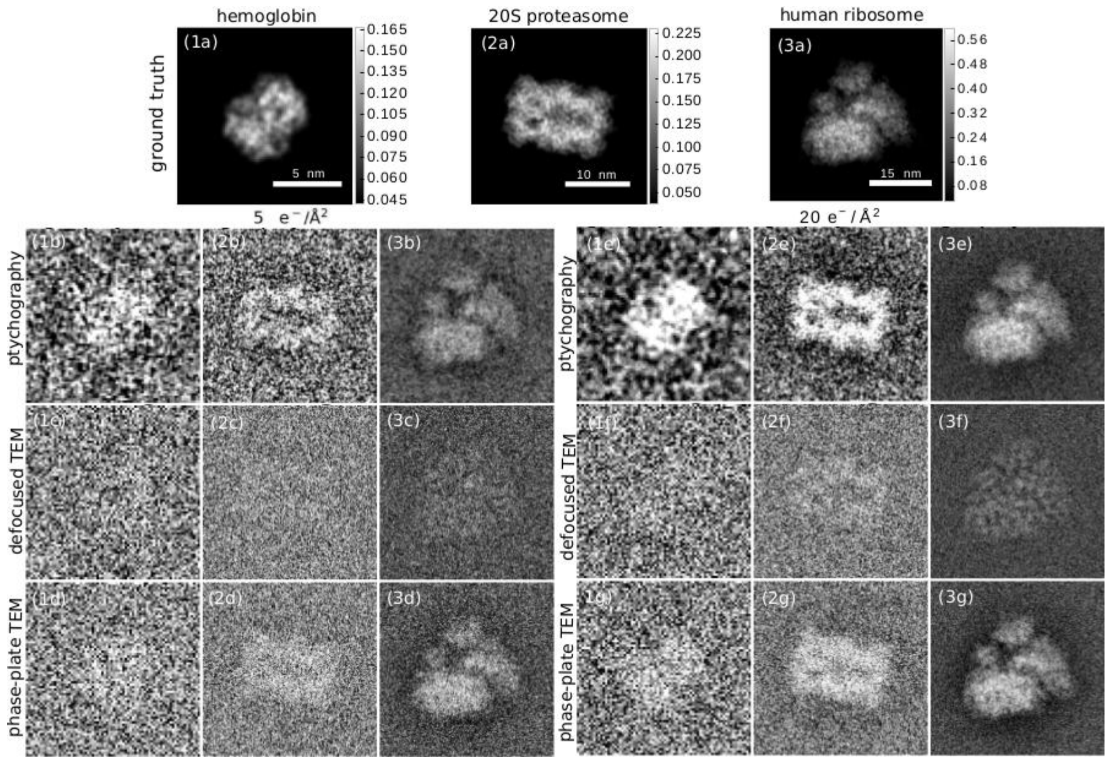

Figure 2.5: Cryo-electron ptychography reconstructions from simulated data and simulated cryo-EM images for different doses and 3 macromolecules with growing molecular weights in columns 1-3. Row a): Phase of the transmission function, the ground truth for the ptychography reconstructions. The scale bar next to the figures is in rad. Rows b) and e): ptychography reconstruction at doses of $5\,e^{-}/\mathring{A}^{2}$ and $20\,e^{-}/\mathring{A}^{2}$. Rows c) and f): Simulated cryo-EM image with a defocus of $1.6\,\mu\mathrm{m}$ at a dose of $5\,e^{-}/\mathring{A}^{2}$ and $20\,e^{-}/\mathring{A}^{2}$. Rows d) and g): Simulated cryo-EM image with a Zernike phase plate and a defocus of $50\,\mathrm{nm}$ at doses of $5\,e^{-}/\mathring{A}^{2}$ and $20\,e^{-}/\mathring{A}^{2}$. Column (1) hemoglobin, column (2) 20S proteasome, column (3) human ribosome (from Pelz *et al.* [96])

We choose exemplary doses of $5\,e^-/\mathring{A}^2$ as the typical threshold where the highest resolution details are destroyed [130] and $20\,e^-/\mathring{A}^2$ as a typical dose at which experiments are performed. We have reversed the contrast in the cryo-EM images to simplify the visual comparison with the ptychography reconstructions. To quantitatively assess the image quality, we have computed the 2D Fourier Ring Correlation (FRC) [131] with the ground truth for both the ptychographic reconstruction and simulated cryo-EM images of the macromolecules, as shown in Fig. 2.6. The ground truth images are depicted in appendix 6.5.

As ground truth for the images we use the electron counts in a noiseless, aberration-free phase-plate image. Using the 1-bit criterion as a resolution threshold [131], the achieved resolutions at $5\,e^-/\mathring{A}^2$ and $20\,e^-/\mathring{A}^2$, respectively, are 12 Å and 8.9 Å for hemoglobin; 10.9 Å and 9.1 Å for 20S proteasome; and 10.3 Å and 5.4 Å for human ribosome. In the case 20S proteasome, these values are identical to the FRC threshold for the phase plate image; for hemoglobin and human ribosome, the phase plate image yields a slightly better resolution of 8.7 Å and 5.1 Å respectively at a dose of $20\,e^-/\mathring{A}^2$ and 10 Å at a dose of $5\,e^-/\mathring{A}^2$. As the FRC is insensitive to very small and very large values of SNR, we also show the spatial-frequency resolved SNR in Fig. 2.6 d) - f). We define the SNR as

$$SNR(q) = 10 \cdot \log_{10}\left(\frac{|\mathcal{F}\left[T(\mathbf{r})\right]|^2}{|\mathcal{F}\left[T(\mathbf{r})\right] - \mathcal{F}\left[T_{model}(\mathbf{r})\right]|^2}\right)\text{dB}. \tag{2.34}$$

The SNR of the ptychographic reconstruction is significantly lower than the SNR of the phase-plate image for all three particles at spatial frequencies below $0.1\,\mathring{A}^{-1}$. It does however scale better to high spatial frequencies, and does not drop below -15 dB for all particles and all resolution up to nearly $0.5\,\mathring{A}^{-1}$, where the SNR is close to two orders of magnitude better than the phase-plate image SNR. This helps ptychography perform better when multiple reconstructions are averaged, because a positive single-digit SNR can be reached with fewer particles.

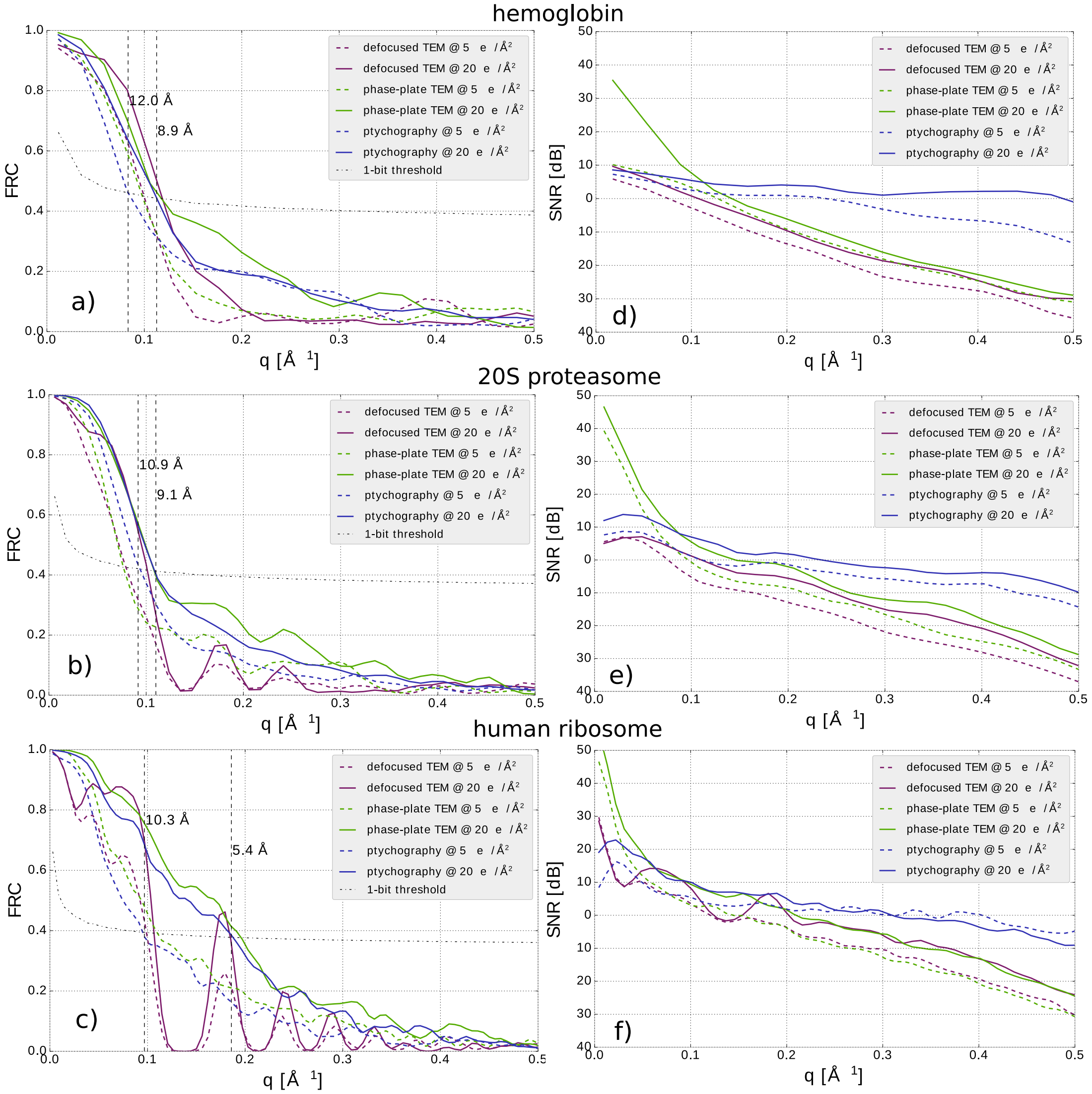

Figure 2.6: FRC a) - c) and SNR d) - f) as a function of spatial frequency for the cryo-electron ptychography reconstructions and simulated cryo-EM images in Fig. 2.5 (from Pelz *et al.* [96]).

2.6.2 Effect of averaging

In single-particle cryo-EM, a three-dimensional reconstruction can be obtained by collecting a large ensemble of 2D images, before orienting and averaging them in three dimensions, such that a satisfactory SNR is achieved [16, 132]. A similar 3D reconstruction from ptychographic data was not prioritized for this thesis, and a future full integration of ptychographic reconstruction with 3D reconstruction is certainly a challenging problem. A straightforward approach would be to use the reconstructed 2D phase images as an input to existing 3D reconstruction algorithms [132, 133], as is done routinely in ptychographic X-ray tomography [134]; however, it is likely that a dedicated algorithm which reconstructs the 3D structure directly from the diffraction patterns achieves the best results. Coarse orientation alignment for such an algorithm could be done in real space from 2D reconstructions shown here. We leave the evaluation of such approaches to future studies, and for now concentrate on the achievable 2D resolution when averaging a larger ensemble of particles.

To give a rough estimate how the resolution and SNR achieved by our algorithm scales with averaging over multiple datasets, we simulate 30 independent datasets with identically oriented particles, and average the reconstruction results. We found that the resolution corresponding to the diffraction limit as defined by the probe-forming aperture is achieved with roughly 40 averaged reconstructions as shown in Fig. 2.8. Superresolution beyond this point is in principle possible because ptychography transfers information up to double the half-convergence angle, but due to the low electron counts and the low contrast transfer for higher angles, more images are needed for further improvements. To limit the amount of necessary computation we use an average of 30 images, where a resolution of roughly 3 Å is reached, close to the resolution corresponding to the probe-forming aperture of 2.7 Å. Fig. 2.7 a)-f) show images of the averaged reconstructions of the three samples, at doses of $5\,e^-/\text{Å}^2$ and $20\,e^-/\text{Å}^2$ respectively. We also compare the FRC between respectively 30 averaged reconstructions of 60 independently Poisson-sampled ptychographic data sets, to give a resolution estimate. We use here the 1/2-bit resolution threshold discussed in [131], which gives a slightly more conservative estimate than the 0.143-criterion commonly used for the 3D Fourier Shell correlation in averaged reconstructions for 3D cryo-EM. With averaging, a resolution of 3.4 Å is achieved for hemoglobin, 3.1 Å for 20S proteasome and 2.9 Å for human ribosome, all at a dose of $20\,e^-/\text{Å}^2$. This shows that cryo-electron ptychography can recover atomic resolution information in 2D from only tens of averaged images, facilitated by the favorable scaling of the SNR with spatial frequency, as discussed above. It may therefore be possible to drastically reduce the number of particles that is required for a successful 3D reconstruction at atomic resolution. A rough estimate [135] suggests that the ribosome could be reconstructed to 3 Å resolution in 3D with less than 10 000 particles.

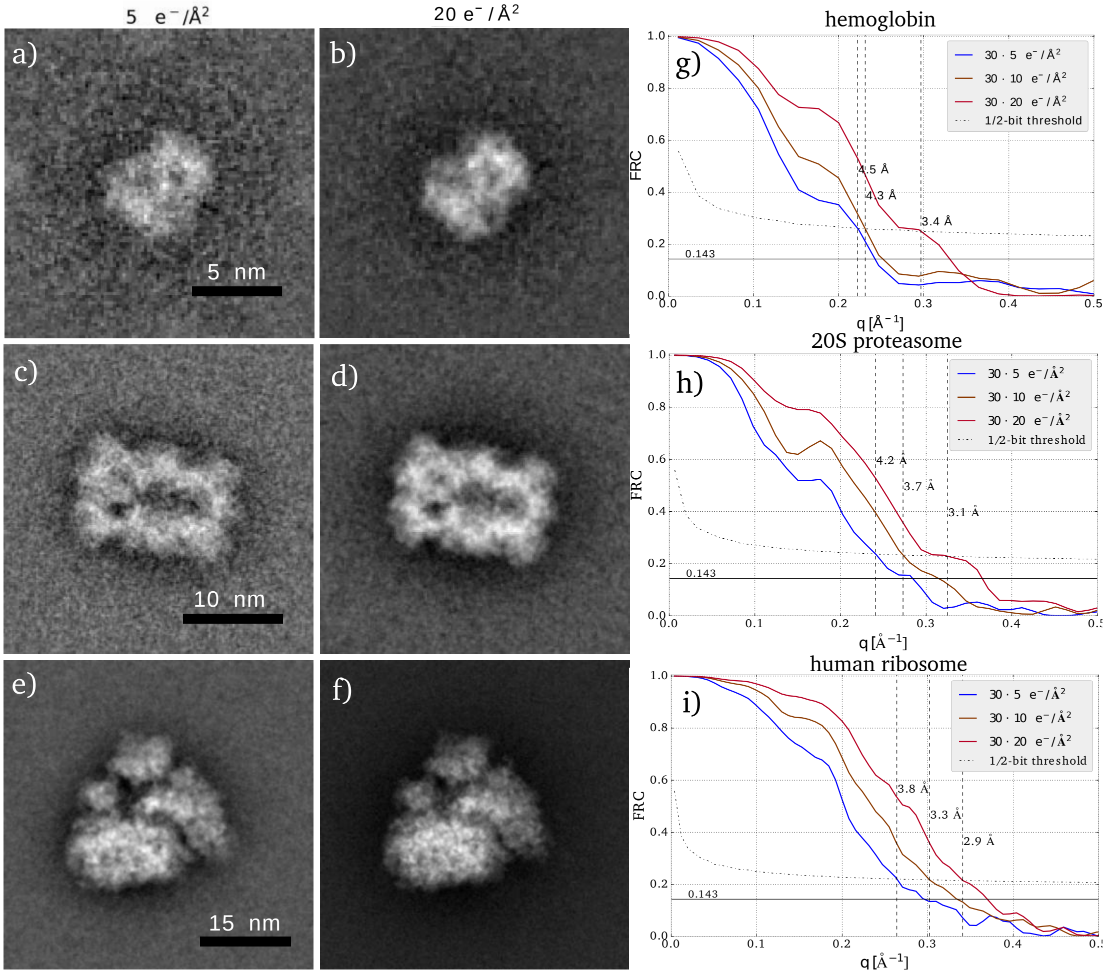

Figure 2.7: Average over 30 ptychographic reconstructions from independent data sets for a) hemoglobin with 5 $e^-/\text{Å}^2$, b) hemoglobin with 20 $e^-/\text{Å}^2$, c) proteasome 20S with 5 $e^-/\text{Å}^2$, d) proteasome 20S with 20 $e^-/\text{Å}^2$, e) human ribosome with 5 $e^-/\text{Å}^2$, f) human ribosome with 20 $e^-/\text{Å}^2$. FRC of averaged reconstructions from independent data sets for g) hemoglobin, h) proteasome 20S i) human ribosome. (From Pelz *et al.* [96])

Fig. 2.8 shows how the FRC scales with the number of averaged reconstructions, showing that also resolution beyond 3 Å are possible if enough particles are averaged. This is of course only possible if the sample fulfills the thickness requirements of ptychography, as explained in section 3.1.2.

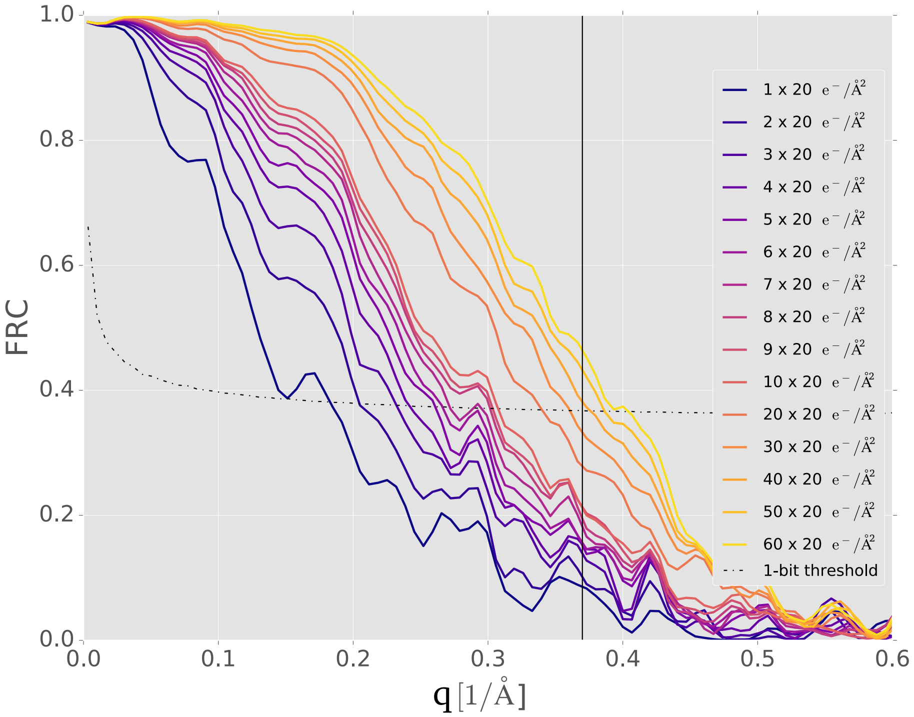

Figure 2.8: Scaling of the FRC between the ground truth and the averaged reconstructions with the number of averaged reconstructions for human ribosome at $20\,e^{-}/\text{Å}^{2}$. The vertical line is the wave-vector where the probe-forming aperture ends (from Pelz *et al.* [96]).

2.7 *scikit-pr*: a GPU-accelerated neural network-based implementation of Bayesian phase-retrieval

The algorithms presented above are highly parallelizable, because many operations are element-wise and fast parallel implementations of the Fourier transform exist. The use of gradient-based optimization schemes makes them amenable to be implemented in highly-optimized machine learning frameworks such as *pytorch* [136] or *Tensorflow* [137]. We chose to implement the algorithms in *pytorch* because of its numpy-like interface and because of its imperative control flow. At the time the project was initiated, the *Tensorflow* library only supported an interface based on computational graphs, which makes the code hard to digest for the normal python user, while *pytorch* offered an imperative programming style used in many programming languages. We therefore extended the *pytorch* framework to be able to specify networks with complex variables. A computational graph is generated by creating a `Variable`, which holds a `data` tensor and a `gradient` tensor. All operations on the Variable are recorded by an internal tape system, such that the gradient of any computation with respect to all `Variables` used in that computation can be computed by simply calling the function `backward()` on the `Variable`. The following code listing provides a simple example of the ease of gradient computation in pytorch.

```python
import torch as th
import numpy as np

x_array = np.array([5.])
y_array = np.array([3.])

x = th.autograd.Variable(th.from_numpy(x_array), requires_grad=True)
y = th.autograd.Variable(th.from_numpy(y_array), requires_grad=True)

z = 5*x+3*y**2

z.backward()

print(x.grad)
print(y.grad)

#Output:
#
#Variable containing:
#5
#[torch.DoubleTensor of size 1]
#
#Variable containing:
#18
#[torch.DoubleTensor of size 1]
```

In this way, complex computational graphs can be constructed just by calling differentiable functions on a `Variable`. Fig. 2.9 shows the computational graph for the ptychographic phase retrieval algorithm outlined in section 2.3. We have built a framework around this neural network-based modeling of experiments, so that the forward model, the loss function, and the optimizer can be swapped in a plug-and-play fashion. This means that for the implementation of a new experimental setup, only the neural network module must be swapped out.

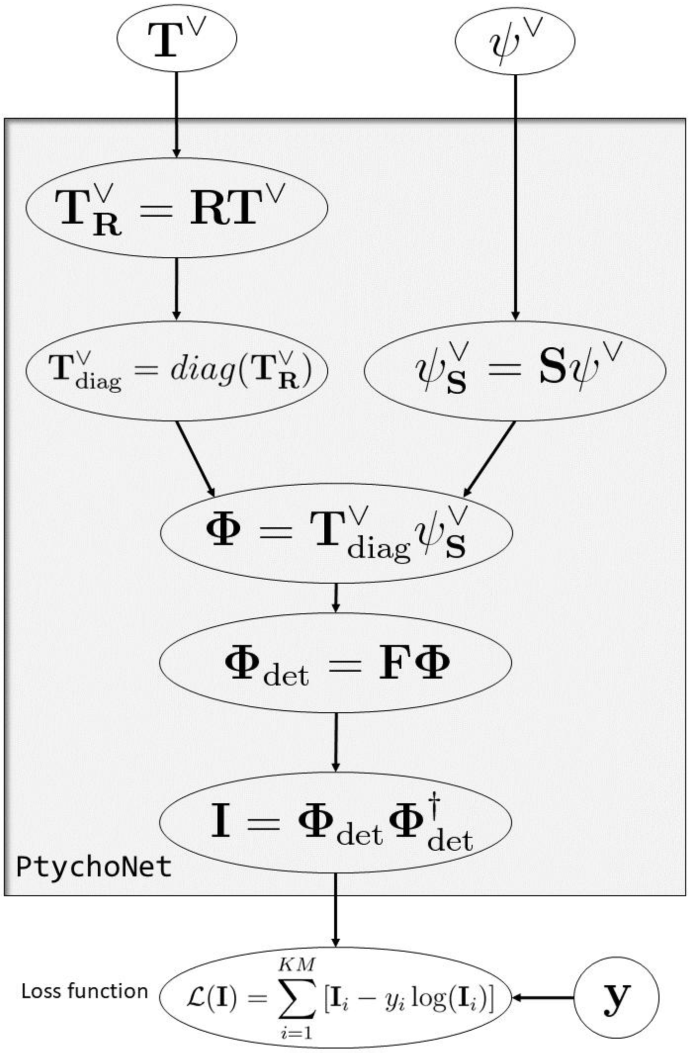

Figure 2.9: Schematic diagram of the computational graph for ptychographic phase retrieval. All nodes but the last node in the computational graph can be encapsulated into a neural network module we call `PtychoNet`. The loss function operates on the output tensor of the network, i.e. the model intensities $\mathbf{I}$, and the measured intensities $\mathbf{y}$. Different loss function depending on the measurement statistic can be adapted in a plug-and-play style, the rest of the network stays the same.

The following code listing shows an example of the configuration of a ptychographic reconstruction with *scikit-pr*:

```
import skpr.core.ptycho as pty
import skpr.nn as n
from skpr.core.parameters import *
from skpr.inout.h5rw import h5read
from skpr.nn import modules as M
from skpr.util import *

#Load the data
f1 = '/path/to/data.h5'
f = h5read(f1)
pr = f['probe']

#Load default parameters dictionary
p = get_ptycho_default_parameters()

#Specify the forward model
p.model = pty.models.PtychoNet

#Specify probe parameters
p.probe.initial = th.from_numpy(pr[np.newaxis, ...].astype(np.complex64))
p.probe.amplitude_constraint = None
#Specify at which iteration to start updating the probe
p.probe.update_start = 0
#Specify at which iteration to start centering the probe
p.probe.centering_active = lambda epoch: True if epoch > 1 else False
#Specify support radius of the probe in real and fourier space
p.probe.support_radius = None
p.probe.support_radius_fourier = None
#Specify a solution if this is from simulated data
p.probe.solution = None
#scale probe intensity to maximum diffraction data intensity
p.probe.scale_intensity_to_data = True
#use a mask on the probe gradients?
p.probe.gradient_mask = None
#is an amplitude constraint available for the probe?
p.probe.amplitude_constraint = None
#at which epochs should the probe be centered?
p.probe.centering_active = lambda epoch: True if epoch < -1 else False
#at which epochs should we include subpixel shifts?
p.probe.subpixel_precision_active = lambda epoch: True if epoch > 0 else False
# at which epochs should we optimize probe positions? - experimental
p.probe.subpixel_optimization_active = lambda epoch: True if epoch > 100 else False
#should we fix dead pixels in the bright field?
p.probe.fix_dead_probe_pixels = False

#specify the loss function depending on the measurement characteristics
p.loss.function = M.PoissonLikelihood

#specify a prior for the object
p.loss.object_prior = M.BM3DPrior
#noise parameter for the prior
p.loss.object_prior_parameters.sigma = 5

#specify the input data
p.ptycho.pos = th.from_numpy(f['pos']).cuda()
p.valid_mask = f['mask']
p.y = d = f['data']

#specify the optimization algorithm for probe, object, and object prior
p.optimizer.probe.type = th.optim.SGD
p.optimizer.probe.parameters.lr = 20e-2
p.optimizer.probe.parameters.momentum = 0.9
p.optimizer.probe.parameters.nesterov = True

p.optimizer.object.type = th.optim.SGD
p.optimizer.object.parameters.lr = 10e-2
```

```
p.optimizer.object.parameters.momentum = 0.7
p.optimizer.object.parameters.nesterov = True

p.optimizer.object_prior.type = th.optim.SGD
p.optimizer.object_prior.parameters.lr = 0.5

#specify if gradient should be calculated again after probe/object update
#or used for both updates
p.optimizer.optimize_probe_and_object_jointly = lambda epoch: False

#number of batches for minibatching the data
p.optimizer.n_batches = 250
#how the batches should be selected, 'random' or
#'clustering' of the positions
p.optimizer.batch_selection = 'random'

#logging specifications
p.logging.level = INFO
p.logging.log_reconstruction_parameters = False
p.logging.log_object_progress = True
p.logging.log_probe_progress = True
p.logging.log_error_progress = True
p.logging.print_summary = True
p.logging.print_report = True

#number of optimization epochs
p.epochs = 100

#hand the parameters to an engine and optimize
eng = pty.StochasticPtychoEngine(p)
eng.fit()
```

We note that the forward model

`p.model = pty.models.PtychoNet,`

the loss function

`p.loss.function = M.PoissonLikelihood`

and the optimization algorithm (in this case stochastic gradient descent (SGD))

`p.optimizer.probe.type = th.optim.SGD`

can be swapped with a single line of code, thereby making it easy to implement new experimental designs and test out new optimization algorithms. *scikit-pr* is available as open source with an MIT-license under `https://github.com/PhilippPelz/scikit-pr-open`. Currently `PtychoNet` and its dependencies are not released as open source, because Phasefocus Ltd. has a suit of patents regarding iterative ptychography and is prosecuting the publication of open source code.

3 Low-dose electron ptychography experiments

In this chapter we go over all practical considerations when designing and performing a low-dose ptychography experiment, and then show two proof-of-concept experiments with different combinations of microscope and direct electron detector.

3.1 Practical considerations for low-dose electron ptychography experiments

3.1.1 Electron microscopy equipment and availability

To perform a proof-of-principle low-dose electron ptychography experiment successfully with more than a few hours time on the same sample, the following equipment is required: An electron microscope with

1. a Schottky field emission gun [138] or a cold field emission gun [138] for a sufficiently coherent electron beam
2. STEM equipment for fast scanning of the sample
3. a fast direct electron detector with $\mathrm{DQE}(0) \sim 1$, ideally with electron counting
4. synchronization of the STEM scanning coils with the direct detector
5. a cryo-capable microscope with ancillary equipment

The fifth requirement can be lifted if one is content with exchanging the sample every few hours and using a conventional cryo-transfer holder. This combination of equipment is very unusual, because STEM is generally only used in materials science and is usually not fitted in cryo-electron microscopes. The synchronization with the direct detector must usually be purchased as an add-on package, or is even disabled per software in some cases to prevent over-exposure of the sensitive back-thinned direct electron detectors usually found in cryo-electron microscopes.

After a thorough search we found only one microscope which fulfills all the requirements. It is located at Cornell university in the group of Prof. Kourkoutis.

Unfortunately, beam time at this instrument was not available.
We found however several instruments which fulfill four of the five requirements, and the experiments performed on these machines are be presented in the following sections.

3.1.2 Sample thickness limits for ptychography

The sample thickness limit for ptychography is discussed in the seminal paper by Rodenburg & Bates [13]. The argument goes as follows: the scattering vector in z direction q_z is restricted by elastic scattering to the Ewald sphere:

$$q_z = q - \sqrt{(q^2 - q_x^2 - q_y^2)}. \tag{3.1}$$

For small scattering angles $q_x \ll q$, this can be Taylor expanded around $-(q_x^2 + q_y^2)/q^2$ to yield

$$q_z \simeq \frac{\lambda}{2}(q_x^2 + q_y^2). \tag{3.2}$$

The maximum scattering angle determines the attainable resolution $q_{x,max} = 1/\Delta r$. For a truly 2D object, the 3D transform is independent of the frequency q_z and the measurement on the Ewald sphere is equivalent to measurement of the 2D diffraction intensities. An object of finite thickness t has speckles of size $1/t$ in longitudinal direction. If the Ewald sphere at the highest transverse frequencies still cuts through a speckle the is centered at $q_z = 0$, then the measurement can be treated just like a 2D Fourier transform. Different criteria can now be applied for the validity of the Ewald sphere departure. Rodenburg & Bates [13] used the criterion $q_z < 1/t$, while Chapman *et al.* [139] use a stricter criterion $q_z < 1/4t$. Rodenburg's criterion leads to a maximum allowable sample thickness of

$$t_{max} \simeq \frac{2(\Delta r)^2}{\lambda}, \tag{3.3}$$

while Chapman's criterion leads to a maximum thickness of

$$t_{max} \simeq \frac{(\Delta r)^2}{2\lambda}. \tag{3.4}$$

Tsai *et al.* [140] conclude after a numerical study, that Rodenburg's criterion can be relaxed even more and suggest a thickness limit $t_{max} \simeq \frac{5.2(\Delta r)^2}{\lambda}$. We stick here to Rodenburg's original formula. If, for the sake of a proof of principle experiment, if one aims for a resolution of 3 Å at an electron energy of 300 keV, the maximum allowable sample thickness is $t_{max} \simeq 91$ nm. While this is a quite a steep requirement for cryo-EM sample preparation, preparing a vitrified protein sample with this thickness is certainly within reach of current sample preparation methods. If one aims for higher resolution, two or more slices would need to be reconstructed in a multi-slice fashion [141, 142], or thinner samples would need to be prepared, adding more complication to the experiment. The relation between resolution and thickness limit is in line with the just recently implemented Ewald sphere corrections to achieve sub-3 Å resolution for conventional cryo-EM [143–145].

3.1.3 Sampling considerations for low-dose ptychography

The sampling requirements of ptychography were studied by Bunk *et al.* [146] and Edo *et al.* [147] and then more rigorously by da Silva & Menzel [148] and da Silva & Menzel [148]. As discussed in section 1.3.3.3, a ptychographic data set comprises a discretely-sampled phase-space convolution of the Wigner distributions of probe and object. The usual sampling in coherent diffractive imaging (CDI) is oversampling with respect to the underlying Nyquist detector sampling of the complex-valued wave. This means that the diffraction pattern has to be sampled at twice the periodicity of the wave amplitude incident upon the detector because twice as many intensity measurements are required to solve for the complex-valued wave function (real and imaginary numbers) arriving at the detector [149]. This gives the CDI sampling criterion

$$\Delta\theta \leq \frac{\lambda}{2D}, \tag{3.5}$$

where $\Delta\theta$ is the angular sampling of a detector pixel, and D is the spatial extent of the object, or the probe, whichever is smaller. Because ptychography oversamples phase space, the CDI sampling criterion can be significantly relaxed, and Batey *et al.* [150] and Edo *et al.* [147] show in experiments and simulations that the phase-space sampling criterion

$$\Delta\theta\Delta R \leq \frac{\lambda}{2} \tag{3.6}$$

must be fulfilled for successful reconstruction. Here, ΔR is the step size in real space. Batey *et al.* [150] define also the quantity

$$S = \frac{\lambda}{2\Delta\theta\Delta R} \geq 1 \tag{3.7}$$

to easily evaluate if the ptychographic sampling criterion is fulfilled. This means that poor sampling in real space, i.e. a large step size, can be compensated by dense sampling in detector space, i.e. using a detector with many pixels, and vice versa.

For ptychography at low doses this means that the detector can be binned up to a point where the ptychographic sampling criterion is still fulfilled, thus increasing the signal-to-noise ratio for each measurement. As we discuss in the detector section, this has the additional beneficiary effect of using the DQE of the detector in the most efficient way.

3.1.4 Ambiguities in ptychographic reconstructions

The result of a ptychographic reconstruction is only unique with respect to the autocorrelation of the exit waves $\psi_j(\mathbf{r}) = \psi(\mathbf{r} - \mathbf{r}_j)T(\mathbf{r})$. With any $\mathbf{r}_f, \mathbf{q}_f \in \mathbb{R}^2$ and $c_f \in \mathbb{C}$ we may construct alternative probes and objects,

$$\psi'(\mathbf{r}) = c_f e^{2\pi i \mathbf{q}_f \mathbf{r}} \psi(\mathbf{r} - \mathbf{r}_f) \qquad \text{and} T'(\mathbf{r}) = \frac{1}{c_f} e^{-2\pi i \mathbf{q}_f \mathbf{r}} T(\mathbf{r} - \mathbf{r}_f), \tag{3.8}$$

and note that these primed solutions are also compatible with the model

$$I_j(\mathbf{q}) = \left| \mathcal{F}_{\mathbf{r},\mathbf{q}} \left[\psi'(\mathbf{r} - \mathbf{r}_j) T'(\mathbf{r}) \right] \right|^2 . \tag{3.9}$$

The amplitude of the multiplicative scaling factor c_f can usually be fixed if the probe intensity is known, while the constant phase factor is an inherent ambiguity in every phase retrieval problem. Because of the multiplicative model of ptychography, another ambiguity arises dependent on the scan pattern [121]. If a solution to Eq. (3.9) has been found in form of a wave function $\psi_j(\mathbf{r})$ and a transmission function $T(\mathbf{r})$, let two new functions be $T''(\mathbf{r}) = f(\mathbf{r})T(\mathbf{r})$ and $\psi''(\mathbf{r}) = f(\mathbf{r})^{-1}\psi(\mathbf{r})$. It can be seen that $T''(\mathbf{r})$ and $\psi''(\mathbf{r})$ are also a solution of the problem iff

$$f(\mathbf{r}) = f(\mathbf{r} - \mathbf{r}_j) \forall \mathbf{r}_j. \tag{3.10}$$

This means that, when the real space sampling is not dense enough to represent a true convolution in discrete phase space, i.e., if the step size is larger than the diffraction-limited resolution, and the sample is scanned on a periodic lattice with step size s in pixels, s^2 additional degrees of freedom are introduced, which manifest itself as the so-called *raster grid pathology* [121, 151]. Since the typical scan in STEM is done on a periodic lattice, and the scanning coils suffer hysteresis when they are scanned arbitrarily, it is currently favorable to scan very densely to avoid these artifacts. However, as is discussed in the following chapter, the beam current together with available camera speeds do currently not allow to sample densely enough.

Some microscope manufacturers have already begun developing specialized scan hardware for ptychography, so it is only a matter of time until this problem is solved. Recently it was shown that the raster grid problem can be mitigated when the far-field intensity of the probe function is know [103], but this is not always practical in electron ptychography experiments, since a vacuum region needs to be present on the sample or the sample needs to be removed from the microscope column after a scan, which can change the illumination conditions depending on stability of the microscope.

3.1.5 Direct electron detectors for low-dose ptychography

There are two different families of direct electron detectors currently available. Monolithic active pixel sensor (MAPS) detectors have rather small pixels and are back-thinned so that the streak that an electron leaves on the pixels is confined to a small area. They are intrinsically integrating detectors, but if the frame rate is high enough and the electron flux per pixel is low enough, the electrons can be counted and localized after detection, in some cases even with sub-pixel precision. MAPS detectors were developed for real-space imaging applications, where a large number of pixels is important to achieve a large field of view. Because of the large number of pixels, the electron-counted unbinned frame rate of these detectors is usually below 100 Hz, which makes them suboptimal for ptychography. The other family of detectors are called hybrid pixel array detectors. Most of these detectors were initially developed for X-ray applications at synchrotrons. They feature a rather large pixel size, and the sensitive area is bump-bonded onto a readout chip. This decoupling of readout and detection gives them very low readout noise, and most of these detectors are intrinsically counting detectors. In table 3.1 we give an overview about the characteristics of most of the currently available direct electron detectors.

detector		f_{full} [kHz] / dyn. range	f_{max} [kHz] / binning	counting/windowing	DQE(0)
EMPAD	[129, 152]	1.1 / 1×10^6	1.1 / 1	no/no	0.94
Medipix3	[153]	1 / 24bit, 2 / 12bit	1 / 1, 2 / 1	yes/no	0.8
EIGER	[154, 155]	2 / 32bit, 6 / 12bit, 23 / 4bit	23 / 1	yes/yes	0.8
pnCCD	[128]	1 / [1bit @ >200 keV , 2bit @ < 200 keV]	4 / 4	no/yes	N.A.
DE16	[126, 156]	0.06 / 32bit	6 / 2	yes/yes	0.85
K2	[126, 156]	0.04 / 32bit	0.04 / 1	yes/yes	0.8
K2 IS	[126, 156]	0.4 / 32bit	1.6 / 4	no/yes	0.8

detector	DQE(Nyquist)	I_{max}	pixel size [μm]	pixels
EMPAD	N.A.	2.7 pA / pixel	150	128x128
Medipix3	0.3	N.A.	55	panels of 256x256, max 1536 x 1536
EIGER	0.1 (extrapolated)	N.A.	75	panels of 256x256, max 4150 x 4371
pnCCD	N.A.	N.A.	48	264 x 264
DE16	0.2	N.A.	6.5	4096 x 4096
K2	0.26	4.8×10^{-7} pA / pixel	5	3838 x 3710
K2 IS	0.26	4.8×10^{-7} pA / pixel	5	3838 x 3710

Table 3.1: Overview of currently available direct electron detectors, ordered by descending pixel size. f_{max} is the max. frame rate possible. f_{full} is the maximum full-field frame rate. DQE values are given for 200 keV energy. I_{max} is the maximum current per pixel for optimum performance @ 200keV.

Since the current in a focused electron beam can be several tens of pA, and a beam current of 10 pA in a 10 nm diameter beam deposits an electron flux of $\sim 2000\, e/\text{Å}^2\text{s}$ on the sample, detectors with high frame rates are desirable for low-dose ptychography, because it is difficult to tune down the current in the microscope enough to achieve the low doses needed for cryo-EM in a ptychography experiment. The fact that most cryo-microscopes are equipped with slow MAPS detectors makes a proof-of-principle experiment currently difficult.

3.1.6 Data preprocessing steps

As an electron microscope has more lenses than ideally needed for an electron ptychography experiment, the data can vary greatly from experiment to experiment, because the microscope is usually newly aligned each time. The largest source of error in the reconstructions is the shifting of the bright field disk during the scan as a consequence of imperfect alignment of the pivot points in the beam deflection system. Equally important is the determination of hot or dead pixels, as these can deteriorate reconstructions by a large amount. A pixel mask is routinely determined for every experiment. Fig. 3.1 shows the order in which the data and metadata are processed to form an input data set for the reconstruction algorithm. First, data, metadata, hot pixel mask and gap mask are loaded from disk. Then, if not already known, the rotation of the diffraction pattern due to the projection lenses in the microscope is determined, and also the per-column and per-row shifts of the bright field disk. From the metadata camera length, convergence angle, and defocus, an initial estimate of the probe wave function is generated. Then data are cropped to a square size from the center and binned, if the sampling criterion Eq. (3.6) allows it. Then, bright-field and dark-field STEM images are created from the dataset, by summing the respective intensities with a mask given by the convergence angle, and saved to get a first impression if everything is prepared correctly so far. Optionally, intensity from dead pixels can be interpolated if the counts in the neighboring pixels are not too low. The final data, masks, and positions are then saved to an hdf5 file as input for the reconstruction algorithm. An example of a metadata file is shown in appendix 6.2.

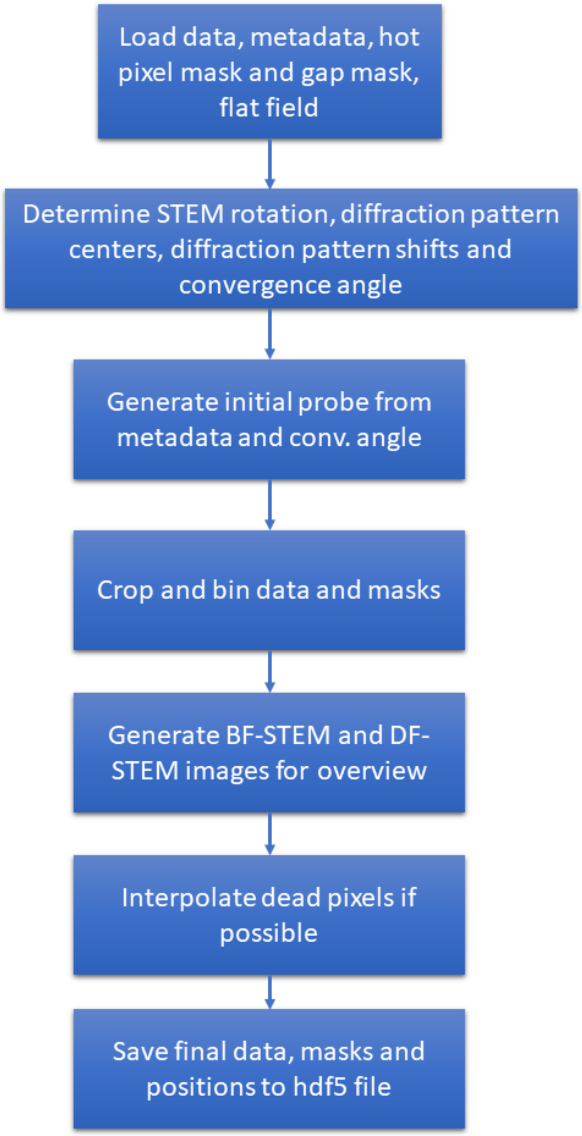

Figure 3.1: Flow graph of the data preprocessing routine. At the Tecnai F20 microscope in Hamburg, the metadata are saved in a separate json file for every scan

3.2 Discussion of previous published experiments in electron ptychography

The electron dose used for successful reconstruction used in electron ptychography experiments has exceeded $1 \times 10^3\, e^-/\text{Å}^2$ so far, limiting the usability of ptychography to radiation-hard specimens. Table 3.2 lists recently published electron ptychography experiments and the used average electron doses. The lowest dose was reported in Jiang *et al.* [162], which performed a dose series with electron doses down to $250\, e^-/\text{Å}^2$ on a two-dimensional molybdenum disulfide sample. At this dose, however, the atomic positions cannot be recovered anymore from a reconstruction with the ePIE algorithm. A reasonable reconstruction was only possible with $1 \times 10^3\, e^-/\text{Å}^2$. We note that most samples reconstructed with electron ptychography so far have been crystalline samples, where all the intensity is scattered only into few reciprocal lattice vectors, and therefore the achieved resolution is not comparable with the reconstruction of an amorphous sample such as a protein.

Reference	resolution	dose
Putkunz *et al.* [157]	$\sim$1 Å	9.2×10^6
Wang *et al.* [158]	$\sim$2 Å	2.1×10^6
Gao *et al.* [142]	3.4 Å	not specified
D'Alfonso *et al.* [159]	$\sim$1.5 Å	1.77×10^4
Yang *et al.* [160]	atomic	1.3×10^4
Humphry, Kraus & Hurst [161]	$\sim$2.3 Å	3.33×10^3
Jiang *et al.* [162]	$\sim$2 Å	1×10^3

Table 3.2: List of previously published electron ptychography experiments, achieved resolution, if stated, and used electron dose.

The only publications on amorphous samples are Yang *et al.* [160], where only heavy atoms in carbon nanotube conjugates could be resolved at a dose of $1 \times 10^3\, e^-/\text{Å}^2$. Gao *et al.* [142] resolve the 3.4 Å spacing of carbon nanotubes but do not report the used dose.

The following two sections describe therefore experiments at unprecedented low-dose conditions and with amorphous samples.

3.3 Demonstration with carbon black flakes on a Titan Krios microscope

A major obstacle to perform the above mentioned cryo electron ptychography experiment is the scarcity of suitable equipment and the limited access to equipment. A benchmark experiment was therefore performed at the Ramaciotti Centre for Cryo-electron Microscopy at Monash University with the microscopist Georg Ramm. It houses a Titan Krios Microscope with an autoloader system for 12 microscope grids, cryo-box, Gatan K2 Summit and FEI Falcon II direct detectors and a STEM system. The Titan Krios is a microscope with three condenser lenses, such that the probe convergence angle is not coupled to the size of the condenser aperture. The FEI Falcon II detector was disabled via software as soon as the microscope was set to STEM mode, so that it could not be used for ptychography experiments. The K2 detector is not synchronized with the STEM system, so that it was necessary to start the movie mode of the camera first and then start a STEM scan and select only data sets where the camera was synchronized with the STEM motion. This was the only way to perform ptychography experiments with a direct detector on the Titan Krios.

The K2 summit has a maximum frame rate of 40Hz, 3838×3710 pixels and a pixel size of $5\,\mu$m. At the time of the experiment, it was the detector with the best detective quantum efficiency on the market. A downside of this detector is the low frame-rate, which cannot be increased by binning. We were not allowed to change condenser apertures for the experiment, so the only tunable parameter to control the dose, after setting gun lens and spot size to the highest values to spread the beam as large as possible before the condenser aperture, was the step size of the scan.

Due to the low frame-rate we did not reach the desired dose of $20\,e^-/\mathring{A}^2$. Even when inserting the smallest condenser aperture of $50\,\mu$m size, and using the microscope settings with highest coherence and lowest electron dose (spot size 11, gun lens 9), we could only reach a dose of $40\,e^-/\mathring{A}^2$ by slightly misaligning the gun, such that the intensity maximum is off-center on the condenser aperture.

The defocus was set to 800 nm to achieve a probe size of roughly 10 nm with a convergence semi-angle of 6 mrad. This corresponds to a diffraction-limited half-period resolution of 1.6 Å. The step size was 3 nm to achieve a probe overlap of 66 %. With these parameters a ptychographic oversampling parameter of $S = 13.9$ is achieved. We performed a dose series to illustrate the impact of electron dose on image quality. The camera length was set to 1.22 m, such that the bright-field disk almost filled the whole detector.

A set of sample diffraction patterns at doses of $40\,e^-/\mathring{A}^2$, $100\,e^-/\mathring{A}^2$ and $500\,e^-/\mathring{A}^2$ is shown in Fig. 3.2 b) - d). In Fig. 3.2 d), the first diffraction orders of the carbon planes become visible at the edges of the screen. The diffraction patterns were cropped to a size of 512 × 512 pixels after binning. The carbon planes in the sample greatly alleviated the determination of the defocus for the experiment, as the beam size on the specimen and therefore the defocus can be read off the bright field disc by counting the number of lattice fringes in the disk. Fig. 3.2 a) - c) show the phase of the reconstructed transmission function for the three different doses. For the reconstruction we used Algorithm 2 with parameters $Iter_{Max} = 40$, $\square =$ BM3D, $n_{batch} = 32$, $\rho_{\psi^\vee} = 0.9$, $\rho_{\mathrm{T}^\vee} = 0.6$, learning rates

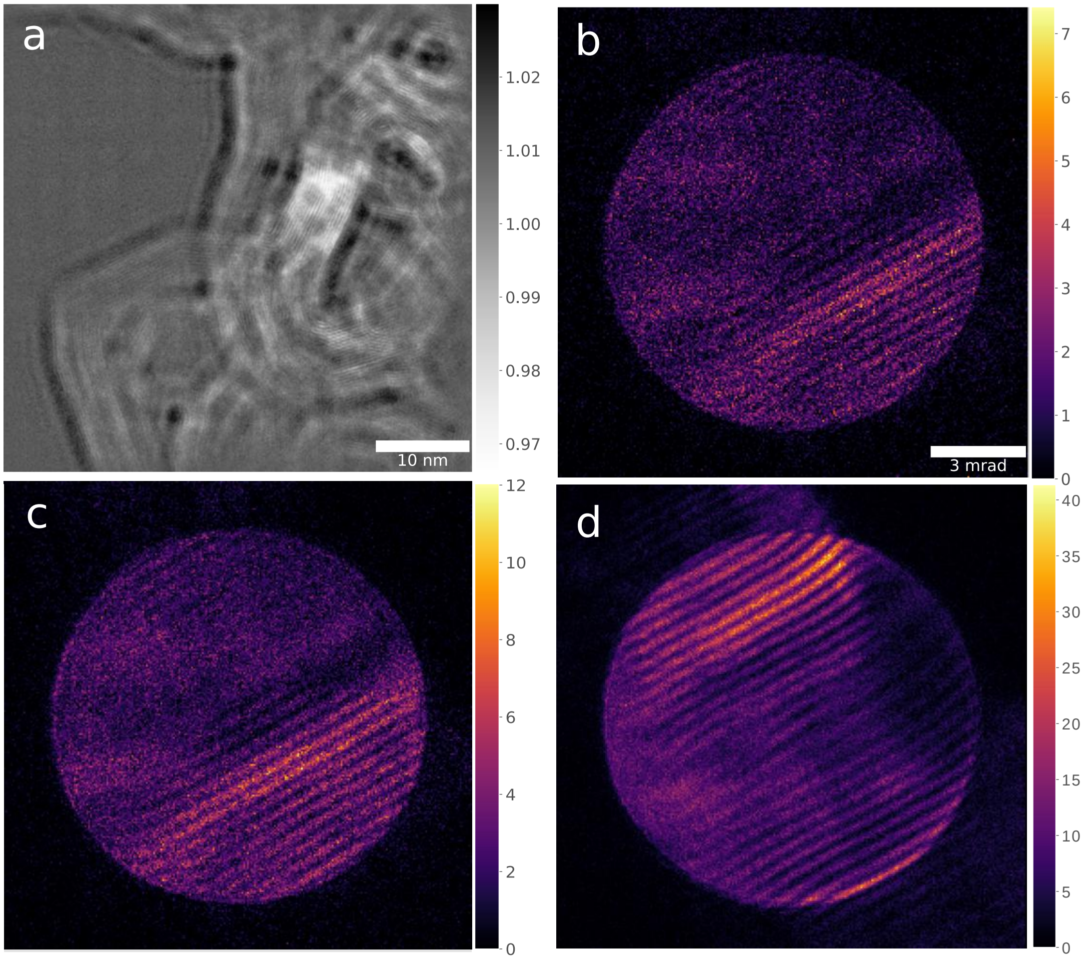

Figure 3.2: a) Example reconstructed amplitude profile of the carbon black sample at . b)-d) Example intensity measurements of the datasets with a total dose of $40\,e^-/\mathring{A}^2$, $100\,e^-/\mathring{A}^2$ and $500\,e^-/\mathring{A}^2$.

$\gamma_{\psi^\vee} = 10^{-3}, \gamma_{\mathbf{T}^\vee} = 10^{-3}$.

After the first successful reconstruction the microscopist at the Ramaciotti Centre for Cryo-electron Microscopy contacted the microscope manufacturer FEI to enable the Falcon detector for STEM imaging, as it would be automatically integrated in the STEM system of the microscope software. After a few months, FEI released the software lock so that a first cryo-experiment was performed on GroEL particles in April 2017. It was then realized that the counting mode of the Falcon II camera could not be activated when it is operated in STEM mode. The integrating mode of the Falcon II has a much worse DQE, therefore the experiments were discontinued. In the following months I was only granted single days on the microscope and was attending the experiments remotely.

A general problem in cryo-ptychography experiments is that the only available online analysis tool while performing the experiment is the high-angle annular dark field signal. This signal is relatively weak for biological macromolecules, such that navigating the specimen and choosing the area to image can can either be achieved by changing between TEM and STEM mode, which changes the whole lens system of the microscope and makes it difficult to image a previously selected area, or by defocusing the beam very strongly, so that the particles become visible in the ronchigram.

Another difficulty is the exact determination of the defocus for a good initial estimate for the reconstruction algorithm, and to roughly know that the sampling criteria are fulfilled. A usual trick from cryo-tomography is to use gold-nanoparticles (AuNPs) with a narrow size distribution. We also tried to include carbon black flakes into the sample solution, so that the typical fringes shown in Fig. 3.2 could be used for defocus determination. The carbon black flakes look very similar to ice crystals at low magnification and are therefore not optimal, because an area with both carbon black flakes and protein sample is hard to find. This of course depends on the time one invests in sample preparation, and could easily be improved in future experiments. Although the experimental time on the microscope is limited, the refinements of the experimental procedure are still ongoing.

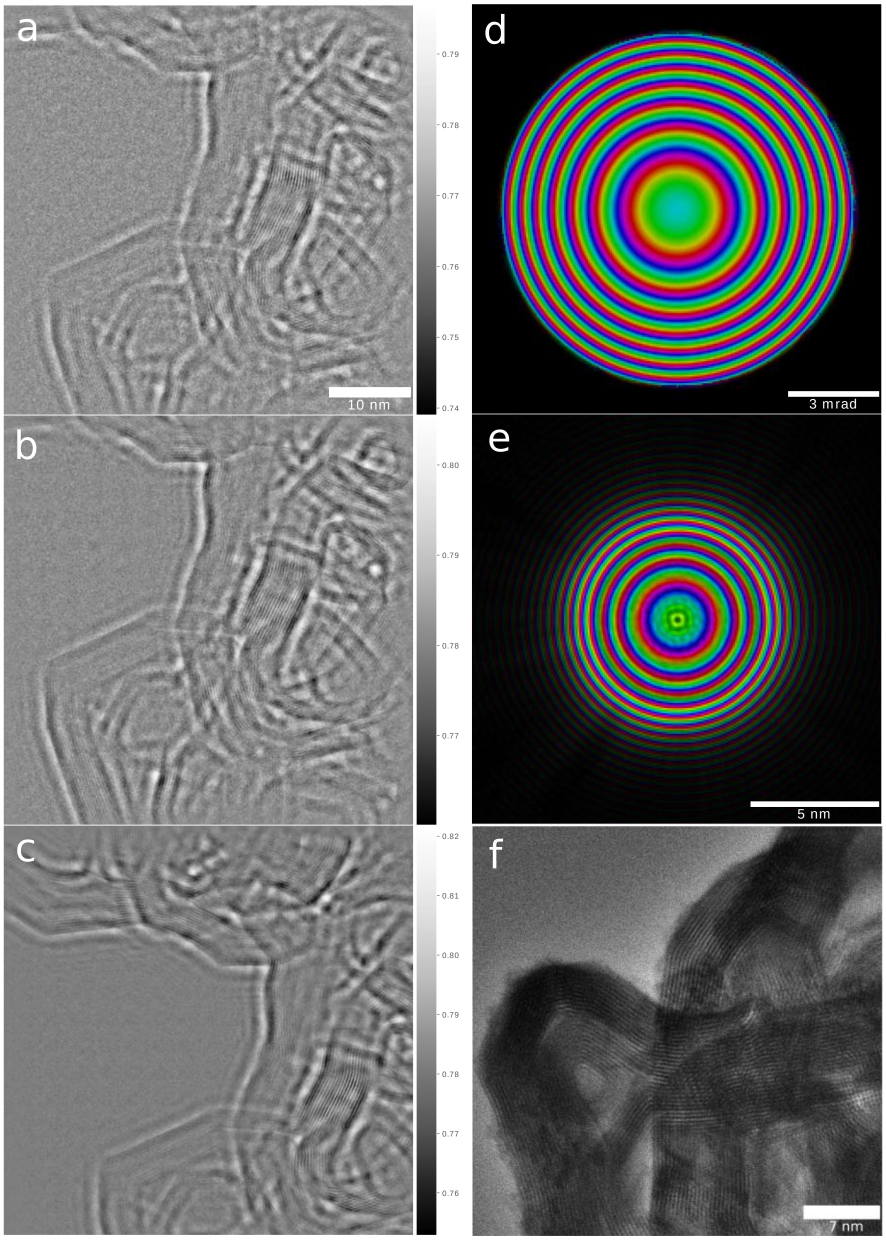

Figure 3.3: Comparison of ptychography reconstructions at different doses, and comparison with Volta phase plate. a) Reconstruction at $50\,e^{-}/\text{Å}^2$, b) Reconstruction at $200\,e^{-}/\text{Å}^2$, c) Reconstruction at $500\,e^{-}/\text{Å}^2$, d) Reconstructed probe in the condenser aperture plane, e) Reconstructed probe in the sample plane, f) Image taken with a Volta phase-plate in the back focal plane at approximately zero defocus at $100\,e^{-}/\text{Å}^2$.

3.4 Demonstration with apo-ferritin proteins at room temperature at a Tecnai F20 microscope

In 2014 a collaboration between the microscope manufacturer FEI and the Max Planck Institute for Structure and Dynamics of Matter was initiated. Part of the collaboration agreement was the delivery of a Tecnai F20 microscope with a Schottky field emitter to the Max Planck Institute in Hamburg. Due to delays in the acquisition and installation process, the microscope was available for experiments in late 2017.
Concurrently with the negotiations, a prototype of a water-cooled Medipix 3 detector was developed by the postdoc Fabian Westermeyer in collaboration with the DESY detector group. It was installed on the microscope in Jan. 2018, so that the first benchmark experiments could be performed in February 2018. After a first set of experiments in February and March 2018, the detector was unavailable due to a cooling failure. A second set of experiments was performed in June 2018 with unfixed apo-ferritin molecules from horse spleen on ultra thin carbon film (3 nm thickness). The microscope was operated and aligned by the postdoc Robert Bücker and the apo-ferritin sample was prepared by Dennis Eggert.

Because the F20 microscope has only two condenser lenses, the convergence angle can only be set by choosing and appropriate size of the condenser aperture. An aperture of $70\,\mu$m diameter was chosen, which results in a half-convergence angle of 7.4 mrad and a diffraction-limited resolution of 1.69 Å for an electron energy of 200 keV. We choose a defocus of 800 nm, resulting in a probe diameter of 11.5 nm, and a scan step size of 3.4 nm. This corresponds to a probe overlap of 70.4 %. This results in an oversampling parameter of $S = 6.4$.

The beam current was chosen as 2.8 pA and the exposure time of the camera to 2 ms, such that a scan of 64×64 positions completed in 8.2 s. The total accumulated dose on the sample was $30\,e^-/\text{Å}^2$.
The reconstruction is shown in Fig. 3.4. One can clearly make out the ferritin particles in the phase image, but the background from the thin carbon substrate is quite strong. Also because the experiment was performed at room temperature, the particles are expected to have undergone significant radiation damage, although the shape of some particles clearly resembles the known structure, for which we show a phase map in Fig. 3.4 c). It can also be seen that the reconstructed phase shift of 0.08 rad is only half of the expected maximum phase shift of 0.16 rad. This can either come from mass lose due to radiation damage, or the inhomogeneous background phase shift of the carbon substrate. For a de-

tailed assessment of the improvement in SNR over conventional methods, an experiment under cryogenic conditions must be performed. For the reconstruction we used Algorithm 2 with parameters $\mathit{Iter}_{\mathit{Max}} = 50$, $\square =$ BM3D, $n_{batch} = 64$, $\rho_{\psi^\vee} = 0.9$, $\rho_{\mathbf{T}^\vee} = 0.6$, learning rates $\gamma_{\psi^\vee} = 10^{-3}$, $\gamma_{\mathbf{T}^\vee} = 10^{-3}$.

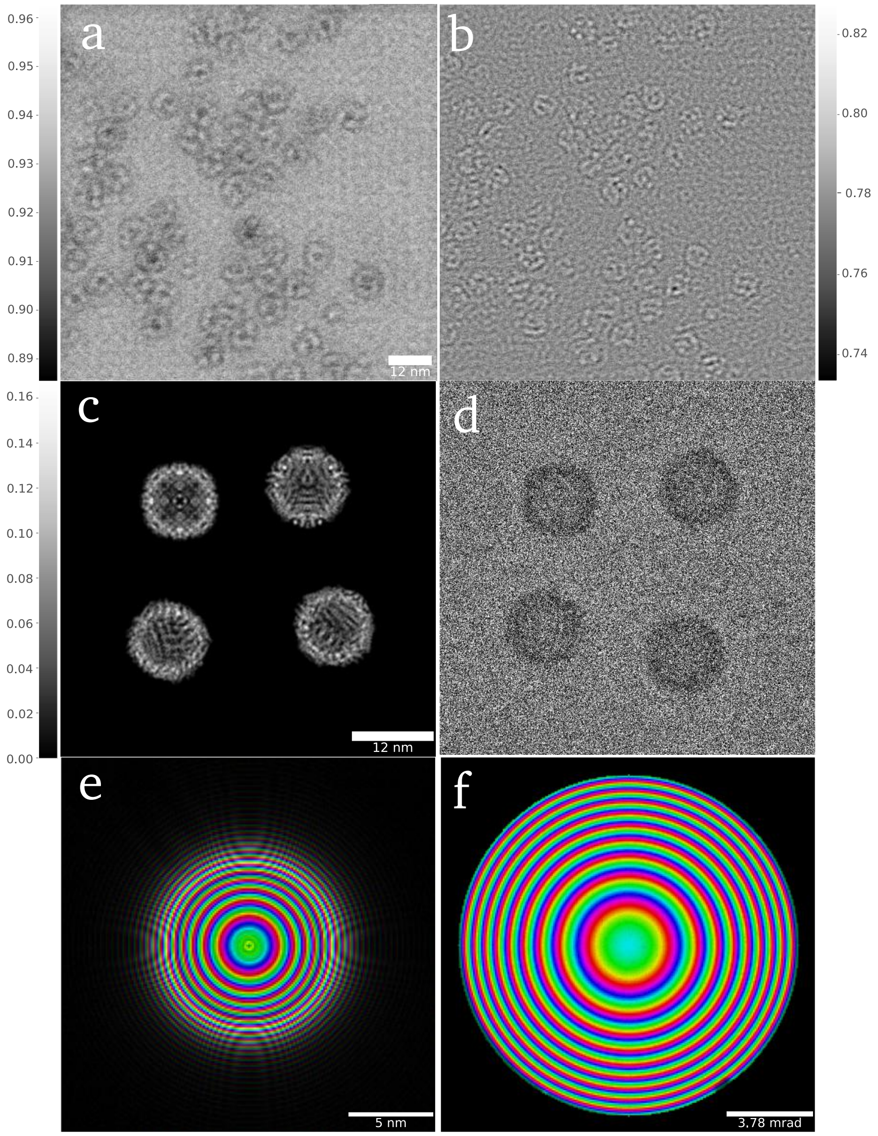

Figure 3.4: Ptychographic reconstruction of apo-ferritin molecules on ultra-thin carbon at a dose of $30\,e^-/\text{Å}^2$. a) Amplitude of the reconstructed transmission function, b) phase of the reconstructed transmission function. c) phase maps of apo-ferritin molecules simulated for $200\,\mathrm{keV}$ for visual comparison with the reconstruction. d) simulated Volta-phase plate cryo-EM image at a dose of $30\,e^-/\text{Å}^2$. e) Reconstructed probe at the sample plane. Slight aliasing can be seen at the edges of the probe due to binning to fit the data set into GPU memory. This should be avoided in future experiments to achieve an optimal reconstruction. f) Reconstructed probe at the aperture plane. In the lower right corner of the aperture on can see some dirt protrude towards the center, obstructing the intensity.

3.5 Conclusion and remarks

We have discussed the experimental implications and difficulties when planning and performing a low-dose ptychography experiment with currently available equipment. We show two proof-of-principle experiments and demonstrate that ptychographic phase contrast imaging is possible at the low doses required for cryo-EM. Due to the lack of experimental access to the equipment we could not show a reconstruction under cryo conditions yet, but with a sample of sufficient quality we do not see any obstacles to perform cryo-electron ptychography experiments in the near future.

4 Towards optimal experimental design for phase retrieval in the TEM

In this chapter we review several papers that hint at the advantages of using structured illumination in phase retrieval experiments. We discuss how structured illumination can be realized in the TEM and design and test nano-structured phase masks which can be inserted in the condenser aperture to produce a beam with strongly varying local phase structure.

4.1 The case for structured illumination electron ptychography

It is well-known that the phase profile of the ptychographic probe can heavily influence the reconstruction quality. The use of a 'phase-diverse' beam for ptychography was first realized in 2011 for visible light [163], where it was used to achieve super-resolution of up to 4 times the diffraction limit imposed by the detector cut-off. It was subsequently used to achieve three-dimensional imaging by reconstructing multiple slices of the specimen [141, 164]. In the framework of WDD it was shown that a probe with multiple vortices produces higher quality reconstructions and suppresses noise, because its large extent in phase space stabilizes the numerical deconvolution procedure [111]. Subsequently, diffusers were also used in X-ray ptychography to enhance the reconstruction quality [165–167] and it was suggested that partial coherence can be analyzed in real time by characterizing the intensity histogram of a diffuser beam diffraction experiment [167]. Marchesini, Tu & Wu [97] provided another argument similar to [111] for diffuser beams: when the illuminated pixels are connected with the measurements in a connection graph, a beam that is large in real and Fourier space provides a denser graph and therefore more constraints for phase retrieval. Recently, randomized zone plates have been developed for the soft X-ray regime that provide μm-sized beam with speckled phase structure to better distribute the intensity over the detector and improve reconstruction quality [168].

From these reports alone it seems highly beneficial to use a structured beam in low-dose electron ptychography experiments. We therefore analyze the impact of structured illumination in the reconstruction quality of low-dose ptychography experiments below. We numerically test three different probes, depicted in

Fig. 4.1, and their influence on the reconstruction SNR at low and high doses: 1) a standard defocused probe with defocus aberration of 400 nm, 2) a defocused Fresnel Zone Plate (FZP), and 3) a randomized probe generated by a holographic phase plate and a conventional lens. Fig. 4.1 depicts these probes

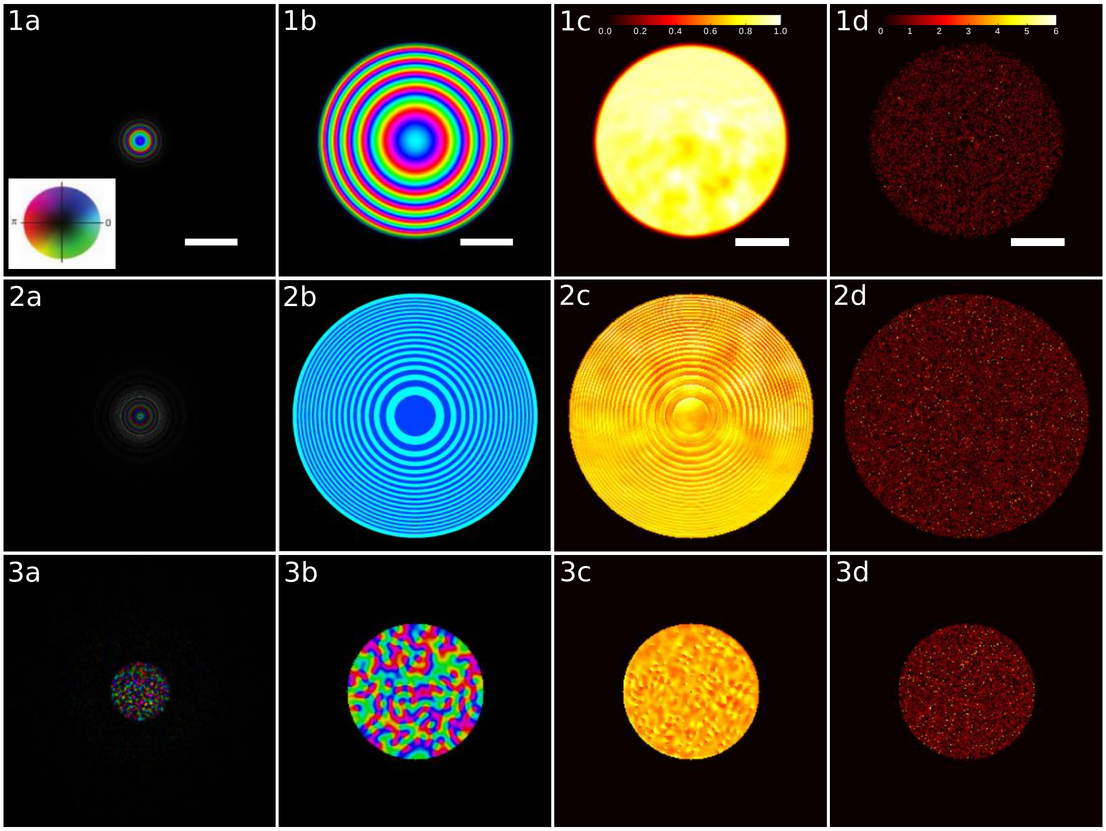

Figure 4.1: Different probes evaluated in this paper and corresponding diffraction patterns. Row 1: defocused beam with defocus aberration of 400nm, convergence half-angle 9.2 mrad; row 2: defocused beam created by a Fresnel zone plate, 600 nm from focus; row 3: randomized beam, generated by a holographic phase plate and focused by a conventional lens. Column a: beam in real space, at the sample position, scale bar is 8.5 nm; column b: beam at the probe forming aperture, scale bar is 4.5 mrad; column c: diffraction pattern of human ribosome at unlimited dose, normalized to the maximum intensity; column d): diffraction pattern for a scan with an electron dose of 20 $e^-/\mathring{A}^2$. The inset in 1a shows the color wheel that is used to represent amplitude and phase in columns a) and b).

in real and Fourier space, and typical diffraction patterns at infinite dose and low dose. The FZP was recently suggested as a phase modulator for bright-field STEM [169], because its simple phase modulation allows analytical retrieval of linear phase contrast. However, diffractive optics typically have imperfections due to the manufacturing process, which introduce errors and dose inefficiency if the reconstruction is obtained by a simple fitting procedure. Iterative ptychography algorithms allow for the simultaneous retrieval of the probe wave function [99, 121], and therefore offer full flexibility in the design of the phase profile. We test as a third probe a random illumination generated by a holographic phase plate and a focusing lens.

Fig. 4.2 shows the SNR of reconstructions of a ribosome particle with the three proposed probes as a function of spatial frequency for doses of $20\,e^-/\mathring{A}^2$ and $80\,e^-/\mathring{A}^2$. It can be seen that the simple defocused probe has almost 2 orders of magnitude worse SNR than the FZP and the random probe at the lowest spatial frequencies. At low spatial frequency the FZP achieves the best SNR, while at high spatial frequencies the random probe does slightly better. We have therefore used the random probe for the reconstructions shown in Figs. 2.5 and 2.7.

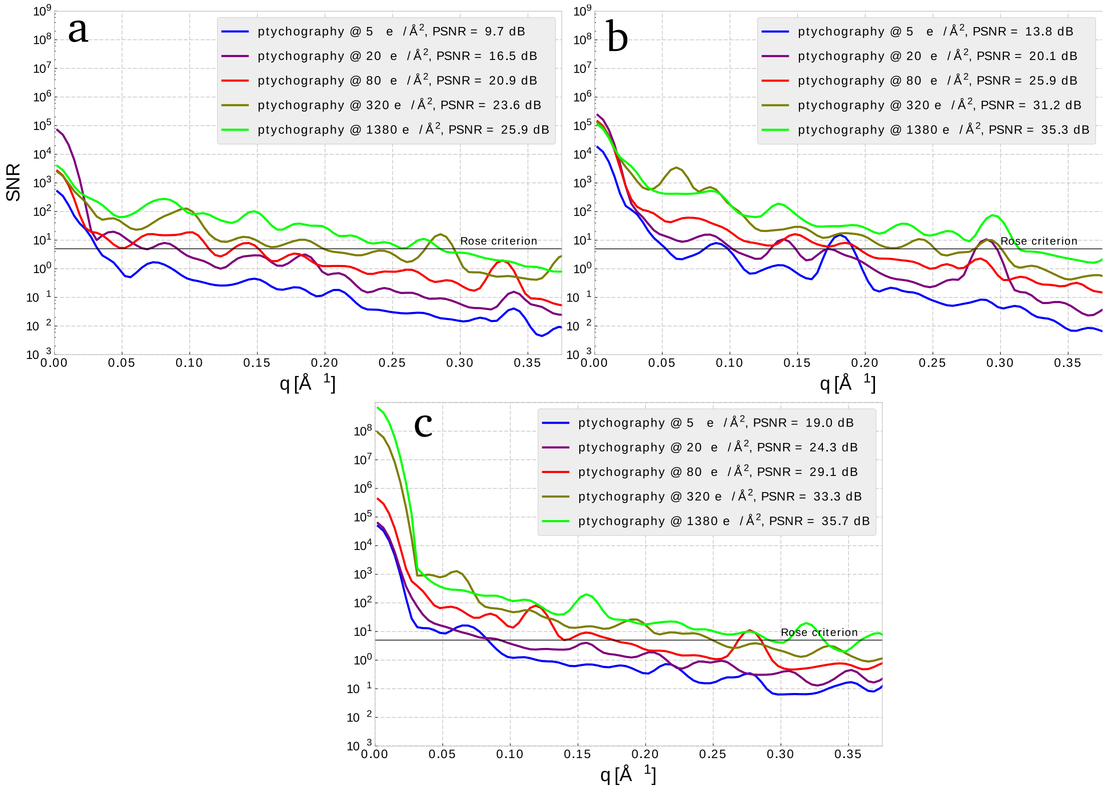

Figure 4.2: SNR of reconstructions of the human ribosome at different radiation doses using the a) defocused probe, b) the Fresnel zone plate and c) the randomized probe. (from Pelz *et al.* [96])

4.2 Design of diffuser apertures for structured illumination electron ptychography

As discussed already in section 1.3.2, the phase of an electron wave function can be manipulated by electrostatic potentials, the magnetic vector potential, as well as holographically by amplitude modulation from a specifically designed obstruction and subsequent free space space propagation to a desired plane, usually the far-field. All these approaches have been used in the recent past to shape the electron wave function, and we review them here shortly with regards to ease of fabrication, ease of implementation in the electron microscope, and flexibility.

Manipulation by electrostatic potentials is most easily achieved by inserting material into the path of the electron wave. The electrostatic potential of the atoms in the material causes a phase shift relative to vacuum. Ideally, non-crystalline materials are used to mitigate diffraction effects from propagation through the material. In this case, the phase modulation can just be described by the material thickness $h(x,y)$ and the mean inner potential V_0 of the material [170]:

$$T(x,y) = \exp\Big(i\tilde{k}h(x,y)\Big), \tag{4.1}$$

where $\tilde{k} = \sigma V_0 + i\alpha$ is the effective complex wavenumber of the electron within the material (see section 1.2.1). This is just a variation of Eq. (1.20) in section 1.2.4. The amplitude coefficient α describes the effects of inelastic and high-angle scattering and σ is the interaction constant that depends only on the energy of the beam [171]. The transmitted electron wave function immediately behind such a thickness-modulated mask is then calculated just by transmission through a single slice of material as in Equ. 1.19.

The standard material for such height-modulated masks is silicon nitride (Si_3N_4) because of its robustness, amorphousness, and easy handling for FIB milling. Usually, FIB milling is used to produce the desired height profile, and pixel sizes of 50 nm can easily be realized, such that 1000 pixels are available for a typical 50 μm diameter aperture. After calibration of the FIB to produce a certain thickness, the process to create a mask is a matter of minutes and many designs can be realized relatively quickly. A drawback is the energy dependence of the phase shift, therefore a new mask must be produced for every electron energy that is used in the experiment. It is possible to create off-axis holograms and inline holograms [170] this way, depending solely on the thickness profile, but the use of higher diffraction orders off the optical axis requires careful realignment of the microscope and is therefore impractical in otherwise already difficult low-dose ptychography experiments.

The creation of magnetic vector potentials in the beam path was suggested to create a Zernike-like phase plate [65], but a pixel-by-pixel design would involve multiple current-carrying wires and is difficult to fabricate, as already the fabrication of a single thin enough wire poses practical difficulties. Therefore, this option was not further pursued.

The last, simplest option is to fabricate an binary amplitude grating, where the desired phase is holographically imprinted such that the phase profile after a certain propagation distance has the desired properties [172]. The practical disadvantage is again the off-axis position of the hologram, requiring additional microscope alignment. Additionally, the current is greatly reduced and the required thickness to totally block the beam does not allow as fine features as pure silicon nitride masks, such that the flexibility in this regard is limited. Changing the electron energy however only changes the angle at which the desired phase profile appears.

Because of the great freedom of design, we chose to use the first method to create structured illumination masks for ptychography. Masks with 1000×1000 pixels were designed with an iterative Gerchberg-Saxton algorithm depicted in Fig. 4.3. Starting with random phases in the aperture plane, we iteratively apply amplitude projectors $\mathcal{P}_{a_r}$ and $\mathcal{P}_{a_f}$ in real and Fourier space to confine the beam to a certain area. After a few iterations, the vortex structure as shown in Fig. 4.5 evolves. Then, the algorithm is terminated and an additional phase is added to correct for the spherical aberration of the microscope. From the resulting phase profile, a stream file was created for processing in the FIB. The python code to create such a mask is displayed in appendix 6.6. An SEM image of an example resulting height profile $h(x,y)$ is shown in Fig. 4.4.

4.3 Structured illumination ptychography with a K2-IS camera and a Titan microscope: lessons learned

A first structured illumination experiment was performed at the Ernst Ruska Centre in Juelich in collaboration with Penghan Lu, who fabricated the phase masks, and Dr. Vincenzo Grillo, who generated the stream files for FIB milling and advised on important design parameters. Dr. Grillo suggested to use aper-

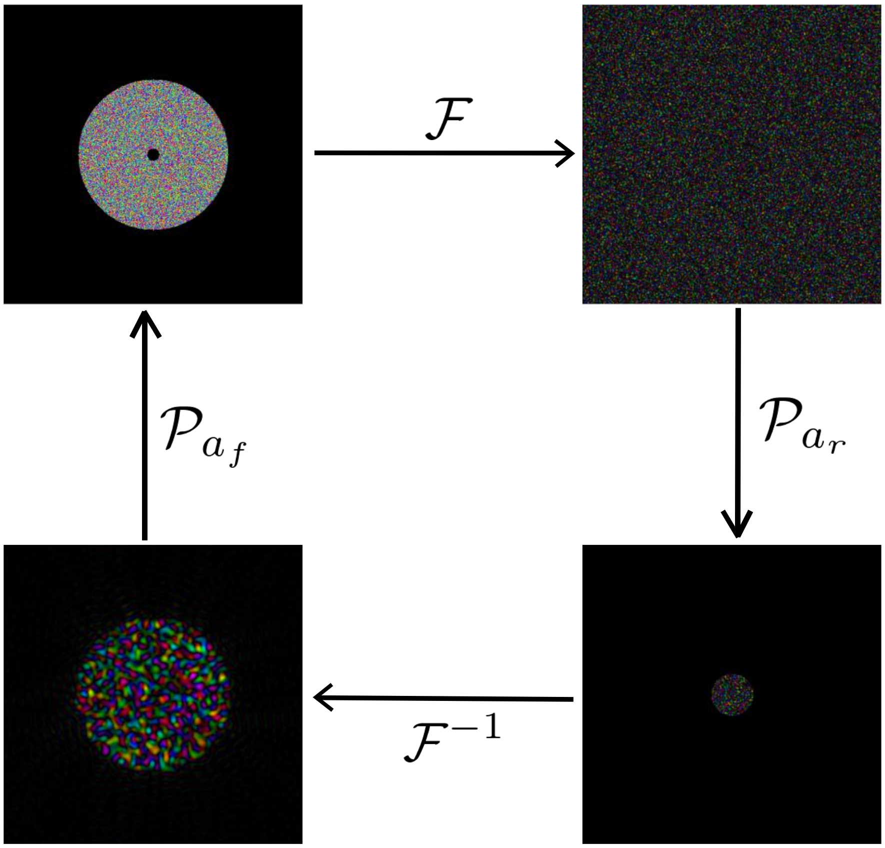

Figure 4.3: Schematic of the Gerchberg-Saxton type algorithm to create the random phase masks

tures no larger than 50 μm in diameter to reduce charging effects that appear with larger apertures. The experiments were performed at the Titan Holo microscope, which is equipped with an image abberration corrector, STEM system and a synchronized K2-IS direct detection camera. The K2-IS camera has the same Hardware specification as the K2 Summit used in section 3.3, but the full frame rate of 400 Hz is accessible for data collection. At this frame rate only integrating mode is available, and the electron counting has to be performed on the raw integrated images after data collection. This means that the electron hit rate on the camera must be in the same range as the dose rate suggested for the K2 Summit detector, i.e 3 e per pixel per second, to achieve the high DQE of the K2 in counting mode and avoid coincidence losses.

This means that the gun must be used at a very coherent setting (gun lens 9 spot 11), to achieve the low currents needed for this detector. It also means that the electron counts per pixel in a single diffraction pattern are very low, as shown

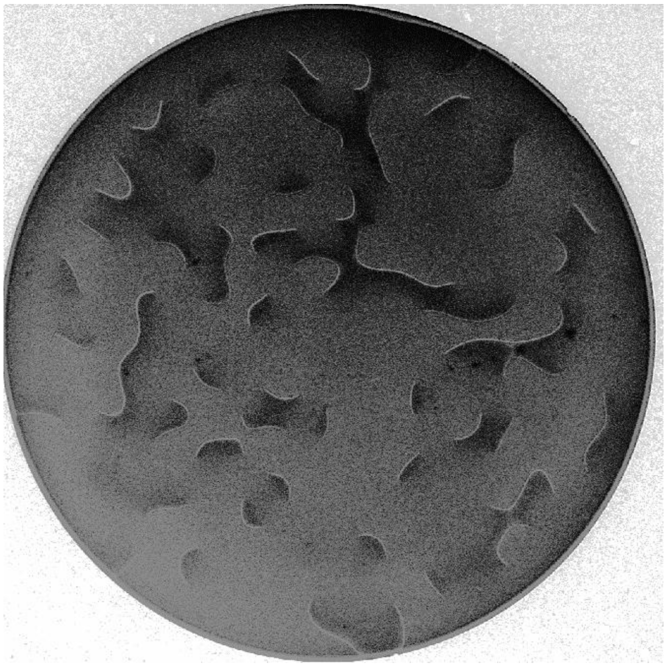

Figure 4.4: SEM image of a height profile created from a phase mask similar to Fig. 4.3. The diameter of the mask is 50 μm.

in an example pattern, after electron counting and binning by 8, shown in Fig. 4.5 c). An additional limitation of the camera software is the fact that only a single exposure can be performed at each position of a 4D STEM scan, leaving very few electrons per exposure on the detector. This means that the detector would have to be binned by a factor of 32 to achieve an average of more than 1 electron per pixel in the bright field disk.

This in turn clashed with the fact that increasing the step size and the beam diameter was the only option to achieve low enough dose to achieve less than $100\,e^-/\text{Å}^2$. It was necessary to choose a step size of 4 nm to achieve an electron dose of $50\,e^-/\text{Å}^2$ with a beam current of 2.1 pA and the 400 Hz frame rate of the K2-IS. This in turn meant that the detector could not be binned by more than 8x to achieve sufficient sampling of the probe. This lead to data sets with diffraction patterns as shown in Fig. 4.5 c).

Due to the many zero intensity pixels in the bright field, the gradient updates from a single measurement are very sparse and we were not able to reconstruct good quality images. The aforementioned limitations regarding the camera software only became clear during the experiment. Because of this, a mask that produces a beam with diameter of 5 nm at a convergence semi-angle of 7 mrad was designed to achieve a half-period resolution of 1.4 Å. The designed probe at focus is shown in Fig. 4.5 f). Because of the step size requirement, the probe had to be defocused to $-1.2\,\mu$m to achieve the desired diameter of 20 nm. The phase and amplitude profiles of this defocused probe from simulation are shown in 4.5 d) and the measured amplitude at $-1.2\,\mu$m is shown in Fig. 4.5 e). We note that the speckle size for the simulation and the experimental amplitudes are very similar, although the simulated pattern does not display the amplitude drop that is present in the center of the experimental intensity. Additionally, spurious amplitude outside the 20 nm diameter is visible in the experimental defocus image. This can be attributed to to two possible causes: either to the fact that the Si_3N_4 mask is not a perfect phase mask and inelastic and multiple scattering still occur in the material, which are not accounted for in the design process so far, or the fact that the thickness profile is not perfect and therefor the phase shift does not amount to exactly 2π, therefore creating vortices with fractional topological charge, which leak out intensity off-axis of the beam. The first reason also leads to electrons being scattered to higher angles, such that the ADF images with inserted diffuser are particularly noisy. These electrons scattered into the dark field will need to be included in the probe reconstruction. In Fig 4.5 d) on the left side it is also visible that at such a large defocus the phase profile of the defocus aberration is very dominant and the sub-nm tiling of the speckles seen in 4.5 f) is lost. It would be interesting to study how this affects the reconstruction SNR.

4.4 Conclusion and remarks

Ptychography experiments with diffuser masks at very low doses are challenging for a number of reasons. The lack of a proper online analysis tool because of the poor quality of ADF is the biggest obstacle, which can in principle be resolved by fast ptychography reconstruction. This is currently hindered by the firmware of most of the cameras, which does not allow to stream the data from the camera into memory directly, but saves it on disk before further processing. With data files f several to hundreds of GB in size, this causes a significant delay from data collection to phase contrast image.

Another obstacle is that in microscopes with two condenser systems the condenser plane is not fully in the front focal plane of the sample, so that in the diffraction plane one sees a slightly propagated aperture. This is no problem for a standard round aperture, because the Fresnel fringes are usually very small. If

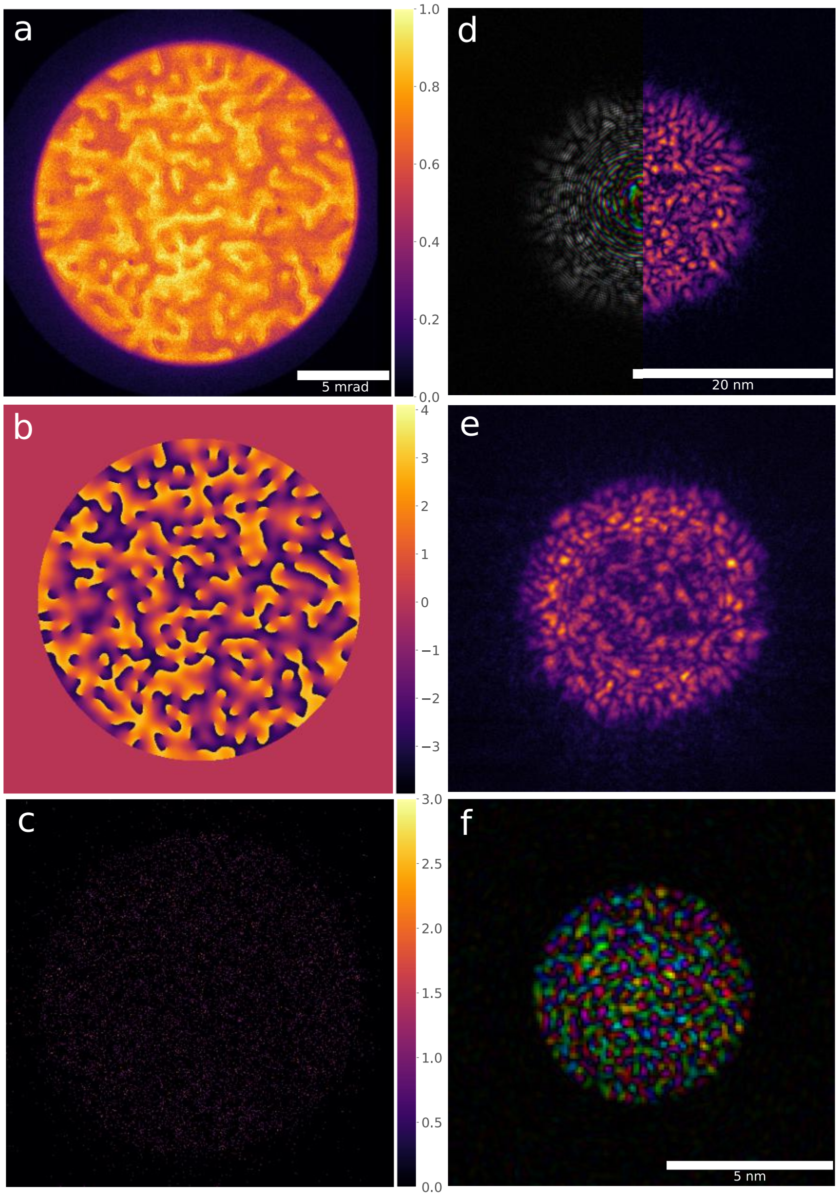

Figure 4.5: Data and simulations for the first structured illumination experiment. a) Sum of all intensities of a scan with 80×80 positions, revealing the depth profile of the SI mask. The edge of the HAADF detector blocks most of the electrons scattered into the dark field. b) aperture design with corresponding phase shift for the mask used in a). c) Experimental diffraction pattern with an 8x binning applied, resulting in 426×426 pixels. d) simulated probe with an additional defocus aberration of $1.2\,\mu\mathrm{m}$ to achieve a diameter of roughly $20\,\mathrm{nm}$. The left half shows the domain-colored complex wave, the right half shows the amplitude only. e) Experimental amplitude recorded at approximately $1.2\,\mu\mathrm{m}$ defocus. f) Simulated complex wave at focus.

a diffuser mask is used, one observes strong Fresnel fringes in the whole bright field disk because of the strong height profile of the mask. In principle this should not be a problem for the reconstruction, but it leads to a very non-uniform intensity distribution over the bright field. The effects of this need to be studied in the reconstructions.

5 Summary and future directions

After the tremendous success of cryo-EM in structural biology in the past years, the development of a reliable, quantitative and easily implementable phase contrast technique is still on the wish list of the cryo-EM practicioners.

In this thesis we show that computational phase contrast imaging via electron ptychography at the low doses required to image biological macromolecules is possible with the help of Bayesian reconstruction algorithms, and demonstrate it in two proof-of-principle experiments on two different electron microscopes. This turns cryo-electron ptychography into a viable alternative to current phase contrast imaging methods in cryo-EM, which could eventually outperform those methods, as we have shown in reconstruction from simulated data.

We have shown how ptychography relates to other phase retrieval techniques in the general framework of quantum state reconstruction and highlighted its advantages in terms of implementability, uniqueness of the reconstruction, and susceptibility to partial coherence effects.

A challenging hurdle in achieving the high resolutions of state-of-the art cryo-EM is certainly a multi-slice reconstruction at such low-doses, or implementation of another method of Ewald sphere correction for electron ptychography.

We believe that the next generation of pixelated STEM detectors enables ptychographic phase contrast imaging even on mid-range microscopes, substantially lowering the instrumental hurdles for performing phase contrast cryo-EM. A dedicated ptychographic STEM could dispatch all of the lenses after the sample and the objective lens. This would essentially be a high-voltage scanning electron microscope (SEM) with a long propagation tube, and would lower the entry cost for cryo-EM by a large amount.

In the following sections we discuss investigations that could not be performed within this thesis, but for which it could provide a starting point.

5.1 Dose rate dependence of cryo-electron ptychography

Due to limitations in camera frame rate, the experiments presented in this thesis were performed at an electron dose rate which is unusual for cryo-EM. Typical cryo-EM data collection strategies work with a dose rate of $<1\,e^{-}/\mathring{\mathrm{A}}^{2}\mathrm{s}$ and expose the sample for 20 seconds or longer, to minimize the beam-induced specimen movement [173]. While a whole scan takes a similar amount of time in ptychography as in cryo-EM, all the dose is delivered onto one sample area in a single exposure with the defocused beam. This is is because the detector usually operates already at the highest frame rate, and a dose fractionation as done in conventional cryo-EM is currently not possible. This will be alleviated with the next generation of detectors, which increase the frame rate by a factor of 10 to 50. In our experiments we used dose rates of $64\,e^{-}/\mathring{\mathrm{A}}^{2}\mathrm{s}$ in the case of the Titan Krios microscope and $557\,e^{-}/\mathring{\mathrm{A}}^{2}\mathrm{s}$, thus with one and two orders of magnitude difference to what is used with the conventional cryo-EM technique.

In the future it will be interesting to explore how the electron dose rate influences the reconstruction quality, and if dose-fractionation techniques need to be applied to achieve resolution comparable to conventional cryo-EM.

5.2 Multi-modal cryo-electron ptychography

Electron ptychography being a STEM technique has the unique advantage that incoherent images and spectroscopic signals can be collected simultaneously together with the 4D ptychographic data set. This means that in principle one could collect additionally the EDX signal and the ADF signal of a biological sample. While these signal are expected to be very weak for weakly scattering biomolecules, they could be averaged, oriented and then combined with the 3D phase contrast reconstruction. The EDX signal would be especially useful to disambiguate between elements with very similar atomic scattering potentials, which are hard to infer from the atomic potential alone, e.g. the differentiation of metal ions with very similar elastic scattering cross sections (e.g. Ca^{2+}, Mg^{2+}, Mn^{2+}). Ptychography with a focused electron probe makes it possible to collect these different incoherent signals at atomic resolution, and therefore make the most use of all available scattering cross sections [174]. Such multi-modal and correlative microscopy approaches are becoming increasingly important as the systems under study become more complex [175, 176].

5.3 Optimal experimental design

In this thesis we have made the connection between quantum state tomography and the generalized phase retrieval problem. While we studied the behavior of the reconstruction-algorithms with respect to different illuminating wave fronts, a theoretical study of the optimal experimental scheme would certainly be very fruitful. This problem could be approached from several angles, which we shortly describe in the following.
First, drawing from the connection to quantum tomography, one can explicitly design a minimal set of informationally complete measurements, also called *quorum*, which allow to reconstruct an arbitrary quantum state. In the case of pure state quantum tomography, this has been done e.g. by Pohl, Yang & Boche [177], who construct a measurement basis with 4N measurements that guarantees reconstruction of pure states, and they even provide an analytic reconstruction procedure. Carmeli *et al.* [178, 179] provide measurement bases with 5N, from which stable recovery is guaranteed. [180] discuss the minimal number of measurements that is needed to recover a pure state.

Second, one could optimize certain information theoretical measures regarding the information content of the measurements about the object. This approach has been performed by Shlezinger, Dabora & Eldar [181, 182]. They maximize the amount of mutual information between the signal of interest, in our case the transmission function, and the measurements. However, [181] performs this exercise only for the case of masked Fourier measurements, i.e a binary amplitude mask is performed in real space, before the signal is Fourier transformed and recorded. Performing such an experiment is probably very difficult with electrons, although one could imagine demagnifying an amplitude mask in the condenser aperture to the required pixel size. Demagnifying 500 nm pixels of an amplitude mask in the condenser plane to 3 Å pixels in the image plane requires a demagnification factor of 1666 and is certainly feasible, if only with an unusual electron optical configuration. An application of this information-theoretical approach to ptychography would therefore certainly be very interesting.

The third approach can be understood as an extension of the neural network implementation of generalized phase retrieval as presented in section 2.7, and an implementation of this principle is the presented `PtychoNet`. A promising branch of recent developments in machine learning focuses on optimizing experimental designs by representing a physical measurement system by a set of differentiable transformations, such that back-propagation of errors is possible via the chain rule. An example of such neural network for ptychography was presented in section 2.7, with the operator **P** being the differentiable ptychographic measurement operator. Once a network presenting the measurement process is defined, the optimization loop of an algorithm like Algorithm 2 can be *unrolled* [183–185], such that the whole optimization is a simple forward pass through the unrolled network.

This allows now to propagate gradients back through the whole optimization algorithm, for example making it possible to optimize the probe wave function to achieve the best spectral SNR, or the smallest residual error when compared to a ground truth. *scikit-pr* lays the groundwork for this next step by implementing ptychographic phase retrieval as a neural network.

This approach was recently demonstrated for Fourier ptychography with visible light [186], showing that phase recovery from only 2N measurements is possible, and showing that the mean squared error of the reconstruction can be improved by over 80 % when optimizing the illumination system compared to conventional illumination.

5.4 Inelastic electron ptychography - quantum tomography of specimen excitations

Electron microscopes have developed into extremely versatile instruments, enabling the collection not only of high-resolution images, but also of spectral information with extremely high spatial resolution. When using a post-specimen energy filter, it is possible to select inelastically electrons with a very narrow range of energy losses. Electrons with the same final state after interaction with a specimen where only single scattering occurs interfere coherently, and form a coherent diffraction pattern like elastically scattered electrons. It should therefore be possible to reconstruct the inelastic mode of the object they were scattered from.

This has already been demonstrated with the differential phase contrast technique on nano-rods which exhibit surface plasmon excitations from passing high-energy electrons [187]. A natural extension would be to apply ptychography to get a full picture of the excitation modes of the specimen. Since the inelastic cross sections for a very narrow electron energy loss range are very small, the

Bayesian techniques presented in this thesis could prove very useful for the data analysis.

6 Appendix

6.1 Some conventions

Variables

We adopt the following conventions for variables:
A variable in lower case bold-face type represents a vector, $\mathbf{a} \in \mathbb{C}^n, \mathbb{R}^n$.
A variable in upper case bold-face type represents a linear operator, $\mathbf{A} \in \mathbb{C}^{n\times n}, \mathbb{R}^{n\times n}$.
A variable in sans-serif type represents an integer number, $\mathsf{a} \in \mathbb{Z}, \mathbb{N}$.
A variable in italic type is usually a scalar, $a \in \mathbb{C}, \mathbb{R}$.

Fourier transform

For functions $\mathrm{g}, \mathrm{h} : \mathbf{x} \in \mathbb{R}^{\mathrm{n}} \to \mathrm{g}(\mathbf{x}) \in \mathbb{C}$, we denote

$$\mathcal{F}\left[g\right](\mathbf{v}) \equiv \int_{\mathbb{R}^n} g(\mathbf{x}) e^{-2\pi i \mathbf{x}\mathbf{v}} \, \mathrm{d}\mathbf{x} \,, \tag{6.1}$$

as the *Fourier transform* of g and indicate it with the symbol $\mathcal{F}$. Usually, the domain of integration is inferred from the integration variable and the domain subscript is dropped when the integration includes the whole vector space. The inverse transformation to Eq. (6.1) is called the *inverse Fourier transform* and indicated by the label $\mathcal{F}^\dagger$,

$$\mathcal{F}^\dagger\left[h\right](\mathbf{x}) \equiv \int_{\mathbb{R}^n} h(\mathbf{v}) e^{2\pi i \mathbf{x}\mathbf{v}} \, \mathrm{d}\mathbf{v} \tag{6.2}$$

If only a subspace of $\mathbb{R}^n$ is integrated, we indicate this with a subscript to the label $\mathcal{F}$. For example, for $(\mathbf{x}, \mathbf{y}) \in \mathbb{R}^2 \times \mathbb{R}^2$, we write the two-dimensional Fourier transform with respect to $\mathbf{x}$ as

$$\mathcal{F}_{\mathbf{x}}\left[g(\mathbf{x}, \mathbf{y})\right](\mathbf{v}, \mathbf{y}) \equiv \int g(\mathbf{x}, \mathbf{y}) e^{-2\pi i \mathbf{x}\mathbf{v}} \, \mathrm{d}\mathbf{x} \,, \tag{6.3}$$

such that a short hand notation is possible, e.g. $\mathcal{F}_{\mathbf{x}}\left[\exp\left(\mathbf{x}^2\mathbf{y}^2\right)\right](\mathbf{v}, \mathbf{y})$. In cases where the argument $\mathbf{v}$ is not needed in an equation, we can use the shorter form

$$\mathcal{F}_{\mathbf{x}}\left[g(\mathbf{x}, \mathbf{y})\right] \equiv \int g(\mathbf{x}, \mathbf{y}) e^{2\pi i \mathbf{x}\mathbf{v}} \, \mathrm{d}\mathbf{x} \,. \tag{6.4}$$

In cases where the argument of the Fourier transform is clear, we may omit the argument brackets for brevity. We also introduce an additional shorthand for Fourier transforms of functions of a single variable:

$$\tilde{f}(\mathbf{v}) \equiv \mathcal{F}\left[g(\mathbf{v})\right] \tag{6.5}$$

Fourier slice theorem

The *Fourier slice theorem* or *projection-slice theorem* [188] states that "the Fourier transform of the projection of an N-dimensional function $f(\mathbf{r})$ onto an m-dimensional linear submanifold is equal to an m-dimensional submanifold is equal to an m-dimensional slice of the N-dimensional Fourier transform of that function consisting of an m-dimensional linear submanifold through the origin in the Fourier space which is parallel to the projection manifold." [189]

Fractional Fourier Transform

The fractional Fourier transform is a generalization of the Fourier transform that gives access to a continuum of functions joining the original function and its Fourier transform. The fractional Fourier transform of degree θ is defined as

$$\mathcal{F}_\theta\left[g\right](\mathbf{v}) \equiv \left[\frac{\tan(\theta) - i}{\pi\tan(\theta)}\right]\int_{\mathbb{R}^n} g(\mathbf{x})\exp\left(\pi i\frac{(x^2 + v^2)\cos(\theta) - 2\mathbf{x}\mathbf{v}}{2\sin(\theta)}\right)\mathrm{d}\mathbf{x}\,. \tag{6.6}$$

Notice that, for $\theta = 0$ and $\theta = \pi/2$, the fractional Fourier transform reduces, respectively, to the original function and its Fourier transform

$$\mathcal{F}_0\left[g(\mathbf{x})\right](\mathbf{v}) = g(\mathbf{x}) \tag{6.7}$$

$$\mathcal{F}_{\pi/2}\left[g(\mathbf{x})\right](\mathbf{v}) = \mathcal{F}\left[g\right](\mathbf{v}) \tag{6.8}$$

Convolution and cross-correlation

For functions $g, h : \mathbf{x} \in \mathbb{R}^n \to g(\mathbf{x}) \in \mathbb{C}$, we define

$$g(\mathbf{x}) \star h(\mathbf{x}) \equiv (f \star g)(\mathbf{x}) = \int f^*(\mathbf{y})g(\mathbf{y} + \mathbf{x})\,\mathrm{d}\mathbf{y}\,. \tag{6.9}$$

as the *cross-correlation* and

$$g(\mathbf{x}) \otimes h(\mathbf{x}) \equiv (f \otimes g)(\mathbf{x}) = \int f(\mathbf{y})g(\mathbf{y} - \mathbf{x})\,\mathrm{d}\mathbf{y} \tag{6.10}$$

as the *convolution* of f and g. Both may be expressed in term of Fourier transforms,

$$\mathcal{F}[g(\mathbf{x}) \otimes h(\mathbf{x})] = \mathcal{F}g \cdot \mathcal{F}h \tag{6.11}$$

and

$$\mathcal{F}[g(\mathbf{x}) \star h(\mathbf{x})] = \mathcal{F}g \cdot (\mathcal{F}h)^{\dagger}. \tag{6.12}$$

If either convolution or cross-correlation is carried out on a subspace of $\mathbb{R}^n$, we indicate this with a subscript to the label $\star$ or $\otimes$ as follows:

$$g(\mathbf{x}, \mathbf{y}) \otimes_{\mathbf{y}} h(\mathbf{x}, \mathbf{y}) \equiv \int g(\mathbf{x}, \mathbf{w}) h(\mathbf{x}, \mathbf{y} - \mathbf{w}) d\mathbf{w} \tag{6.13}$$

6.2 Json metadata file from the Tecnai F20 microscope in Hamburg

Below we show the contents of a typical metadata file as produced by the custom software written by Robert Buecker.

```
{
    "Scanning": {
        "Total Pts": 4096,
        "Scan complete": false,
        "Idx": {
            "y": 0,
            "x": 0
        },
        "Curr Point": 0,
        "Pixel size": {
            "y": 0.21484375,
            "x": 0.21484375
        },
        "Frame dose": NaN,
        "Parameters": {
            "Smp/Pos": 1,
            "Mask file": "",
            "Pattern": 0,
            "Continuous": false,
            "Rate": 500.0,
            "Pre-pts": 0,
            "Frame (Y)": {
```

```
                "Extend Scan": false,
                "Max V": 7.5,
                "ROI st": 32,
                "ROI len": 64,
                "Min V": -7.5,
                "Pts": 128
            },
            "Line (X)": {
                "Extend Scan": false,
                "Max V": 7.5,
                "ROI st": 32,
                "ROI len": 64,
                "Min V": -7.5,
                "Pts": 128
            }
        },
        "Current": NaN,
        "Running": false,
        "Field of view": {
            "y": 220.0,
            "x": 220.0
        },
        "Position": {
            "y": 3.72047244094488,
            "x": 3.72047244094488
        }
    },
    "STEM Image": {
        "Name Root": "ADF",
        "Image Directory": "C:\\Data\\Robert\\20180606_Ferritin",
        "File Inc": true,
        "File No": 1530,
        "Autosave": true,
        "Filename": "ADF_01530",
        "Save": false
    },
    "Projection": {
        "ImageBeamShift": {
            "Y": 0.0,
            "X": 0.0
        },
        "LensProgram": 1,
```

```
        "Defocus": 6e-07,
        "CameraLength": 1.0,
        "ObjectiveExcitation": 0.888735340391214,
        "Focus": 0.00331796012784327,
        "ImageBeamTilt": {
            "Y": 0.0,
            "X": 0.0
        },
        "ImageShift": {
            "Y": 0.0,
            "X": 0.0
        },
        "SubModeString": "STEM nano D",
        "Magnification": 320000.0,
        "MagnificationIndex": 0,
        "SubMode": 6,
        "Mode": 2,
        "CameraLengthIndex": 11,
        "TEMMagnification": -1.0,
        "TEMCamLength": 1005.0,
        "DiffractionShift": {
            "Y": -0.000261798,
            "X": 0.0
        },
        "ProjectionIndex": 11
    },
    "Screen": {
        "MainScreen": 2,
        "IsSmallScreenDown": true,
        "ScreenCurrent": 0.0609916998816225,
        "Dose": 0.684837795378426
    },
    "Time Stamp": "2018-06-06T19:14:12.218Z",
    "Gun": {
        "HTValue": 200000.0,
        "Shift": {
            "Y": -0.00169399145477323,
            "X": 0.0112431831204754
        },
        "HTState": 3,
        "Tilt": {
            "Y": -0.459406323081482,
```

```json
            "X": 0.552593046995164
        }
    },
    "LowDose": {
        "LowDoseState": 0,
        "BeamBlanked": true,
        "Dose": 0.0
    },
    "Illumination": {
        "CalibCurrent": NaN,
        "CalibDiameter": NaN,
        "Shift": {
            "Y": 0.0,
            "X": 0.0
        },
        "BeamBlanked": true,
        "CalibDoseRate": NaN,
        "STEMSize": 440.0,
        "Intensity": 0.379443834592606,
        "Mode": 0,
        "Tilt": {
            "Y": 0.0,
            "X": 0.0
        },
        "SpotsizeIndex": 9,
        "StemMagnification": 320000.0,
        "StemRotation": -0.202300000000001
    },
    "Detector": {
        "Layout": "1556X516",
        "FrameNumbers": 4096,
        "LatestImageNumber": -1,
        "ConfigFilePath": "/localdata/share/config",
        "FilePreExt": "",
        "FreeBuffer": 24576,
        "CompressorShuffle": false,
        "Width": 1556,
        "DelayTime": 0.0,
        "PrecompressEnabled": true,
        "ShutterTimeMin": 0.0,
        "SaveFilePath": "/scratch/20180606",
        "OperatingMode": "ContinuousReadWrite",
```

```
        "CompressionEnabled": true,
        "Status": "Detector ID is:0?0.State is:*ON*\n",
        "DistortionCorrection": 1,
        "FileNamePathCaseSensitive": true,
        "CompressionRate": 2,
        "FilePostfix": "nxs",
        "TotalLossFrames": 1,
        "FilePrefix": "FerritinPtychoLoDef",
        "ShutterTime": 2.0,
        "LiveMode": true,
        "ThreadNo": 0,
        "Depth": 12,
        "FileStartNum": 71,
        "TriggerMode": 2,
        "CreateDir": false,
        "FramesPerFile": 4096,
        "SaveAllImages": true,
        "SaveFileName": "FerritinPtychoLoDef_00071",
        "CheckFileExists": false,
        "Height": 516,
        "EnergyThreshold": 44000.0,
        "LiveFrameNo": 0,
        "ShutterTimeMax": 2147483647.0,
        "AppendData": false
    },
    "Stage": {
        "Status": 0,
        "A": 1.70344134994647e-05,
        "Y": 0.0002325774,
        "X": 4.61565e-05,
        "Z": -4.203087e-05,
        "Holder": 1
    }
}
```

6.3 Json config file for `slice++`

```json
{
"nthreads":"1",
"wave":{
"phi_33":"0.000000",
"phi_31":"0.000000",
"gaussian":"false",
"phi_55":"0.000000",
"phi_51":"0.000000",
"phi_53":"0.000000",
"tiltX":"0",
"tiltY":"0",
"astigmatismAngle":"0.000000",
"phi_44":"0.000000",
"a_44":"0.000000",
"defocus":"500",
"a_62":"0.000000",
"a_66":"0.000000",
"a_64":"0.000000",
"AISaperture":"0.0",
"type":"2",
"dE/E":"0.00000",
"C5":"0.000000",
"a_42":"0.000000",
"astigmatism":"0",
"dI/I":"0.00000",
"dV/V":"0.000003",
"phi_62":"0.000000",
"phi_42":"0.000000",
"phi_66":"0.000000",
"alpha":"10",
"a_31":"0.000000",
"a_33":"0.000000",
"Cc":"1",
"smooth":"true",
"gaussScale":"1.0",
"a_55":"0.000000",
"a_53":"0.000000",
"a_51":"0.000000",
"Cs":"0",
```

```
"phi_64":"0.000000"
},
"beam":{
"sourceDiameterAngstrom":"0",
"dwellTimeMsec":"1.6021773e-4",
"beamCurrentpA":"1",
"energy_keV":"200.000000"
},
"mode":"1",
"output":{
"showProbe":"false",
"writeLogFile":"false",
"loglevel":"1",
"SaveWaveAfterTransform":"true",
"SaveWaveAfterNSlices":"1",
"logFileName":"slicelog.log",
"pendelloesungPlot":"false",
"SaveAtomicPotential":"false",
"savePath":"/home/philiipp/projects/slicepp/Examples/configs/gold.h5",
"readPotential":"false",
"SaveWaveAfterPropagation":"true",
"SaveWaveAfterTransmit":"true",
"folder":"CBED",
"saveProjectedPotential":"true",
"saveProbe":"true",
"SaveWaveAfterSlice":"true",
"savePotential":"true"
},
"model":{
"resolutionCalculation":"2",
"centerSample":"false",
"slices":"80",
"beamTiltY":"0.000000",
"beamTiltX":"0.000000",
"resolutionXAngstrom":"0.050000",
"sliceThicknessAngstrom":"2.039125",
"nx":"256",
"tds":"false",
"centerSlices":"false",
"potential":{
"DoZInterpolation":"true",
"UseQPotentialOffsets":"true",
```

```
"periodicZ":"false",
"plotVr_r":"false",
"periodicXY":"false",
"FFT":"true",
"atomRadiusAngstrom":"5.0",
"saveProjectedPotential":"true",
"savePotential":"false",
"structureFactors":"1",
"3D":"true"
},
"sliceThicknessCalculation":"2",
"tiltBack":"false",
"displacementType":"3",
"tdsRuns":"1",
"resolutionYAngstrom":"0.050000",
"ny":"256"
},
"stem":{
"scan_y_pixels":"1",
"scan_x_stop":"10.570000",
"position":"of",
"bottom":"right",
"top":"left",
"scan":"window",
"scan_y_stop":"11.300000",
"scan_x_start":"10.570000",
"corner":"of",
"scan_y_start":"11.300000",
"scan_x_pixels":"1"
},
"structure":{
"zOffset":"0",
"ncellz":"7",
"rotateToZoneAxis":"false",
"isBoxed":"false",
"structure_filename":"/home/philiipp/projects/slicepp/Examples/cif/au.cif",
"crystalTiltY":"0.000000",
"crystalTiltX":"0.000000",
"yOffset":"0.000000",
"zoneAxis":"0,1,0",
"ncellx":"5",
"ncelly":"5",
```

```
"temperatureK":"300.000000",
"boxZ":"40",
"boxY":"40",
"crystalTiltZ":"0.000000",
"xOffset":"0.000000",
"boxX":"40"
}
}
```

6.4 Example cif file of Si_3N_4

```
data_1001248
_chemical_name_systematic          'Silicon nitride - $-beta'
_chemical_formula_structural       'Si3 N4'
_chemical_formula_sum              'N4 Si3'
_publ_section_title
;
Modifications structurales du nitrure de silicium en fonction de la
temperature
;
loop_
_publ_author_name
'Billy, M'
'Labbe, J C'
'Selvaraj, A'
'Roult, G'
_journal_name_full                 'Materials Research Bulletin'
_journal_coden_ASTM                MRBUAC
_journal_volume                    18
_journal_year                      1983
_journal_page_first                921
_journal_page_last                 934
_cell_length_a                     7.6322(6)
_cell_length_b                     7.6322(6)
_cell_length_c                     2.9191(4)
_cell_angle_alpha                  90
_cell_angle_beta                   90
_cell_angle_gamma                  120
_cell_volume                       147.3
```

```
_cell_formula_units_Z              2
_symmetry_space_group_name_H-M     'P 63/m'
_symmetry_Int_Tables_number        176
_symmetry_cell_setting             hexagonal
loop_
_symmetry_equiv_pos_as_xyz
'x,y,z'
'-y,x-y,z'
'y-x,-x,z'
'-x,-y,1/2+z'
'y,y-x,1/2+z'
'x-y,x,1/2+z'
'-x,-y,-z'
'y,y-x,-z'
'x-y,x,-z'
'x,y,1/2-z'
'-y,x-y,1/2-z'
'y-x,-x,1/2-z'
loop_
_atom_type_symbol
_atom_type_oxidation_number
N3-   -3.000
Si4+   4.000
loop_
_atom_site_label
_atom_site_type_symbol
_atom_site_symmetry_multiplicity
_atom_site_Wyckoff_symbol
_atom_site_fract_x
_atom_site_fract_y
_atom_site_fract_z
_atom_site_occupancy
_atom_site_attached_hydrogens
_atom_site_calc_flag
N1     N3-     2 c 0.3333 0.6667 0.25 1.   0 d
N2     N3-     6 h 0.3394 0.0362 0.25 1.   0 d
Si1    Si4+    6 h 0.1952 0.7656 0.25 1.   0 d
_cod_database_code 1001248
```

6.5 Ground truth images used for the FRC calculation

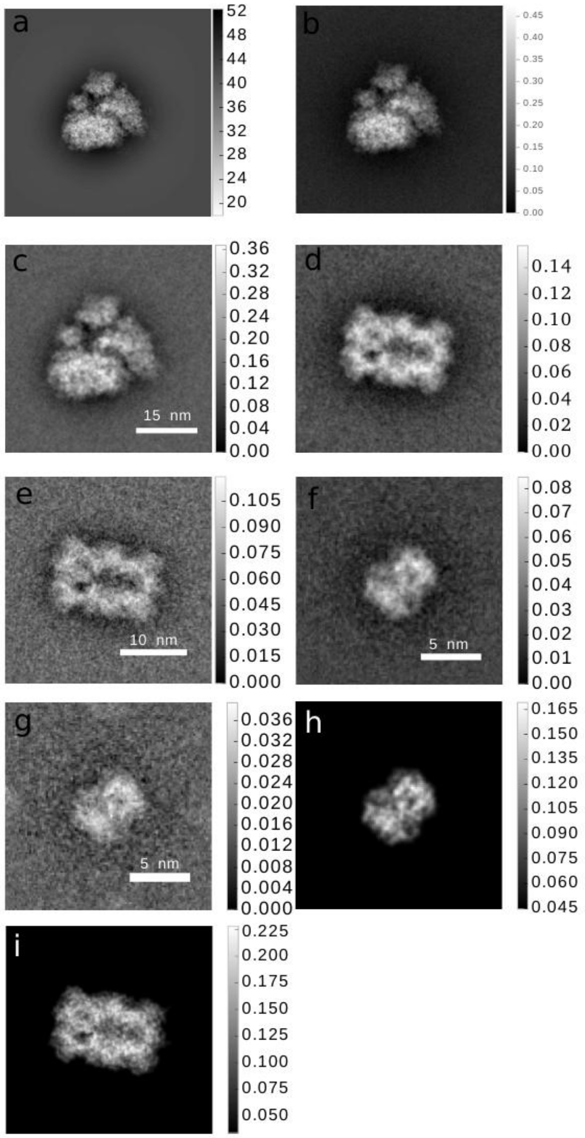

Figure 6.1: Images used for calculating the FRC plots in the manuscript: a) ground truth for phase-plate TEM and defocus TEM of ribosome at $20\,e^-/\text{Å}^2$. b) Second averaged ribosome image for average FRC calculation at $20\,e^-/\text{Å}^2$ c) Second averaged ribosome image for average FRC calculation at $5\,e^-/\text{Å}^2$ d) Second averaged proteasome image for average FRC calculation at $20\,e^-/\text{Å}^2$ e) Second averaged proteasome image for average FRC calculation at $5\,e^-/\text{Å}^2$ f) Second averaged hemoglobin image for average FRC calculation at $20\,e^-/\text{Å}^2$ g) Second averaged hemoglobin image for average FRC calculation at $5\,e^-/\text{Å}^2$ h) ground truth for phase-plate TEM and defocus TEM at $20\,e^-/\text{Å}^2$

6.6 Python code to generate a vortex mask

```
def random_probe(N, rs_rad, fs_rad1, fs_rad2, iterations=50):
    """
    Return a vortex mask of shape (N,N) with a radius of N*rs_rad in real space
    and N * fs_rad1 outer radius and N * fs_rad2 inner radius in Fourier space.
    """
    def sector_mask(shape, centre, radius, angle_range):
        """
        Return a boolean mask for a circular sector. The start/stop angles in
        `angle_range` should be given in clockwise order.
        """

        x, y = np.ogrid[:shape[0], :shape[1]]
        cx, cy = centre
        tmin, tmax = np.deg2rad(angle_range)

        # ensure stop angle > start angle
        if tmax < tmin:
        tmax += 2 * np.pi

        # convert cartesian --> polar coordinates
        r2 = (x - cx) * (x - cx) + (y - cy) * (y - cy)
        theta = np.arctan2(x - cx, y - cy) - tmin

        # wrap angles between 0 and 2*pi
        theta %= (2 * np.pi)

        # circular mask
        circmask = r2 <= radius * radius

        # print 'radius - ', radius

        # angular mask
        anglemask = theta < (tmax - tmin)

        return circmask * anglemask
    sx = rs_rad
    rs_mask = sector_mask((N, N), (N / 2, N / 2), rs_rad, (0, 360)).astype(np.float)
    # rs_mask = nd.gaussian_filter(rs_mask.astype(np.float),10)
    n = norm(rs_mask, 1)
    rs_mask = rs_mask / n
    fs_mask1 = sector_mask((N, N), (N / 2, N / 2), fs_rad1, (0, 360)).astype(np.float)
    fs_mask2 = sector_mask((N, N), (N / 2, N / 2), fs_rad2, (0, 360)).astype(np.float)
    fs_mask3 = np.logical_not(sector_mask((N, N), (N / 2, N / 2), fs_rad2, (0, 360)))
    # riplot(fs_mask3)   + + 3*fs_mask2.astype(np.int)
    fs_mask = (fs_mask1.astype(np.float)) * fs_mask3.astype(np.float)
    fs_mask[N / 2 - s:N / 2 + s, :] = 0
    fs_mask[: , N / 2 - s:N / 2 + s] = 0
    fs_mask = fs_mask / norm(fs_mask, 1)
    sh = fs_mask.shape

    fs_mask = fftshift(fs_mask)

    fac = 1
    phase = 2 * np.pi * zoom(np.random.uniform(size=(N / fac, N / fac)), fac)
    psi_f = fftshift(fs_mask * np.exp(2j * phase))

    psi_f = ifftshift(psi_f)
    it = iterations
    for i in range(it):

        psi = fftshift(ifft2(psi_f, norm='ortho'))

        psir = psi.real
        psii = psi.imag
```

```

        psi = rs_mask * (psir + 1j * psii)  # np.exp(1j*np.angle(psi))#(psir + 1j* psii)
        psi = psi / norm(psi)


        r = int(rs_rad * 1.1)

        psi_f = fft2(ifftshift(psi), norm='ortho')
        psi_fangle = np.angle(psi_f)
        psi_f = fs_mask * np.exp(1j * psi_fangle)
        psi_f = psi_f / norm(psi_f)
    psi = fftshift(fft2(psi_f, norm='ortho'))

    return np.real(psi).astype(np.float32), np.imag(psi).astype(np.float32)
```

6.7 Data preprocessing code

```
import json
import math as m
import time
import datetime
import mrcfile
import numpy as np
import pytiff
from astropy.convolution import Gaussian2DKernel, interpolate_replace_nans
from numpy.fft import ifft2, fftshift
from numpy.linalg import norm
from si_prefix import si_format
from scipy import ndimage as ni

import h5rw as rw
import plot as io
import skpr.util as u
from skpr.simulation import probe
import matplotlib.pyplot as plt
from scipy.interpolate import interp1d
import os
import dask.array as da
from dask import compute, delayed
import dask.threaded
import multiprocessing
import h5py


class DataPreparation:
        def __init__(self, path='./', save_path='./', name='R4_00009', mask_file='./Ref12bit_pxmask.tif', \
                                 reference_file='./Ref12bit_reference.mrc',\
                                 q_max_rel=1.1, data_size=None, exclude_indices=[], \
                                 binning_factor=1, min_fraction_valid=0.5,\
                                 interpolate_dead_pixels=True, binary_mask_file=None,\
                                 save_suffix='processed', fast_axis=1,\
                                 save_hdf5=True, save_matlab=False,\
                                 experiment_geometry_entry='auto',\
                                 experiment_geometry=None, theta=0, select_area=False,
                                 selected_area_start=[0, 0],\
                                 selected_area_size=64, file_extension='.nxs',\
                                 data_entry='/entry/instrument/detector/data',\
                                 mirror=[1, 1], defocus_auto=True, \
                                 mask_from_varmean=False, varmean_tolerance=0.1,\
                                 dp_centering_method='linear', metadata_file=None,\
                                 do_plot=True, blur_stem=0, manual_data_selection=False,\
                                 clip_interactive_data=True, cpu_count=None,\
                                 gap_mask_file=None, vacuum_measurements=None):
                self.manual_data_selection = manual_data_selection
                self.blur_stem = blur_stem
                self.path = path
                self.save_path = save_path
                self.name = name
                self.mask_file = mask_file
                self.gap_mask_file = gap_mask_file
                self.reference_file = reference_file
```

```
        self.q_max_rel = q_max_rel
        self.exclude_indices = exclude_indices
        self.binning_factor = binning_factor
        self.min_fraction_valid = min_fraction_valid
        self.interpolate_dead_pixels = interpolate_dead_pixels
        self.binary_mask_file = binary_mask_file
        self.save_suffix = save_suffix
        self.fast_axis = fast_axis
        self.save_hdf5 = save_hdf5
        self.save_matlab = save_matlab
        self.experiment_geometry_entry = experiment_geometry_entry
        self.experiment_geometry = experiment_geometry
        self.theta = theta
        self.select_area = select_area
        self.selected_area_start = selected_area_start
        self.selected_area_size = selected_area_size
        self.file_extension = file_extension
        self.data_entry = data_entry
        self.mirror = mirror
        self.defocus_auto = defocus_auto
        self.mask_from_varmean = mask_from_varmean
        self.varmean_tol = varmean_tolerance
        self.data_size = data_size
        self.metadata_file = metadata_file
        self.do_plot = do_plot
        self.clip_interactive_data = clip_interactive_data
        self.cpu_count = multiprocessing.cpu_count() if cpu_count is None else cpu_count
        self.vacuum_measurements = vacuum_measurements

        self.radius = np.array([250])
        self.radius_aperture = np.array([250])
        self.radius_aperture_inner = np.array([250])
        self.c1 = np.array([0, 0, 0])
        self.c2 = np.array([0, 0, 0])
        self.c3 = np.array([0, 0, 0])
        self.pos1 = np.array([0, 0, 0])
        self.pos2 = np.array([0, 0, 0])
        self.dp_centering_method = dp_centering_method

        self.valid_mask = None
        self.bin_mask_positions = None
        self.data = None
        self.pos = None

    def gap_mask(self, ms):
        gm = np.ones(ms, dtype=np.float32)
        b = 3
        gm[ms[0] / 2 - b:ms[0] / 2 + b, :] = 0
        gm[:, ms[1] / 2 - b:ms[1] / 2 + b] = 0
        gm[:, ms[1] / 2 - 256 - b - b:ms[1] / 2 - 256 - b + b] = 0
        gm[:, ms[1] / 2 + 256 + b - b:ms[1] / 2 + 256 + b + b] = 0
        gm[:, ms[1] / 2 - 512 - 3 * b - b:ms[1] / 2 - 512 - 3 * b + b] = 0
        gm[:, ms[1] / 2 + 512 + 3 * b - b:ms[1] / 2 + 512 + 3 * b + b] = 0
        return gm

    def load_binary_position_mask(self):
        if self.binary_mask_file is not None:
            print('Loading binary position mask ...')
            with pytiff.Tiff(self.binary_mask_file) as handle:
                im = np.array(handle) * -1
                bin_mask_positions = im.astype(np.bool)
            if self.do_plot:
                io.plot(bin_mask_positions.astype(np.int), 'binary position mask')
        else:
            bin_mask_positions = np.ones((self.stepy, self.stepx)).astype(np.bool)
        # bin_mask_positions = np.transpose(bin_mask_positions)
        print('Binary position mask size :', bin_mask_positions.shape)
        print('Binary position mask entries: %d' % bin_mask_positions.sum())
        return bin_mask_positions

    def load_hot_pixel_mask(self):
        s = self.data.shape
        if self.mask_file is not None:
            print('Loading hot pixel mask ...')
            with pytiff.Tiff(self.mask_file) as handle:
                im = np.abs(np.array(handle))
                # print(im.dtype)
                # if self.do_plot:
                # io.plot(im, 'hot pixel mask file')
                mask = (1 - im / im.max()).astype(np.int8)
            if self.do_plot:
```

```
                                io.plot(mask, 'hot pixel mask')
                        mask = mask[self.com[0] - self.rr:self.com[0] + self.rr,\
                         self.com[1] - self.rr:self.com[1] + self.rr].copy()
                else:
                        mask = np.ones((s[1], s[2]))
                        print(mask.shape, s)
                return np.broadcast_to(mask[np.newaxis, ...], s)

        def load_gap_mask(self):
                s = self.data.shape
                if self.gap_mask_file is not None:
                        print('Loading gap pixel mask ...')
                        with pytiff.Tiff(self.gap_mask_file) as handle:
                                im = np.abs(np.array(handle))
                                # print(im.dtype)
                                # if self.do_plot:
                                # io.plot(im, 'hot pixel mask file')
                                mask = (1 - im / im.max()).astype(np.int8)
                        if self.do_plot:
                                io.plot(mask, 'gap pixel mask')
                        mask = mask[self.com[0] - self.rr:self.com[0] + self.rr,\
                         self.com[1] - self.rr:self.com[1] + self.rr].copy()
                else:
                        mask = np.ones((s[1], s[2]))
                return np.broadcast_to(mask[np.newaxis, ...], s)

        def load_correction_factor(self, s):
                print('Loading correction factors ...')
                if self.reference_file is not None:
                        filename, file_extension = os.path.splitext(self.reference_file)
                        if file_extension == '.mrc':
                                with mrcfile.open(self.reference_file) as mrc:
                                        correction_factor = 1 / mrc.data
                        else:
                                with pytiff.Tiff(self.reference_file) as handle:
                                        im = np.array(handle)
                                        correction_factor = 1 / im
                        correction_factor = correction_factor[self.com[0] - self.rr:self.com[0]\
                         + self.rr, self.com[1] - self.rr:self.com[1] + self.rr].copy()
                else:
                        correction_factor = np.ones((s[1], s[2]))
                return correction_factor

        def prepare_stem_image(self):
                print('Preparing STEM image ...')
                s = self.data.shape
                bf_mask = u.sector_mask((self.M / self.binning_factor, self.M / self.binning_factor),
                               (self.M2 / self.binning_factor, self.M2 / self.binning_factor),
                               self.radius_aperture_inner / self.binning_factor, (0, 360))
                df_mask = np.logical_not(bf_mask)
                data_split = np.array_split(self.data, self.cpu_count, 0)
                bf_stem_list = [delayed(lambda x, y: np.sum(x * y, (1, 2)))(x, bf_mask) for x in data_split]
                l = compute(*bf_stem_list, scheduler='threads')
                bf_stem_intensities = np.concatenate(l, 0)
                print('bf_stem_intensities.shape', bf_stem_intensities.shape)
                df_stem_list = [delayed(lambda x, y: np.sum(x * y, (1, 2)))(x, df_mask) for x in data_split]
                l = compute(*df_stem_list, scheduler='threads')
                df_stem_intensities = np.concatenate(l, 0)
                print('df_stem_intensities.shape', bf_stem_intensities.shape)
                # intensities = np.sum(self.data * beam_mask_aperture, (1, 2))

                if self.do_plot:
                        num = np.linspace(0, len(bf_stem_intensities) - 1, len(bf_stem_intensities), endpoint=True)
                        f, a = plt.subplots(figsize=(8, 20))
                        a.scatter(num, bf_stem_intensities, s=1, marker='x')
                        ss = '%s%s_%s_intensities' % (self.save_path, self.name, self.save_suffix)
                        f.savefig(ss + '.png', dpi=600)
                        plt.show()

                if self.binary_mask_file is None:
                        BF_STEM = np.ones((self.stepy, self.stepx)).astype(np.float32) * np.mean(bf_stem_intensities)
                        BF_STEM.flat[:len(bf_stem_intensities)] = bf_stem_intensities.flat

                        DF_STEM = np.ones((self.stepy, self.stepx)).astype(np.float32) * np.mean(df_stem_intensities)
                        DF_STEM.flat[:len(df_stem_intensities)] = df_stem_intensities.flat
                else:
                        from scipy.ndimage.filters import gaussian_filter

                        ind = np.linspace(0, s[0], endpoint=False, num=s[0]).astype(np.int)

                        indices = np.zeros((self.stepy, self.stepx)).astype(np.int)
```

```
                        indices[self.bin_mask_positions] = ind
                        # io.plot(indices,'indices')
                        BF_STEM = np.zeros((self.stepy, self.stepx)).astype(np.float32)
                        BF_STEM[:] = np.mean(bf_stem_intensities)
                        BF_STEM[self.bin_mask_positions] = bf_stem_intensities

                        if self.blur_stem > 0:
                                BF_STEM = gaussian_filter(BF_STEM, sigma=self.blur_stem)

                        DF_STEM = np.zeros((self.stepy, self.stepx)).astype(np.float32)
                        DF_STEM[:] = np.mean(df_stem_intensities)
                        DF_STEM[self.bin_mask_positions] = df_stem_intensities
                        if self.blur_stem > 0:
                                DF_STEM = gaussian_filter(DF_STEM, sigma=self.blur_stem)

                unit = BF_STEM.shape[0] // 10 * self.stepsize
                sc = (BF_STEM.shape[0] // 10, '{}m'.format(si_format(unit, precision=2)))

                io.plot(BF_STEM, 'BF-STEM', savePath='%s%s_%s_BF-STEM' % (self.save_path, self.name, self.save_suffix),
                                show=self.do_plot, scale=sc)
                io.plot(DF_STEM, 'DF-STEM', savePath='%s%s_%s_DF-STEM' % (self.save_path, self.name, self.save_suffix),
                                show=self.do_plot, scale=sc)

        def determine_center_rotation_alpha(self):
                if self.metadata_file is None:
                        print('Determine center, alpha, and rotation angle ...')

                        r = self.data.shape[1] / 2 * 0.8

                        action_sequence = [
                                ('Please match the radius of the diffraction disc CONTROL',\
                                 'control', 'r', self.radius),
                                ('Please match the outer rim radius of the aperture CONTROL',\
                                 'control', 'r', self.radius_aperture),
                                ('Please match the inner rim radius of the aperture CONTROL',\
                                 'control', 'r',
                                 self.radius_aperture_inner),
                                ('Now determine the center of the disc with your cursor ENTER',\
                                 'enter', 'pos', self.c1),
                                ('Closing', 'close', 'pos', self.pos2)
                        ]
                        show_it = self.data[[0]]
                        show_it *= self.hot_pixel_mask[0]
                        show_it = np.clip(show_it, 0, 5)
                        cursor = u.InteractiveDataPrep(show_it, r, action_sequence)

                        action_sequence = [
                                (
                                        'Now determine the center again. ENTER', 'enter', 'pos', self.c2),
                                ('Closing', 'close', 'pos', self.pos2)
                        ]
                        show_it = self.data[[self.stepx - 1]]
                        show_it *= self.hot_pixel_mask[0]
                        show_it = np.clip(show_it, 0, 5)
                        cursor = u.InteractiveDataPrep(show_it, self.radius, action_sequence)

                        action_sequence = [
                                (
                                        'Now determine the center again. ENTER', 'enter', 'pos', self.c3),
                                ('Closing', 'close', 'pos', self.pos2)
                        ]
                        show_it = self.data[[(self.stepy - 1) * self.stepx]]
                        show_it *= self.hot_pixel_mask[0]
                        show_it = np.clip(show_it, 0, 5)
                        cursor = u.InteractiveDataPrep(show_it, self.radius, action_sequence)
                else:
                        print('Loading centers and radius from metadata file %s' % self.metadata_file)
                        bin = rw.h5read(self.metadata_file, 'binning_factor').values()[0]
                        self.radius = rw.h5read(self.metadata_file, 'r').values()[0] * bin
                        self.radius_aperture = rw.h5read(self.metadata_file, 'r_aperture').values()[0] * bin
                        self.radius_aperture_inner = \
                        rw.h5read(self.metadata_file, 'r_aperture_inner').values()[0] * bin

                print('r= {}'.format(self.radius))
                print('r_aperture = {}'.format(self.radius_aperture))
                print('r_inner= {}'.format(self.radius_aperture_inner))

        def crop_data(self):
                M = self.M
                M2 = self.M2
                s = self.data.shape
                ds = (s[0], M, M)
```

```

                def crop_data1(d, c, corr_fac, ds):
                        cropped_data = np.zeros((d.shape[0], M, M), dtype=np.float32)
                        for i in range(d.shape[0]):
                                c0s = c[i, 0] - M2 if (c[i, 0] - M2) > 0 else 0
                                c1s = c[i, 1] - M2 if (c[i, 1] - M2) > 0 else 0
                                c0e = c[i, 0] + M2 if (c[i, 0] + M2) < s[1] else s[1]
                                c1e = c[i, 1] + M2 if (c[i, 1] + M2) < s[2] else s[2]

                                c0size0 = M2 if (c[i, 0] - M2) > 0 else c[i, 0]
                                c1size0 = M2 if (c[i, 1] - M2) > 0 else c[i, 1]
                                c0size1 = M2 if (c[i, 0] + M2) < s[1] else s[1] - c[i, 0]
                                c1size1 = M2 if (c[i, 1] + M2) < s[2] else s[2] - c[i, 1]

                                cropped_correction_factor = corr_fac[i, c0s:c0e, c1s:c1e]
                                crop = d[i, c0s:c0e, c1s:c1e]

                                cropped_data[i, ds[1] / 2 - c0size0:ds[1] / 2 + c0size1,
                                ds[2] / 2 - c1size0:ds[2] / 2 + c1size1] =\
                                 crop.astype(np.float32) * cropped_correction_factor

                        return cropped_data

                print('Cropping data ...')
                data_split = np.array_split(self.data, self.cpu_count, 0)
                c_split = np.array_split(self.c.astype(np.int), self.cpu_count, 0)
                bc_corrfac = np.broadcast_to(self.correction_factor[np.newaxis, ...], self.data.shape)
                bc_corrfac_split = np.array_split(bc_corrfac, self.cpu_count, 0)
                crop_data_compute_list = [delayed(crop_data1)(d, c, corr_fac, ds) for d, c, corr_fac in
                                                                    zip(data_split, c_split, bc_corrfac_split)]
                cropped_data = compute(*crop_data_compute_list, scheduler='threads')

                self.correction_factor = None
                self.data = cropped_data

        def get_cropped_valid_mask(self):
                if self.mask_from_varmean:
                        print('Taking valid mask from var and mean of data')
                        v = np.var(self.data, 0)
                        m = np.mean(self.data, 0)
                        vm = v / m
                        io.plot(vm, 'var/mean')
                        mask = np.logical_and(vm > 1 - self.varmean_tol, vm < 1 + self.varmean_tol)
                        io.plot(mask.astype(np.float32),

                        self.valid_mask = np.broadcast_to(mask, self.data.shape)
                        self.valid_mask = np.array_split(self.valid_mask, self.cpu_count, 0)
                else:
                        print('Taking valid mask from hot pixel mask')
                        M = self.M
                        M2 = self.M2
                        s = self.hot_pixel_mask.shape
                        ds = (s[0], M, M)

                        def crop_mask(vm, c, ds):
                                cvm = np.zeros((vm.shape[0], M, M), dtype=np.int8)
                                for i in range(vm.shape[0]):
                                        c0s = c[i, 0] - M2 if (c[i, 0] - M2) > 0 else 0
                                        c1s = c[i, 1] - M2 if (c[i, 1] - M2) > 0 else 0
                                        c0e = c[i, 0] + M2 if (c[i, 0] + M2) < s[1] else s[1]
                                        c1e = c[i, 1] + M2 if (c[i, 1] + M2) < s[2] else s[2]

                                        c0size0 = M2 if (c[i, 0] - M2) > 0 else c[i, 0]
                                        c1size0 = M2 if (c[i, 1] - M2) > 0 else c[i, 1]
                                        c0size1 = M2 if (c[i, 0] + M2) < s[1] else s[1] - c[i, 0]
                                        c1size1 = M2 if (c[i, 1] + M2) < s[2] else s[2] - c[i, 1]

                                        crop = vm[i, c0s:c0e, c1s:c1e]
                                        cvm[i, ds[1] / 2 - c0size0:ds[1] / 2 + c0size1,
                                        ds[2] / 2 - c1size0:ds[2] / 2 + c1size1] = crop

                                return cvm

                        print('Cropping mask ...')
                        hot_pixel_mask_split = np.array_split(self.hot_pixel_mask, self.cpu_count, 0)
                        gap_mask_split = np.array_split(self.gap_mask, self.cpu_count, 0)
                        c_split = np.array_split(self.c.astype(np.int), self.cpu_count, 0)
                        crop_mask_compute_list = [delayed(crop_mask)(d, c, ds) for d, c in
                                                                            zip(hot_pixel_mask_split, c_split)]
                        cropped_valid_mask = compute(*crop_mask_compute_list, scheduler='threads')

                        crop_gap_mask_compute_list = [delayed(crop_mask)(d, c, ds) for d, c in
                                                                                    zip(gap_mask_split, c_split)]
```

```
                        cropped_gap_mask = compute(*crop_gap_mask_compute_list, scheduler='threads')
                        self.valid_mask = cropped_valid_mask
                        self.gap_mask = cropped_gap_mask

        def bin_data(self):
                if self.binning_factor > 0:
                        print('Binning data by %d ...' % self.binning_factor)

                        def mul_rebin(x, y):
                                d = x * y
                                ret = u.rebin(d, (1, self.binning_factor, self.binning_factor), mode='sum')
                                return ret

                        data_split = self.data
                        vm_split = self.valid_mask
                        binned_data_compute_list = [delayed(mul_rebin)(*z) for
                                                                                z in zip(data_split, vm_split)]
                        res = compute(*binned_data_compute_list, scheduler='threads')
                        self.data = res
                        if self.do_plot:
                                io.plot(self.data[0][0], 'scaled binned data')

        def bin_mask(self):
                if self.binning_factor > 0:
                        print('Binning mask by %d ...' % self.binning_factor)

                        def q(x):
                                ret = u.rebin(x, (1, self.binning_factor, self.binning_factor), mode='sum') / (
                                        self.binning_factor * self.binning_factor)
                                return ret

                        vm_split = self.valid_mask
                        valid_mask_rebin_compute_list = [delayed(q)(x.astype(np.float32)) for x in vm_split]
                        self.valid_mask = compute(*valid_mask_rebin_compute_list, scheduler='threads')

                        gm_split = self.gap_mask
                        gap_mask_rebin_compute_list = [delayed(q)(x.astype(np.float32)) for x in gm_split]
                        self.gap_mask = compute(*gap_mask_rebin_compute_list, scheduler='threads')
                        if self.do_plot:
                                io.plot(self.valid_mask[0][0], 'valid mask 0 after binning',\
                                 savePath=self.save_path + 'binned_mask')
                                io.plot(self.gap_mask[0][0], 'gap mask 0 after binning',\
                                 savePath=self.save_path + 'binned_mask')

        def define_rebinned_mask(self):
                if self.binning_factor > 0:
                        def q1(x, fraction):
                                ret = (x >= fraction).astype(np.float32)
                                return ret

                        valid_mask_rebin_compute_list = \
                        [delayed(q1)(x, self.min_fraction_valid) for x in self.valid_mask]
                        self.valid_mask = compute(*valid_mask_rebin_compute_list, scheduler='threads')

                        gap_mask_rebin_compute_list = \
                        [delayed(q1)(x, self.min_fraction_valid) for x in self.gap_mask]
                        self.gap_mask = compute(*gap_mask_rebin_compute_list, scheduler='threads')

                        # valid_mask_compute_list = \
                        [delayed(lambda x, y: x*y)(vm,gm) for vm,gm in zip(self.valid_mask,self.gap_mask)]
                        # self.valid_mask = np.vstack(compute(*valid_mask_compute_list, scheduler='threads'))
                        self.valid_mask = np.vstack(self.valid_mask)

                        if self.do_plot:
                                io.plot(self.valid_mask[0], 'scaled binned mask')
                        print('valid_mask.shape ', self.valid_mask.shape)

        def correct_mask_scaling(self):
                if self.binning_factor > 0:
                        print('Binning data by %d ...' % self.binning_factor)

                        def mul_rebin(x, m):
                                x[m > 0] /= m[m > 0]
                                return x

                        binned_data_compute_list = [delayed(mul_rebin)(d.astype(np.float32), v.astype(np.float32)) for
                                                                                d, v in zip(self.data, self.valid_mask)]
                        self.data = np.vstack(compute(*binned_data_compute_list, scheduler='threads'))
                        print('cropped_data.shape ', self.data.shape)

        def generate_valid_mask_nonzero_intensity(self):
                data_nonzero_mask = self.data > 0
                self.bvm = self.valid_mask
                valid_mask_nonzero_intensity = np.logical_and(self.bvm, data_nonzero_mask)
```

```
                return valid_mask_nonzero_intensity

        def generate_valid_mask_beam_valid(self):
                beam_mask_aperture = u.sector_mask((self.M / self.binning_factor, self.M / self.binning_factor),
                                     (self.M2 / self.binning_factor, self.M2 / self.binning_factor),
                                     self.radius_aperture_inner / self.binning_factor, (0, 360))
                valid_mask_beam_valid = self.valid_mask.copy()
                self.bmb = np.broadcast_to(beam_mask_aperture[np.newaxis, ...], valid_mask_beam_valid.shape)
                valid_mask_beam_valid[self.bmb] = 1
                return valid_mask_beam_valid

        def maybe_interpolate_dead_pixels(self):
                not_valid_and_inside_brightfield = np.logical_and(np.logical_not(self.valid_mask), self.bmb)
                if self.interpolate_dead_pixels:
                        print('Interpolating dead pixels...')
                        kernel = Gaussian2DKernel(1)

                        self.data[not_valid_and_inside_brightfield] = np.NaN
                        # p = Pool(multiprocessing.cpu_count())
                        # p.map(replace_nans, data)
                        for i, data in enumerate(self.data):
                                self.data[i] = interpolate_replace_nans(data.copy(), kernel)

                        self.data = np.nan_to_num(self.data, copy=False)
                else:
                        self.data[not_valid_and_inside_brightfield] = 0

        def determine_positions(self):
                print('Creating position array ...')
                print('stepsize ', self.stepsize)
                print('dx ', self.dx)
                if self.experiment_geometry.pixel_stepx is None and self.experiment_geometry.pixel_stepy is None:
                        pixel_step_x = self.stepsize / self.dx
                        pixel_step_y = self.stepsize / self.dx
                        self.pixel_step_x = pixel_step_x
                        self.pixel_step_y = pixel_step_y
                else:
                        self.pixel_step_x = self.experiment_geometry.pixel_stepx
                        self.pixel_step_y = self.experiment_geometry.pixel_stepy

                print('pixel_step_x :', self.pixel_step_x)
                print('pixel_step_y :', self.pixel_step_y)
                s = self.data.shape
                if self.bin_mask_positions is None:
                        print('Creating raster position array ...')
                        pos = u.advanced_raster_scan(ny=self.stepy, nx=self.stepx, \
                            fast_axis=self.fast_axis, mirror=self.mirror,
                                     theta=self.theta,
                                     dy=self.pixel_step_y, dx=self.pixel_step_x)
                        pos1 = u.advanced_raster_scan(ny=self.stepy, nx=self.stepx, \
                            fast_axis=self.fast_axis, mirror=self.mirror,
                                     theta=self.theta + 2,
                                     dy=self.pixel_step_y, dx=self.pixel_step_x)
                        pos2 = u.advanced_raster_scan(ny=self.stepy, nx=self.stepx, \
                            fast_axis=self.fast_axis, mirror=self.mirror,
                                     theta=self.theta - 2,
                                     dy=self.pixel_step_y, dx=self.pixel_step_x)
                        pos3 = u.advanced_raster_scan(ny=self.stepy, nx=self.stepx, \
                            fast_axis=self.fast_axis, mirror=self.mirror,
                            theta=self.theta + 4,
                            dy=self.pixel_step_y, dx=self.pixel_step_x)
                        pos4 = u.advanced_raster_scan(ny=self.stepy, nx=self.stepx, \
                            fast_axis=self.fast_axis, mirror=self.mirror,
                            theta=self.theta - 4,
                            dy=self.pixel_step_y, dx=self.pixel_step_x)
                else:
                        print('Creating position array from position mask...')
                        X, Y = np.mgrid[0:self.stepx, 0:self.stepy]
                        X = X.astype(np.float32)
                        Y = Y.astype(np.float32)
                        X *= self.pixel_step_x
                        Y *= self.pixel_step_y
                        x_pos = X[self.bin_mask_positions]
                        y_pos = Y[self.bin_mask_positions]
                        pos = np.zeros((s[0], 2))
                        pos[:, 0] = y_pos
                        pos[:, 1] = x_pos

                        mins = np.array([pos[:, 0].min(), pos[:, 1].min()])
                        maxs = np.array([pos[:, 0].max(), pos[:, 1].max()])

                        center = mins + (maxs - mins) / 2.0
```

```
                        pos -= center

                        theta_rad = self.theta / 180.0 * np.pi
                        R = np.array([[np.cos(theta_rad), -np.sin(theta_rad)],
                                                    [np.sin(theta_rad), np.cos(theta_rad)]])
                        # rotate counterclockwise by theta
                        pos = pos.dot(R)

                        pos1 = pos
                        pos2 = pos
                        pos3 = pos
                        pos4 = pos

                for ind in self.exclude_indices:
                        pos = np.delete(pos, ind, 0)
                        pos1 = np.delete(pos1, ind, 0)
                        pos2 = np.delete(pos2, ind, 0)
                        pos3 = np.delete(pos3, ind, 0)
                        pos4 = np.delete(pos4, ind, 0)

                if self.do_plot:
                        io.scatter_positions2(pos, show=self.do_plot, savePath='%s_pos' % self.name)

                return pos, pos1, pos2, pos3, pos4

        def prepare_initial_probe(self):
                E = self.E_eV
                N = self.M / self.binning_factor
                defocus_nm = self.df * 1e9
                det_pix = self.dpix
                alpha_rad = self.alpha_diff
                dx_angstrom = self.dx * 1e10

                print('Preparing initial probe ...')
                print('defocus_nm:', defocus_nm)
                print('dx_angstrom :', dx_angstrom)
                print('alpha_rad :', alpha_rad)
                print('defocus_nm:', defocus_nm)
                print('det_pix :', det_pix)

                probes = []
                fourier_probes = []

                r, i, fr, fi = probe.focused_probe(E, N, d=dx_angstrom,\
                 ^^Ialpha_rad=alpha_rad, defocus_nm=defocus_nm, det_pix=det_pix,\
                 ^^I C3_um=2.2, C5_mm=0, tx=0, ty=0, Nedge=2, plot=False)
                pr = (r + 1j * i).astype(np.complex128)
                fpr = ifft2(fftshift(pr), norm='ortho')

                probes.append(pr)
                fourier_probes.append(fpr)

                for k in range(5):
                        df = (defocus_nm + (k + 1) * 100)
                        r, i, fr, fi = probe.focused_probe(E, N, d=dx_angstrom, alpha_rad=alpha_rad, defocus_nm=df,
^^I                        det_pix=det_pix, C3_um=2.2, C5_mm=0, tx=0, ty=0, Nedge=2, plot=False)
                        pr = (r + 1j * i).astype(np.complex128)
                        fpr = ifft2(fftshift(pr), norm='ortho')

                        probes.append(pr)
                        fourier_probes.append(fpr)

                        df = (defocus_nm - (k + 1) * 100)
                        r, i, fr, fi = probe.focused_probe(E, N, d=dx_angstrom, alpha_rad=alpha_rad, defocus_nm=df,
                            det_pix=det_pix, C3_um=2.2, C5_mm=0, tx=0, ty=0, Nedge=2, plot=False)
                        pr = (r + 1j * i).astype(np.complex128)
                        fpr = ifft2(fftshift(pr), norm='ortho')

                        probes.append(pr)
                        fourier_probes.append(fpr)
                if self.do_plot:
                        io.plotAbsAngle(probes[0], 'probe real space')
                        io.plotAbsAngle(fourier_probes[0], 'probe aperture space')

                return np.array(probes), np.array(fourier_probes)

        def prepare_hdf5_dict(self):
                ret = u.Param()

                ret.mask = fftshift(self.valid_mask.astype(np.float32), (1, 2))
                ret.mask_beam_valid = fftshift(self.valid_mask_beam_valid.astype(np.float32), (1, 2))
                ret.data = fftshift(self.data, (1, 2))
                ret.alpha = self.alpha
                ret.alpha_diff = self.alpha_diff
```

```
                ret.z = self.z
                ret.E = self.E_eV
                ret.dpix = self.dpix
                ret.dx = self.dx
                ret.theta = 0
                ret.I_beam = self.beam_intensity
                ret.r_aperture = self.radius_aperture / self.binning_factor
                ret.r_aperture_inner = self.radius_aperture_inner / self.binning_factor
                ret.r = self.radius / self.binning_factor
                ret.centers = self.c
                ret.centers_residual = self.c_residual
                ret.stepsize = self.stepsize
                ret.stepx = self.stepx
                ret.stepy = self.stepy
                ret.pixel_step_y = self.pixel_step_y
                ret.pixel_step_x = self.pixel_step_x
                ret.pos = self.pos
                ret.pos1 = self.pos1
                ret.pos2 = self.pos2
                ret.pos3 = self.pos3
                ret.pos4 = self.pos4
                ret.probe = self.pr.astype(np.complex64)
                ret.probe_fourier = self.fpr.astype(np.complex64)
                ret.grid_positions = self.grid_positions
                ret.binning_factor = self.binning_factor
                if self.vacuum_measurements is not None:
                        ret.vacuum_mean = self.vacuum_mean

                return ret

        def prepare_mat_dict(self):
                ret = u.Param()

                ret.mask = self.valid_mask.astype(np.float32)
                ret.mask_beam_valid = self.valid_mask_beam_valid.astype(np.float32)
                ret.data = self.data, (1, 2)
                #data = None
                ret.alpha = self.alpha
                ret.alpha_diff = self.alpha_diff
                ret.z = self.z
                ret.E = self.E_eV
                ret.dpix = self.dpix
                ret.dx = self.dx
                ret.theta = 0
                ret.I_beam = self.beam_intensity
                ret.r_aperture = self.radius_aperture / self.binning_factor
                ret.r_aperture_inner = self.radius_aperture_inner / self.binning_factor
                ret.r = self.radius / self.binning_factor
                ret.centers = self.c
                ret.centers_residual = self.c_residual
                ret.stepsize = self.stepsize
                ret.stepx = self.stepx
                ret.stepy = self.stepy
                ret.pixel_step_y = self.pixel_step_y
                ret.pixel_step_x = self.pixel_step_x
                ret.pos = self.pos
                ret.pos1 = self.pos1
                ret.pos2 = self.pos2
                ret.pos3 = self.pos3
                ret.pos4 = self.pos4
                ret.probe_real = self.pr.real.astype(np.float32)
                ret.probe_imag = self.pr.imag.astype(np.float32)
                ret.probe_fourier_real = self.fpr.real.astype(np.float32)
                ret.probe_fourier_imag = self.fpr.imag.astype(np.float32)
                ret.grid_positions = self.grid_positions
                ret.binning_factor = self.binning_factor
                if self.vacuum_measurements is not None:
                        ret.vacuum_mean = self.vacuum_mean
                return ret

        def determine_dp_centers(self):
                if self.metadata_file is None:
                        if self.dp_centering_method == 'linear':
                                ctr_0 = np.array([self.c1[1], self.c1[2]], dtype=np.float32)
                                ctr_end_col = np.array([self.c2[1], self.c2[2]], dtype=np.float32)
                                ctr_end_row = np.array([self.c3[1], self.c3[2]], dtype=np.float32)
                                dp_shift_per_column = (ctr_end_col - ctr_0) / (self.stepx - 1)
                                dp_shift_per_row = (ctr_end_row - ctr_0) / (self.stepy - 1)
                                print('ctr_0', ctr_0)
                                print('ctr_end_col', ctr_end_col)
                                print('ctr_end_row', ctr_end_row)
                                print('dp_shift_per_column', dp_shift_per_column)
```

```python
                print('dp_shift_per_row ', dp_shift_per_row)

                ctr = np.zeros(((self.stepy * self.stepx), 2))
                ctr_res = np.zeros(((self.stepy * self.stepx), 2))

                for y in range(self.stepy):
                    for x in range(self.stepx):
                        ctr[y * self.stepx + x] =\
                         np.around(ctr_0 + x * dp_shift_per_column + y * dp_shift_per_row)
                        ctr_res[y * self.stepx + x] = (ctr_0 + x * dp_shift_per_column +\
                         y * dp_shift_per_row) - ctr[
                                y * self.stepx + x]

                # fx = interp1d([c1[0], c2[0]], [self.c1[1], self.c2[1]],
                # fill_value='extrapolate')
                # fy = interp1d([c1[1], c2[1]], [self.c1[2], self.c2[2]],
                # fill_value='extrapolate')
                #
                # # x = np.linspace(self.c1[1], self.c2[1], endpoint=True, num=self.stepx)
                # # y = np.linspace(self.c1[2], self.c2[2], endpoint=True, num=self.stepy)
                # x = fx(np.arange(self.stepx))
                # y = fy(np.arange(self.stepy))
                # xr = np.round(x)
                # yr = np.round(y)
                # cxx_int, cyy_int = np.meshgrid(xr, yr)
                # cxx, cyy = np.meshgrid(x, y)
                # cyy_residual = cyy - cyy_int
                # cxx_residual = cxx - cxx_int
                #
                # # io.plot(cxx_int,'cxx_int')
                # # io.plot(cyy_int, 'cyy_int')
                #
                # cy = cyy_int[self.bin_mask_positions]
                # cx = cxx_int[self.bin_mask_positions]
                #
                # cy_residual = cyy_residual[self.bin_mask_positions]
                # cx_residual = cxx_residual[self.bin_mask_positions]

                print('centers', ctr)

                self.c = ctr
                self.c_residual = ctr_res
                self.grid_positions = np.stack([self.xpos, self.ypos], -1)
            elif self.dp_centering_method == 'registration':
                pass
        else:
            self.c = rw.h5read(self.metadata_file, 'centers').values()[0]
            self.c_residual = rw.h5read(self.metadata_file, 'centers_residual').values()[0]
            self.grid_positions = rw.h5read(self.metadata_file, 'grid_positions').values()[0]

    def set_geometry_parameters(self):
        if self.experiment_geometry_entry == 'auto':
            print('Loading experiment geometry from metadata...')
            json_filename = self.path + self.name + '.json'
            json_dict = json.load(open(json_filename))
            post_magnification = 1.58
            z = json_dict['Projection']['CameraLength']
            if z == 1.0:
                z = 1.005
            elif z == 0.73:
                z = 0.707
            elif z == 0.52:
                z = 0.509
            self.z = z * post_magnification
            self.E_eV = json_dict['Gun']['HTValue']
            self.lam = u.lam(self.E_eV)
            self.dpix = 55e-6

            self.stepy = json_dict['Scanning']['Parameters']['Frame (Y)']['ROI len']
            self.stepx = json_dict['Scanning']['Parameters']['Line (X)']['ROI len']
            self.pointsx = json_dict['Scanning']['Parameters']['Line (X)']['Pts']
            self.pointsy = json_dict['Scanning']['Parameters']['Line (X)']['Pts']
            self.stepsize = json_dict['Illumination']['STEMSize'] / self.pointsy * 1e-9
            self.df = json_dict['Projection']['Defocus']
        else:
            print('Manual experiment geometry from metadata...')
            if self.experiment_geometry.alpha_diff is not None:
                self.alpha_diff = self.experiment_geometry.alpha_diff
            else:
                self.z = self.experiment_geometry.z
            self.E_eV = self.experiment_geometry.E_eV
            self.lam = u.lam(self.E_eV)
            self.dpix = self.experiment_geometry.dpix

```

```
            self.stepy = self.experiment_geometry.stepy
            self.stepx = self.experiment_geometry.stepx
            self.stepsize = self.experiment_geometry.stepsize
            self.df = self.experiment_geometry.df

        if not self.defocus_auto:
            self.df = self.experiment_geometry.df

        self.dpix *= self.binning_factor

    def print_timestamp(self):
        ts = time.time()
        st = datetime.datetime.fromtimestamp(ts).strftime('%Y-%m-%d %H:%M:%S')
        print(st)

    def prepare_dataset(self):
        r"""Prepares data for reconstruction

        Args:
            path (string): path to the data file
            name (string): name of the h5 file and the json file
            mask_file (string): path and name of the hot pixel mask
            step_size (float): real space step size
            q_max_rel (float): maximum scattering angle relative to\
             diffraction limit angle (default: 1.1)
        """

        h5_filename = self.path + self.name + self.file_extension

        self.print_timestamp()
        self.set_geometry_parameters()

        print('Loading data from file %s' % h5_filename)
        f = h5py.File(h5_filename, 'r')
        # self.data = rw.h5read(h5_filename, self.data_entry).values()[0]

        d0 = f[self.data_entry]
        d0s = np.array(d0.shape)
        d0s[0] = d0s[0] // 20
        print('d0s,', tuple(d0s))
        self.data = da.from_array(d0, chunks=tuple(d0s))
        s = np.array(self.data.shape)
        print('data type', self.data.dtype)
        self.print_timestamp()
        print('initial dataset size = ', s)
        print('Data loaded.')
        self.bin_mask_positions = self.load_binary_position_mask()

        if self.manual_data_selection:
            dsum = da.sum(self.data[100:200], 0).compute()

            smallest_side = np.min(s[1:] // 2)
            print(smallest_side)
            cm = ni.center_of_mass(dsum)
            self.com = com = np.array(cm).astype(np.int)
            self.rr = rr = np.min(np.array([com[0], com[1],\
             s[1] - com[0], s[2] - com[1], smallest_side]))
            print('com,radius = ', com, rr)

            dcrop = self.data[:, com[0] - rr:com[0] + rr, com[1] - rr:com[1] + rr].compute()
            self.data = dcrop
            dcrop1 = da.from_array(dcrop, chunks=dcrop.shape)
            dcsum = da.sum(dcrop1, (1, 2)).compute()

            def get_com(imgs):
                ret = np.ones((imgs.shape[0]))
                for i, dd in enumerate(imgs):
                    comx1, comy1 = ni.center_of_mass(dd)
                    ret[i] = comy1
                return ret

            dcrop_split = np.array_split(dcrop, self.cpu_count, 0)
            com_compute_list = [delayed(get_com)(d) for d in dcrop_split]
            comy = np.hstack(compute(*com_compute_list, scheduler='threads'))
            print('comy.shape ', comy.shape)
            global f
            f, a = plt.subplots(figsize=(20, 8))
            a.scatter(np.arange(len(comy)), comy, s=1)

            idx = np.array([0, 0])

            def onclick(event):
                global f
```

```
                                # print(event.button)
                                if event.button == 3:
                                        ix, iy = event.xdata, event.ydata

                                        idx[0] = ix

                                        f.canvas.mpl_disconnect(cid)
                                        plt.close(f)

                        cid = f.canvas.mpl_connect('button_press_event', onclick)

                        plt.show()
                        idx[1] = idx[0] + (self.stepx * self.stepy)
                        print('start, end = ', idx)

                        self.data = self.data[idx[0]:idx[1], ...]
                        dcsum = dcsum[idx[0]:idx[1]]
                        dcsum1 = dcsum.reshape((self.stepy, self.stepx))

                        s = np.array(self.data.shape)
                        print('loaded dataset size = ', s)
                        x = u.MaskPrep(dcsum1, np.ones_like(dcsum1))
                        self.bin_mask_positions = x.current_mask.astype(np.bool)
                        if self.do_plot:
                                io.plot(self.bin_mask_positions.astype(np.int), 'valid positions')
                else:
                        self.data = self.data.compute()

                if self.select_area:
                        size = self.selected_area_size
                        print('Selecting an area of size %d x %d ...' % (size, size))
                        st = self.selected_area_start
                        print('reshape to ', (self.stepy, self.stepx, s[1], s[2]))
                        # d1 = np.reshape(self.data, (self.stepy, self.stepx, s[1], s[2]))
                        d1 = self.data.reshape((self.stepy, self.stepx, s[1], s[2]))

                        self.data = d1[st[0]:st[0] + size, st[1]:st[1] + size, ...]
                        self.bin_mask_positions = self.bin_mask_positions[st[0]:st[0] + size, st[1]:st[1] + size]

                        ds = self.data.shape
                        self.data = self.data.reshape((ds[0] * ds[1], ds[2], ds[3]))
                        s = np.array(self.data.shape)
                        print('New data shape after selecting area: ', s)
                        self.stepx = self.stepy = size

                x = np.linspace(0, self.stepx, endpoint=False, num=self.stepx).astype(np.int)
                y = np.linspace(0, self.stepy, endpoint=False, num=self.stepy).astype(np.int)
                yy, xx = np.meshgrid(x, y)
                self.xpos = xx[self.bin_mask_positions]
                self.ypos = yy[self.bin_mask_positions]

                bmflat = self.bin_mask_positions.flatten()
                self.data = self.data[bmflat]
                self.bin_mask_positions_flat = bmflat

                s = np.array(self.data.shape)

                print('dataset size after excluding indices = ', s)
                self.hot_pixel_mask = self.load_hot_pixel_mask()
                self.gap_mask = self.load_gap_mask()

                self.determine_center_rotation_alpha()

                self.M_diff = int(self.radius * 2)

                if self.data_size is None:
                        self.M = int(self.q_max_rel * self.radius * 2)
                else:
                        self.M = self.data_size

                self.M = self.M if self.M % (self.binning_factor * 2) == 0 else \
                    self.M - (self.M % (self.binning_factor * 2))
                self.M2 = self.M / 2

                print(' M = {}'.format(self.M))
                print('after considering binning: M = {}'.format(self.M))

                if self.experiment_geometry.alpha_diff is not None:
                        self.z = (self.radius * self.dpix /\
                         self.binning_factor / np.tan(self.alpha_diff))[0]
                        self.alpha = np.arctan(self.M / self.binning_factor / 2 * self.dpix / self.z)
                else:
                        self.alpha_diff = np.arctan(self.M_diff\
                         / self.binning_factor / 2 * self.dpix / self.z)
                        self.alpha =\
```

```
                         np.arctan(self.M / self.binning_factor / 2 * self.dpix / self.z)

                self.dx = u.real_space_resolution(self.E_eV, self.z,\
                 self.dpix, self.M / self.binning_factor)
                self.dx_diff = u.real_space_resolution(self.E_eV,\
                 self.z, self.dpix, self.M_diff / self.binning_factor)

                self.pr, self.fpr = self.prepare_initial_probe()

                print('z= {}m'.format(si_format(self.z)))
                print('E= {}eV'.format(si_format(self.E_eV)))
                print('lam= {}m'.format(si_format(self.lam, precision=2)))
                print('det_pix= {}m'.format(si_format(self.dpix, precision=2)))
                print('dx = {}m'.format(si_format(self.dx, precision=2)))
                print('dx BF limit= {}m'.format(si_format(self.dx_diff, precision=2)))
                print('alpha= {}rad'.format(si_format(self.alpha, precision=2)))
                print('alpha BF limit = {}rad'.format(si_format(self.alpha_diff, precision=2)))

                self.determine_dp_centers()

                self.correction_factor = self.load_correction_factor(s)

                self.get_cropped_valid_mask()

                self.crop_data()
                self.bin_data()

                self.bin_mask()

                self.correct_mask_scaling()
                self.define_rebinned_mask()

                if self.do_plot:
                        print(self.valid_mask.shape)
                        io.plot(self.valid_mask[0].astype(np.float32), 'valid_mask[0]')

                self.prepare_stem_image()

                # self.valid_mask_nonzero_intensity = self.generate_valid_mask_nonzero_intensity()
                self.valid_mask_beam_valid = self.generate_valid_mask_beam_valid()

                # io.plot(valid_mask * data[0], 'test cropped valid mask 1')
                # io.plot(valid_mask_nonzero_intensity[0] * data[0], 'test cropped valid mask 2')

                self.maybe_interpolate_dead_pixels()

                if self.vacuum_measurements is not None:
                        vacuum_data = self.data[self.vacuum_measurements]
                        self.vacuum_mean = np.mean(vacuum_data, 0)
                        vacuum_data = None
                        if self.do_plot:
                                io.plot(self.vacuum_mean, 'vacuum_mean')

                intensities = np.sum(self.data * self.valid_mask, (1, 2))
                max_intensity = intensities.max()
                max_intensity_ind = intensities.argmax()


                print('maximum intensity: %g at index %d' % (max_intensity, max_intensity_ind))

                beam_mask = u.sector_mask((self.M / self.binning_factor, self.M / self.binning_factor),
                             (self.M2 / self.binning_factor, self.M2 / self.binning_factor),
                             self.radius / self.binning_factor, (0, 360))
                # io.plot(beam_mask, 'beam_mask')
                mean_beam_pixel_intensity = np.mean(self.data[max_intensity_ind] * beam_mask * self.valid_mask)
                print('mean_beam_pixel_intensity: %g' % mean_beam_pixel_intensity)

                dead_pixels_in_BF_mask = np.logical_and(np.logical_not(self.valid_mask), beam_mask)
                # io.plot(dead_pixels_in_BF_mask, 'dead_pixels_in_BF_mask')
                dead_pixels_in_BF = np.sum(dead_pixels_in_BF_mask)
                print('dead_pixels_in_BF: %d' % dead_pixels_in_BF)

                self.beam_intensity = np.sum(
                        self.data[max_intensity_ind] * self.valid_mask) + dead_pixels_in_BF * mean_beam_pixel_intensity
                print('beam_intensity: %g' % self.beam_intensity)

                self.pos, self.pos1, self.pos2, self.pos3, self.pos4 = self.determine_positions()P

                for i in range(self.pr.shape[0]):
                        self.fpr[i] /= m.sqrt(norm(self.fpr[i]) ** 2)
                        self.fpr[i] *= m.sqrt(self.beam_intensity)

                        self.pr[i] /= m.sqrt(norm(self.pr[i]) ** 2)
                        self.pr[i] *= m.sqrt(self.beam_intensity)

                if self.save_hdf5:
```

```
                fname = '%s%s_bin%d_%s.h5' % (self.save_path, self.name, self.binning_factor, self.save_suffix)
                print('Saving to hdf5 file %s ...' % fname)
                ret = self.prepare_hdf5_dict()
                rw.h5write(fname, ret)

        if self.save_matlab:
                fname = '%s%s_bin%d_%s' % (self.save_path, self.name, self.binning_factor, self.save_suffix)
                print('Saving to matlab file %s ...' % fname)
                from scipy.io import savemat
                ret = self.prepare_mat_dict()
                savemat(fname, ret, do_compression=True)
        ts = time.time()
        st = datetime.datetime.fromtimestamp(ts).strftime('%Y-%m-%d %H:%M:%S')
        print(st)
        print('Done.')
        return ret
```

6.8 Curriculum vitae

Lebenslauf entfällt aus datenschutzrechtlichen Gründen

6.9 Acronyms

ADF	annular dark field
CDI	coherent diffractive imaging
DM	difference map
cryo-EM	cryo-electron microscopy
CTEM	conventional TEM
CTF	contrast transfer function
DFT	discrete Fourier transform
DQE	detective quantum efficiency
EDX	energy-dispersive X-ray
ePIE	extended ptychographic iterative engine
FIB	focused ion beam
FRC	Fourier Ring Correlation
FZP	Fresnel Zone Plate
GIF	Gatan Imaging Filter
HAADF	high angle annular dark field
IASA	isolated atom superposition approximation
MAP	maximum-a-posteriori
MAPS	Monolithic active pixel sensor
MTF	modulation transfer function
NMSR	Normalized root mean square error
NTF	noise transfer function
PCTF	phase contrast transfer function
SEM	scanning electron microscope
SNR	signal-to-noise ratio
STEM	scanning transmission electron microscope/microscopy

TEM	transmission electron microscope/microscopy
TIE	transport-of-intensity equation
WDD	Wigner Distribution Deconvolution

Bibliography

1. Pauli, W. in *Quantentheorie* (eds Bethe, H., Hund, F., Mott, N. F., Pauli, W., Rubinowicz, A., Wentzel, G. & Smekal, A.) 00491, 83–272 (Springer Berlin Heidelberg, Berlin, Heidelberg, 1933). doi:`10.1007/978-3-642-52619-0_2`.
2. Zernike, F. Phase Contrast, a New Method for the Microscopic Observation of Transparent Objects. *Physica,* 686–698 (1942).
3. Ix, P., Zernike, F., Ii, P., Contrast, P. & Rayleigh, T. Phase Contrast, a New Method for the Microscopic Observation of Transparent Objects Part II. *Physica.* 00000, 686–698 (1942).
4. Danev, R., Buijsse, B., Khoshouei, M., Plitzko, J. M. & Baumeister, W. Volta Potential Phase Plate for In-Focus Phase Contrast Transmission Electron Microscopy. *PNAS* **111.** 00077 PMID: 25331897, 15635–15640 (Apr. 11, 2014).
5. Gabor, D. & Goss, W. P. Interference Microscope with Total Wavefront Reconstruction. *J. Opt. Soc. Am., JOSA* **56.** 00113, 849–858 (July 1, 1966).
6. Gabor, D. *A New Microscopic Principle* 04431. <`https://www.nature.com/articles/161777a0`> (1948).
7. Cowley, J. M. Twenty Forms of Electron Holography. *Ultramicroscopy* **41.** 00165, 335–348 (June 1, 1992).
8. Leith, E. N. & Upatnieks, J. Wavefront Reconstruction with Continuous-Tone Objects*. *J. Opt. Soc. Am., JOSA* **53.** 00000, 1377–1381 (Dec. 1, 1963).
9. Leith, E. N. & Upatnieks, J. Reconstructed Wavefronts and Communication Theory*. *J. Opt. Soc. Am., JOSA* **52.** 00000, 1123–1130 (Oct. 1, 1962).
10. Lubk, A. in *Advances in Imaging and Electron Physics* 00000, 141–229 (Elsevier, Jan. 1, 2018). doi:`10.1016/bs.aiep.2018.05.005`.
11. Hoppe, W. Beugung Im Inhomogenen Primärstrahlwellenfeld. I. Prinzip Einer Phasenmessung von Elektronenbeungungsinterferenzen. *Acta Cryst. A* **25.** 00142, 495–501 (July 2, 1969).
12. Hoppe, W. Beugung im inhomogenen Primärstrahlwellenfeld. III. Amplituden- und Phasenbestimmung bei unperiodischen Objekten. *Acta Cryst A, Acta Cryst Sect A, Acta Crystallogr A, Acta Crystallogr Sect A, Acta Crystallogr A Cryst Phys Diffr Theor Gen Crystallogr, Acta Crystallogr Sect A Cryst Phys Diffr Theor Gen Crystallogr* **25.** 00065, 508–514 (July 2, 1969).

13. Rodenburg, J. M. & Bates, R. H. T. The Theory of Super-Resolution Electron Microscopy Via Wigner-Distribution Deconvolution. *Philos. Trans. R. Soc. A Math. Phys. Eng. Sci.* **339.** 00000, 521–553 (June 1992).
14. Nellist, P. D., McCallum, B. C. & Rodenburg, J. M. Resolution beyond the 'information Limit' in Transmission Electron Microscopy. *Nature.* 00081. doi:10.1038/374630a0 (1995).
15. Chapman, H. N. Phase-Retrieval X-Ray Microscopy by Wigner-Distribution Deconvolution. *Ultramicroscopy* **66.** 00000, 153–172 (Dec. 1996).
16. Bai, X.-c., McMullan, G. & Scheres, S. H. W. How Cryo-EM Is Revolutionizing Structural Biology. *Trends in Biochemical Sciences* **40.** 00152, 49–57 (Jan. 2015).
17. Kühlbrandt, W. Cryo-EM Enters a New Era. *eLife Sciences* **3.** 00064, e03678 (Aug. 13, 2014).
18. Yoshioka, C. Single-Particle Cryo-EM Map @ 1.56Å, Met Close-Up. 00000.
19. Boersch, H. Über Die Kontraste von Atomen Im Elektronenmikroskop. *Zeitschrift für Naturforschung A* **2a.** 00000, 615–633 (1947).
20. Khoshouei, M., Radjainia, M., Baumeister, W. & Danev, R. Cryo-EM Structure of Haemoglobin at 3.2 Å Determined with the Volta Phase Plate. *Nature Communications* **8.** 00044, 16099 (June 30, 2017).
21. Crewe, A. V., Eggenberger, D. N., Wall, J. & Welter, L. M. Electron Gun Using a Field Emission Source. *Review of Scientific Instruments* **39.** 00443, 576–583 (Apr. 1, 1968).
22. Tonomura, A., Matsuda, T., Endo, J., Todokoro, H. & Komoda, T. Development of a Field Emission Electron Microscope. *J Electron Microsc (Tokyo)* **28.** 00215, 1–11 (Jan. 1, 1979).
23. Krivanek, O. L., Nellist, P. D., Dellby, N., Murfitt, M. F. & Szilagyi, Z. Towards Sub-0.5Å Electron Beams. *Ultramicroscopy. Proceedings of the International Workshop on Strategies and Advances in Atomic Level Spectroscopy and Analysis* **96.** 00189, 229–237 (Sept. 1, 2003).
24. Haider, M., Uhlemann, S., Schwan, E., Rose, H., Kabius, B. & Urban, K. Electron Microscopy Image Enhanced. *Nature* **392.** 00955, 768–769 (Apr. 1998).
25. Reimer, L., Fromm, I., Hülk, C. & Rennekamp, R. Energy-Filtering Transmission Electron Microscopy in Materials Science. *Microsc. Microanal. Microstruct.* **3.** 00030, 141–157 (Apr. 1, 1992).
26. Bayou, A. *FEI Tecnai F-20 Operations Manual* 00000. 21:09:05 UTC.

27. Tuan, S. F. & Sakurai, J. J. *Modern Quantum Mechanics* revised edition. 00228. 512 pp. (Prentice Hall, Reading, Mass, Aug. 31, 1993).
28. Kirkland, E. *Advanced Computing in Electron Microscopy* 00000 (2010).
29. Reimer, L. & Kohl, H. *Transmission Electron Microscopy: Physics of Image Formation* 5th ed. 00123 (Springer-Verlag, New York, 2008).
30. Nellist, P., Martinez, G., Pennycook, T., Jones, L., Yang, H., Huth, M., Simson, M., Soltau, H., Kondo, Y., Sagawa, R. & IUCr. *Imaging Charge Transfer in Crystals Using Electron Ptychography* 00000. <`http://scripts.iucr.org/cgi-bin/paper?S2053273317094517`> (2017).
31. Egerton, R. F. Measurement of Inelastic/Elastic Scattering Ratio for Fast Electrons and Its Use in the Study of Radiation Damage. *physica status solidi (a)* **37.** 00044, 663–668 (Oct. 16, 1976).
32. Henderson, R. The Potential and Limitations of Neutrons, Electrons and X-Rays for Atomic Resolution Microscopy of Unstained Biological Molecules. *Q. Rev. Biophys.* **28.** 00581, 171–93 (May 1995).
33. Vulovi , M., Ravelli, R. B. G., van Vliet, L. J., Koster, A. J., Lazi , I., Lücken, U., Rullgård, H., Öktem, O. & Rieger, B. Image Formation Modeling in Cryo-Electron Microscopy. *Journal of Structural Biology* **183.** 00027, 19–32 (July 2013).
34. Baker, L. A. & Rubinstein, J. L. Radiation Damage in Electron Cryomicroscopy. *Meth. Enzymol.* **481.** 00059, 371–388 (2010).
35. G. McMullan, Vinothkumar, K. R. & Henderson, R. Thon Rings from Amorphous Ice and Implications of Beam-Induced Brownian Motion in Single Particle Electron Cryo-Microscopy. *Ultramicroscopy* **158.** 00023, 26–32 (Nov. 1, 2015).
36. Matthies, D., Bartesaghi, A., Merk, A., Banerjee, S. & Subramaniam, S. Residue Specific Radiation Damage of Protein Structures Using High-Resolution Cryo-Electron Microscopy. *Biophysical Journal* **108.** 00000, 190a (Jan. 27, 2015).
37. Leapman, R. D. & Sun, S. Cryo-Electron Energy Loss Spectroscopy: Observations on Vitrified Hydrated Specimens and Radiation Damage. *Ultramicroscopy. Proceedings of the 2nd international workshop on Electron Energy Loss Spectroscopy and Imaging* **59.** 00110, 71–79 (July 1, 1995).
38. Hosten, O., Krishnakumar, R., Engelsen, N. J. & Kasevich, M. A. Quantum Phase Magnification. *Science* **352.** 00012 PMID: 27339982, 1552–1555 (June 24, 2016).

39. Juffmann, T., Klopfer, B. B. & Kasevich, M. A. *Multi-Pass Phase Microscopy* in *Novel Techniques in Microscopy* 00000 (Optical Society of America, 2017), NS1C–5.

40. Juffmann, T., Koppell, S. A., Klopfer, B. B., Ophus, C., Glaeser, R. & Kasevich, M. A. Multi-Pass Transmission Electron Microscopy. 00000 arXiv: 1612.04931. arXiv: `1612.04931 [physics, physics:quant-ph]` (Dec. 15, 2016).

41. Kruit, P., Hobbs, R. G., Kim, C.-S., Yang, Y., Manfrinato, V. R., Hammer, J., Thomas, S., Weber, P., Klopfer, B., Kohstall, C., Juffmann, T., Kasevich, M. A., Hommelhoff, P. & Berggren, K. K. Designs for a Quantum Electron Microscope. *Ultramicroscopy* **164.** 00013, 31–45 (May 2016).

42. Meyer, R. R. & Kirkland, A. I. Characterisation of the Signal and Noise Transfer of CCD Cameras for Electron Detection. *Microsc. Res. Tech.* **49.** 00112, 269–280 (May 1, 2000).

43. McMullan, G., Chen, S., Henderson, R. & Faruqi, A. R. Detective Quantum Efficiency of Electron Area Detectors in Electron Microscopy. *Ultramicroscopy* **109.** 00137, 1126–1143 (Aug. 2009).

44. Koch, C. T. Determination of Core Structure Periodicity and Point Defect Density along Dislocations. *Ph.D. Thesis.* 00232 (Jan. 1, 2002).

45. Yalamanchili, P., Arshad, U., Mohammed, Z., Garigipati, P., Entschev, P., Kloppenborg, B., Malcolm, J. & Melonakos, J. ArrayFire - A High Performance Software Library for Parallel Computing with an Easy-to-Use API. 00029 (2015).

46. O'Boyle, N. M., Banck, M., James, C. A., Morley, C., Vandermeersch, T. & Hutchison, G. R. Open Babel: An Open Chemical Toolbox. *Journal of Cheminformatics* **3.** 02126, 33 (Oct. 7, 2011).

47. Lubk, A. in *Advances in Imaging and Electron Physics* (ed Hawkes, P. W.) 00000, 105–140 (Elsevier, Jan. 1, 2018). doi:`10.1016/bs.aiep.2018.05.004`.

48. Peng, L. M., Dudarev, S. L. & Whelan, M. J. *High Energy Electron Diffraction and Microscopy* 00129. 560 pp. (Oxford University Press, Oxford, New York, Apr. 7, 2011).

49. Dudarev, S. L., Peng, L.-M. & Whelan, M. J. Correlations in Space and Time and Dynamical Diffraction of High-Energy Electrons by Crystals. *Phys. Rev. B* **48.** 00096, 13408–13429 (Nov. 1, 1993).

50. Müller, H. *A Coherence Function Approach to Image Simulation* 00040. phd (Technische Universität, Darmstadt, June 21, 2000).

51. Kohl, H. & Rose, H. in *Advances in Electronics and Electron Physics* (ed Hawkes, P. W.) 00237, 173–227 (Academic Press, 1985).

52. A. Alonso, M. Wigner Functions in Optics: Describing Beams as Ray Bundles and Pulses as Particle Ensembles. *Adv. Opt. Photonics* **3,** 272 (Nov. 2011).

53. Lubk, A. & Röder, F. Phase-Space Foundations of Electron Holography. *Phys. Rev. A* **92.** 00000, 033844 (Sept. 23, 2015).

54. Raymer, M., Beck, M. & McAlister, D. Complex Wave-Field Reconstruction Using Phase-Space Tomography. *Phys. Rev. Lett.* **72,** 1137–1140 (1994).

55. Smithey, D., Beck, M., Raymer, M. & Faridani, A. Measurement of the Wigner Distribution and the Density Matrix of a Light Mode Using Optical Homodyne Tomography: Application to Squeezed States and the Vacuum. *Phys. Rev. Lett.* **70.** 01303, 1244–1247 (Mar. 1993).

56. Band, W. & Park, J. L. A General Method of Empirical State Determination in Quantum Physics: Part II. *Found Phys* **1.** 00000, 339–357 (Dec. 1971).

57. Park, J. L. & Band, W. A General Theory of Empirical State Determination in Quantum Physics: Part I. *Found Phys* **1.** 00063, 211–226 (Sept. 1971).

58. Badde, H. & Reimer, L. Der Einfluß Einer Streuenden Phasenplatte Auf Das Elektronenmikroskopische Bild. *Zeitschrift für Naturforschung A* **25a.** 00000, 760–765 (1970).

59. Willasch, D. High Resolution Electron Microscopy with Phase Plates. *Mikroskopie* **28.** 00000, 364–365 (1973).

60. Glaeser, R. M. Invited Review Article: Methods for Imaging Weak-Phase Objects in Electron Microscopy. *Review of Scientific Instruments* **84.** 00051, 111101 (Nov. 1, 2013).

61. Walter, A., Muzik, H., Vieker, H., Turchanin, A., Beyer, A., Gölzhäuser, A., Lacher, M., Steltenkamp, S., Schmitz, S., Holik, P., Kühlbrandt, W. & Rhinow, D. Practical Aspects of Boersch Phase Contrast Electron Microscopy of Biological Specimens. *Ultramicroscopy* **116,** 62–72 (May 1, 2012).

62. Alloyeau, D., Hsieh, W. K., Anderson, E. H., Hilken, L., Benner, G., Meng, X., Chen, F. R. & Kisielowski, C. Imaging of Soft and Hard Materials Using a Boersch Phase Plate in a Transmission Electron Microscope. *Ultramicroscopy. Hannes Lichte 65th Birthday* **110,** 563–570 (Apr. 1, 2010).

63. Frindt, N., Oster, M., Hettler, S., Gamm, B., Dieterle, L., Kowalsky, W., Gerthsen, D. & Schröder, R. R. In-Focus Electrostatic Zach Phase Plate Imaging for Transmission Electron Microscopy with Tunable Phase Contrast of Frozen Hydrated Biological Samples. *Microscopy and Microanalysis* **20.** 00016, 175–183 (Feb. 2014).

64. Edgcombe, C. J., Ionescu, A., Loudon, J. C., Blackburn, A. M., Kurebayashi, H. & Barnes, C. H. W. Characterisation of Ferromagnetic Rings for Zernike Phase Plates Using the Aharonov–Bohm Effect. *Ultramicroscopy* **120.** 00019, 78–85 (Sept. 1, 2012).
65. Tavabi, A. H., Beleggia, M., Migunov, V., Savenko, A., Öktem, O., Dunin-Borkowski, R. E. & Pozzi, G. Tunable Ampere Phase Plate for Low Dose Imaging of Biomolecular Complexes. *Scientific Reports* **8.** 00000, 5592 (Apr. 4, 2018).
66. Tran, C. Q., Peele, A. G., Roberts, A., a Nugent, K., Paterson, D. & McNulty, I. X-Ray Imaging: A Generalized Approach Using Phase-Space Tomography. *J. Opt. Soc. Am. A. Opt. Image Sci. Vis.* **22.** 00000, 1691–700 (Aug. 2005).
67. Coene, W., Janssen, G., de Beeck, M. & Dyck, D. V. Phase Retrieval through Focus Variation for Ultra-Resolution in Field-Emission Transmission Electron Microscopy. *Phys. Rev. Lett.* **69** (1992).
68. Kawasaki, T., Takai, Y., Ikuta, T. & Shimizu, R. Wave Field Restoration Using Three-Dimensional Fourier Filtering Method. *Ultramicroscopy* **90.** 00042, 47–59 (Dec. 1, 2001).
69. Allen, L. J., McBride, W., O'Leary, N. L. & Oxley, M. P. Exit Wave Reconstruction at Atomic Resolution. *Ultramicroscopy* **100,** 91–104 (July 2004).
70. Kirkland, A. I. & Meyer, R. R. "Indirect" High-Resolution Transmission Electron Microscopy: Aberration Measurement and Wavefunction Reconstruction. *Microscopy and Microanalysis* **10.** 00076, 401–413 (Aug. 2004).
71. Hsieh, W.-K., Chen, F.-R., Kai, J.-J. & Kirkland, A. I. Resolution Extension and Exit Wave Reconstruction in Complex HREM. *Ultramicroscopy. Festschrift in Honor of the 70th Birthday of Professor Fang-Hua Li* **98.** 00063, 99–114 (Jan. 1, 2004).
72. Tillmann, K., Thust, A. & Urban, K. Spherical Aberration Correction in Tandem with Exit-Plane Wave Function Reconstruction: Interlocking Tools for the Atomic Scale Imaging of Lattice Defects in GaAs. *Microscopy and Microanalysis* **10.** 00053, 185–198 (Apr. 2004).
73. Dietrich, J., Abou-Ras, D., Schmidt, S. S., Rissom, T., Unold, T., Cojocaru-Mirédin, O., Niermann, T., Lehmann, M., Koch, C. T. & Boit, C. Origins of Electrostatic Potential Wells at Dislocations in Polycrystalline Cu(In,Ga)Se2 Thin Films. *Journal of Applied Physics* **115.** 00018, 103507 (Mar. 11, 2014).
74. Seldin, J. H. & Fienup, J. R. Numerical Investigation of the Uniqueness of Phase Retrieval. *J. Opt. Soc. Am. A, JOSAA* **7.** 00092, 412–427 (Mar. 1, 1990).

75. Allen, L. J., Faulkner, H. M. L., Nugent, K. A., Oxley, M. P. & Paganin, D. Phase Retrieval from Images in the Presence of First-Order Vortices. *Phys. Rev. E* **63.** 00074, 037602 (Feb. 27, 2001).

76. Martin, a. V., Chen, F.-R., Hsieh, W.-K., Kai, J.-J., Findlay, S. D. & Allen, L. J. Spatial Incoherence in Phase Retrieval Based on Focus Variation. *Ultramicroscopy* **106.** 00040, 914–24 (2006).

77. Kawasaki, T., Endo, J., Matsuda, T., Osakabe, N. & Tonomura, A. Applications of Holographic Interference Electron Microscopy to the Observation of Biological Specimens. *J Electron Microsc (Tokyo)* **35.** 00015, 211–214 (Oct. 1, 1986).

78. Aoyama, K., Lai, G. & Ru, Q. Electron Holographic Observation of Thin Biological Filaments. *J Electron Microsc (Tokyo)* **43.** 00009, 39–41 (Feb. 1, 1994).

79. Bates, R. H. T. & Rodenburg, J. M. Sub-Ångström Transmission Microscopy: A Fourier Transform Algorithm for Microdiffraction Plane Intensity Information. *Ultramicroscopy* **31.** 00026, 303–307 (Nov. 1989).

80. Cowley, J. M. Image Contrast in a Transmission Scanning Electron Microscope. *Appl. Phys. Lett.* **15.** 00344, 58–59 (July 15, 1969).

81. Landau, L. D. & Lifshitz, L. M. *Quantum Mechanics: Non-Relativistic Theory* 3 edition. 00013. 689 pp. (Butterworth-Heinemann, Singapore, Jan. 15, 1981).

82. Horstmeyer, R. & Yang, C. A Phase Space Model of Fourier Ptychographic Microscopy. *Opt. Express* **22,** 338 (Jan. 2014).

83. Zheng, G., Horstmeyer, R. & Yang, C. Wide-Field, High-Resolution Fourier Ptychographic Microscopy. *Nature Photonics* **7.** 00553, 739–745 (Sept. 2013).

84. Kirkland, A. I., Saxton, W. O., Chau, K. .-.-L., Tsuno, K. & Kawasaki, M. Super-Resolution by Aperture Synthesis: Tilt Series Reconstruction in CTEM. *Ultramicroscopy* **57.** 00134, 355–374 (Mar. 1, 1995).

85. Haigh, S. J., Sawada, H. & Kirkland, A. I. Atomic Structure Imaging Beyond Conventional Resolution Limits in the Transmission Electron Microscope. *Phys. Rev. Lett.* **103.** 00028, 126101 (Sept. 17, 2009).

86. Liberti, E., Martinez, G., O'Leary, C., Nellist, P. & Kirkland, A. Phase Retrieval Quantitative Comparison Between Tilt-Series Imaging in TEM and Position-Resolved Coherent Diffractive Imaging in STEM. *Microscopy and Microanalysis* **23.** 00000, 470–471 (July 2017).

87. Shan, M., Liu, L., Zhong, Z., Liu, B., Luan, G. & Zhang, Y. Single-Shot Dual-Wavelength off-Axis Quasi-Common-Path Digital Holography Using Polarization-Multiplexing. *Opt. Express, OE* **25.** 00003, 26253–26261 (Oct. 16, 2017).

88. Wang, Z., Jiang, Z. & Chen, Y. Single-Shot Dual-Wavelength Phase Reconstruction in off-Axis Digital Holography with Polarization-Multiplexing Transmission. *Appl. Opt., AO* **55.** 00003, 6072–6078 (Aug. 1, 2016).

89. Houdellier, F., Caruso, G. M., Weber, S., Kociak, M. & Arbouet, A. Development of a High Brightness Ultrafast Transmission Electron Microscope Based on a Laser-Driven Cold Field Emission Source. *Ultramicroscopy* **186.** 00009, 128–138 (Mar. 1, 2018).

90. Feist, A., Bach, N., Rubiano da Silva, N., Danz, T., Möller, M., Priebe, K. E., Domröse, T., Gatzmann, J. G., Rost, S., Schauss, J., Strauch, S., Bormann, R., Sivis, M., Schäfer, S. & Ropers, C. Ultrafast Transmission Electron Microscopy Using a Laser-Driven Field Emitter: Femtosecond Resolution with a High Coherence Electron Beam. *Ultramicroscopy. 70th Birthday of Robert Sinclair and 65th Birthday of Nestor J. Zaluzec PICO 2017 – Fourth Conference on Frontiers of Aberration Corrected Electron Microscopy* **176.** 00058, 63–73 (May 1, 2017).

91. Zhang, F., Chen, B., Morrison, G. R., Vila-Comamala, J., Guizar-Sicairos, M. & Robinson, I. K. Phase Retrieval by Coherent Modulation Imaging. *Nature Communications* **7.** 00000, 13367 (Nov. 18, 2016).

92. Zhang, F. & Rodenburg, J. M. Phase Retrieval Based on Wave-Front Relay and Modulation. *Phys. Rev. B* **82.** 00008, 121104 (Sept. 20, 2010).

93. Pan, X., Liu, C. & Zhu, J. Single Shot Ptychographical Iterative Engine Based on Multi-Beam Illumination. *Appl. Phys. Lett.* **103.** doi:`10.1063/1.4826273` (2013).

94. Chen, B. K., Sidorenko, P., Lahav, O., Peleg, O. & Cohen, O. *Multiplexed Single-Shot Ptychography* in *Imaging and Applied Optics 2018 (3D, AO, AIO, COSI, DH, IS, LACSEA, LS&C, MATH, pcAOP) (2018), Paper JTh3A.2* Computational Optical Sensing and Imaging. 00000 (Optical Society of America, June 25, 2018), JTh3A.2. doi:`10.1364/3D.2018.JTh3A.2`.

95. Sidorenko, P. & Cohen, O. Single-Shot Ptychography. *Optica, OPTICA* **3.** 00000, 9–14 (Jan. 20, 2016).

96. Pelz, P. M., Qiu, W. X., Bücker, R., Kassier, G. & Miller, R. J. D. Low-Dose Cryo Electron Ptychography via Non-Convex Bayesian Optimization. *Scientific Reports* **7.** 00001, 9883 (Aug. 29, 2017).

97. Marchesini, S., Tu, Y.-C. & Wu, H.-T. Alternating Projection, Ptychographic Imaging and Phase Synchronization. *Applied and Computational Harmonic Analysis* **41.** 00037, 815–851 (Nov. 1, 2016).

98. Thibault, P., Dierolf, M., Menzel, A., Bunk, O., David, C. & Pfeiffer, F. High-Resolution Scanning x-Ray Diffraction Microscopy. *Science* **321.** 00619, 379–82 (July 2008).

99. Maiden, A. M. & Rodenburg, J. M. An Improved Ptychographical Phase Retrieval Algorithm for Diffractive Imaging. *Ultramicroscopy* **109,** 1256–62 (Sept. 2009).

100. Godard, P., Allain, M., Chamard, V. & Rodenburg, J. Noise Models for Low Counting Rate Coherent Diffraction Imaging. *Opt. Express* **20.** 00024, 25914–34 (Nov. 2012).

101. Pelz, P. M., Guizar-Sicairos, M., Thibault, P., Johnson, I., Holler, M. & Menzel, A. On-the-Fly Scans for X-Ray Ptychography. *Appl. Phys. Lett.* **105.** 00011, 251101 (Dec. 22, 2014).

102. Thibault, P. & Guizar-Sicairos, M. Maximum-Likelihood Refinement for Coherent Diffractive Imaging. *New J. Phys.* **14.** 00081, 063004 (June 2012).

103. Chang, H., Enfedaque, P. & Marchesini, S. Blind Ptychographic Phase Retrieval via Convergent Alternating Direction Method of Multipliers. 00000. arXiv: `1808.05802 [eess, math]` (Aug. 17, 2018).

104. Fannjiang, A. & Zhang, Z. Blind Ptychography by Douglas-Rachford Splitting. 00001 (Aug. 26, 2018).

105. Jaganathan, K., Eldar, Y. C. & Hassibi, B. Phase Retrieval: An Overview of Recent Developments. 00031. arXiv: `1510.07713 [cs, math]` (Oct. 26, 2015).

106. Shechtman, Y., Eldar, Y., Cohen, O., Chapman, H., Miao, J. & Segev, M. Phase Retrieval with Application to Optical Imaging: A Contemporary Overview. *IEEE Signal Processing Magazine* **32.** 00016, 87–109 (May 2015).

107. Sun, J., Qu, Q. & Wright, J. *A Geometric Analysis of Phase Retrieval* in *2016 IEEE International Symposium on Information Theory (ISIT)* 2016 IEEE International Symposium on Information Theory (ISIT). 00043 (July 2016), 2379–2383. doi:`10.1109/ISIT.2016.7541725`.

108. Katkovnik, V. & Astola, J. Sparse Ptychographical Coherent Diffractive Imaging from Noisy Measurements. *J. Opt. Soc. Am. A. Opt. Image Sci. Vis.* **30.** 00004, 367–79 (2013).

109. Danielyan, A., Katkovnik, V. & Egiazarian, K. BM3D Frames and Variational Image Deblurring. *IEEE Transactions on Image Processing* **21.** 00196, 1715–1728 (Apr. 2012).

110. Yang, H., Ercius, P., Nellist, P. D. & Ophusa, C. Enhanced Phase Contrast Transfer Using Ptychography Combined with a Pre-Specimen Phase Plate in a Scanning Transmission Electron Microscope. *Ultramicroscopy.* 00001. doi:`10.1016/j.ultramic.2016.09.002`.

111. Li, P., Edo, T. B. & Rodenburg, J. M. Ptychographic Inversion via Wigner Distribution Deconvolution: Noise Suppression and Probe Design. *Ultramicroscopy* **147.** 00007, 106–113 (Dec. 2014).

112. Thibault, P. & Menzel, A. Reconstructing State Mixtures from Diffraction Measurements. *Nature* **494.** 00000, 68–71 (Feb. 2013).

113. Chang, H. & Marchesini, S. A General Framework for Denoising Phaseless Diffraction Measurements. 00001 (Nov. 2, 2016).

114. Katkovnik, V., Ponomarenko, M. & Egiazarian, K. Complex-Valued Image Denosing Based on Group-Wise Complex-Domain Sparsity. 00000 (Nov. 1, 2017).

115. Chen, Y. & Candes, E. J. Solving Random Quadratic Systems of Equations Is Nearly as Easy as Solving Linear Systems. 00021 (May 19, 2015).

116. Shewchuk, J. R. *An Introduction to the Conjugate Gradient Method Without the Agonizing Pain* 00000 (Carnegie Mellon University, Pittsburgh, PA, USA, 1994).

117. *Torch.Optim* 00000.

118. Mises, R. V. & Pollaczek-Geiringer, H. Praktische Verfahren Der Gleichungsauflösung . *Z. angew. Math. Mech.* **9.** 00185, 152–164 (Jan. 1, 1929).

119. Lehoucq, R., Sorensen, D. & Yang, C. *ARPACK Users' Guide: Solution of Large-Scale Eigenvalue Problems with Implicitly Restarted Arnoldi Methods* 02150 (Society for Industrial and Applied Mathematics (SIAM, 3600 Market Street, Floor 6, Philadelphia, PA 19104), 1998).

120. Sawada, H., Sannomiya, T., Hosokawa, F., Nakamichi, T., Kaneyama, T., Tomita, T., Kondo, Y., Tanaka, T., Oshima, Y., Tanishiro, Y. & Takayanagi, K. Measurement Method of Aberration from Ronchigram by Autocorrelation Function. *Ultramicroscopy* **108.** 00061, 1467–1475 (Oct. 1, 2008).

121. Thibault, P., Dierolf, M., Bunk, O., Menzel, A. & Pfeiffer, F. Probe Retrieval in Ptychographic Coherent Diffractive Imaging. *Ultramicroscopy* **109,** 338–43 (Mar. 2009).

122. Cao, S., Kok, P., Li, P., Maiden, A. M. & Rodenburg, J. M. Modal Decomposition of a Propagating Matter Wave via Electron Ptychography. *Phys. Rev. A* **94.** 00010, 063621 (Dec. 19, 2016).

123. Fermi, G., Perutz, M. F., Shaanan, B. & Fourme, R. The Crystal Structure of Human Deoxyhaemoglobin at 1.74 A Resolution. *J. Mol. Biol.* **175.** 00000 PMID: 6726807, 159–174 (May 15, 1984).

124. Groll, M., Ditzel, L., Löwe, J., Stock, D., Bochtler, M., Bartunik, H. D. & Huber, R. Structure of 20S Proteasome from Yeast at 2.4Å Resolution. *Nature* **386.** 02142, 463–471 (Apr. 3, 1997).

125. Anger, A. M., Armache, J.-P., Berninghausen, O., Habeck, M., Subklewe, M., Wilson, D. N. & Beckmann, R. Structures of the Human and Drosophila 80S Ribosome. *Nature* **497.** 00000, 80–85 (May 2, 2013).

126. McMullan, G., Faruqi, A. R., Clare, D. & Henderson, R. Comparison of Optimal Performance at 300 keV of Three Direct Electron Detectors for Use in Low Dose Electron Microscopy. *Ultramicroscopy* **147.** 00000 arXiv: 1406.1389, 156–163 (Dec. 2014).

127. Enders, B., Dierolf, M., Cloetens, P., Stockmar, M., Pfeiffer, F. & Thibault, P. Ptychography with Broad-Bandwidth Radiation. *Appl. Phys. Lett.* **104.** 00019, 171104 (Apr. 2014).

128. Ryll, H., Simson, M., Hartmann, R., Holl, P., Huth, M., Ihle, S., Kondo, Y., Kotula, P., Liebel, A., K. Müller-Caspary, Rosenauer, A., Sagawa, R., Schmidt, J., Soltau, H. & Strüder, L. A pnCCD-Based, Fast Direct Single Electron Imaging Camera for TEM and STEM. *J. Inst.* **11.** 00003, P04006 (2016).

129. Tate, M. W., Purohit, P., Chamberlain, D., Nguyen, K. X., Hovden, R., Chang, C. S., Deb, P., Turgut, E., Heron, J. T., Schlom, D. G., Ralph, D. C., Fuchs, G. D., Shanks, K. S., Philipp, H. T., Muller, D. A. & Gruner, S. M. High Dynamic Range Pixel Array Detector for Scanning Transmission Electron Microscopy. *Microscopy and Microanalysis* **22.** 00027, 237–249 (Feb. 2016).

130. Stark, H., Zemlin, F. & Boettcher, C. Electron Radiation Damage to Protein Crystals of Bacteriorhodopsin at Different Temperatures. *Ultramicroscopy* **63.** 00060, 75–79 (June 1, 1996).

131. Heel, M. V. & Schatz, M. Fourier Shell Correlation Threshold Criteria Q. *J. Struct. Biol.* **151.** 00000, 250–262 (2005).

132. Scheres, S. H. W. RELION: Implementation of a Bayesian Approach to Cryo-EM Structure Determination. *Journal of Structural Biology* **180.** 00587, 519–530 (Dec. 2012).

133. Tang, G., Peng, L., Baldwin, P. R., Mann, D. S., Jiang, W., Rees, I. & Ludtke, S. J. EMAN2: An Extensible Image Processing Suite for Electron Microscopy. *Journal of Structural Biology. Software tools for macromolecular microscopy* **157.** 01132, 38–46 (Jan. 2007).

134. Dierolf, M., Menzel, A., Thibault, P., Schneider, P., Kewish, C. M., Wepf, R., Bunk, O. & Pfeiffer, F. Ptychographic X-Ray Computed Tomography at the Nanoscale. *Nature* **467.** 00387, 436–439 (2010).

135. Crowther, R. A., DeRosier, D. J. & Klug, A. The Reconstruction of a Three-Dimensional Structure from Projections and Its Application to Electron Microscopy. *Proc. R. Soc. Lond. A* **317.** 01009, 319–340 (June 23, 1970).

136. Paszke, A., Gross, S., Chintala, S., Chanan, G., Yang, E., DeVito, Z., Lin, Z., Desmaison, A., Antiga, L. & Lerer, A. *Automatic Differentiation in PyTorch* in *NIPS-W* 00361 (2017).

137. Abadi, M., Agarwal, A., Barham, P., Brevdo, E., Chen, Z., Citro, C., Corrado, G. S., Davis, A., Dean, J., Devin, M., Ghemawat, S., Goodfellow, I., Harp, A., Irving, G., Isard, M., Jia, Y., Jozefowicz, R., Kaiser, L., Kudlur, M., Levenberg, J., Mané, D., Monga, R., Moore, S., Murray, D., Olah, C., Schuster, M., Shlens, J., Steiner, B., Sutskever, I., Talwar, K., Tucker, P., Vanhoucke, V., Vasudevan, V., Viégas, F., Vinyals, O., Warden, P., Wattenberg, M., Wicke, M., Yu, Y. & Zheng, X. TensorFlow: Large-Scale Machine Learning on Heterogeneous Systems. 00038 Software available from tensorflow.org (2015).

138. Williams, D. B. & Carter, C. B. *Transmission Electron Microscopy: A Textbook for Materials Science* 00003. 760 pp. (2009).

139. Chapman, H. N., Barty, A., Marchesini, S., Noy, A., Hau-Riege, S. P., Cui, C., Howells, M. R., Rosen, R., He, H., Spence, J. C. H., Weierstall, U., Beetz, T., Jacobsen, C. & Shapiro, D. High-Resolution Ab Initio Three-Dimensional x-Ray Diffraction Microscopy. *J. Opt. Soc. Am. A. Opt. Image Sci. Vis.* **23.** 00000, 1179–1200 (Sept. 2006).

140. Tsai, E. H. R., Usov, I., Diaz, A., Menzel, A. & Guizar-Sicairos, M. X-Ray Ptychography with Extended Depth of Field. *Opt. Express, OE* **24.** 00000, 29089–29108 (Dec. 12, 2016).

141. Maiden, a. M., Humphry, M. J. & Rodenburg, J. M. Ptychographic Transmission Microscopy in Three Dimensions Using a Multi-Slice Approach. *J. Opt. Soc. Am. A. Opt. Image Sci. Vis.* **29.** 00062, 1606–14 (Aug. 2012).

142. Gao, S., Wang, P., Zhang, F., Martinez, G. T., Nellist, P. D., Pan, X. & Kirkland, A. I. Electron Ptychographic Microscopy for Three-Dimensional Imaging. *Nature Communications* **8.** 00000. doi:`10.1038/s41467-017-00150-1` (2017).

143. Russo, C. J. & Henderson, R. Ewald Sphere Correction Using a Single Side-Band Image Processing Algorithm. *Ultramicroscopy* **187.** 00007, 26–33 (Apr. 1, 2018).

144. Zhu, D., Wang, X., Fang, Q., Etten, J. L., Rossmann, M. G., Rao, Z. & Zhang, X. Pushing the Resolution Limit by Correcting the Ewald Sphere Effect in Single-Particle Cryo-EM Reconstructions. *Nature Communications* **9.** 00000, 1552 (Apr. 19, 2018).

145. Tan, Y. Z., Aiyer, S., Mietzsch, M., Hull, J. A., McKenna, R., Grieger, J., Samulski, R. J., Baker, T. S., Agbandje-McKenna, M. & Lyumkis, D. Sub-2 Å Ewald Curvature Corrected Single-Particle Cryo-EM. *bioRxiv.* 00001, 305599 (Apr. 21, 2018).

146. Bunk, O., Dierolf, M., Kynde, S., Johnson, I., Marti, O. & Pfeiffer, F. Influence of the Overlap Parameter on the Convergence of the Ptychographical Iterative Engine. *Ultramicroscopy* **108.** 00138, 481–487 (Apr. 1, 2008).

147. Edo, T. B., Batey, D. J., Maiden, a. M., Rau, C., Wagner, U., P si , Z. D., a. Waigh, T. & Rodenburg, J. M. Sampling in X-Ray Ptychography. *Phys. Rev. A* **87.** 00018, 053850 (May 2013).

148. Da Silva, J. C. & Menzel, A. Elementary Signals in Ptychography. *Opt. Express, OE* **23.** 00000, 33812–33821 (Dec. 28, 2015).

149. Miao, J., Sayre, D. & Chapman, H. N. Phase Retrieval from the Magnitude of the Fourier Transforms of Nonperiodic Objects. *J. Opt. Soc. Am. A, JOSAA* **15.** 00552, 1662–1669 (June 1, 1998).

150. Batey, D. J., Edo, T. B., Rau, C., Wagner, U., Peši , Z. D., Waigh, T. A. & Rodenburg, J. M. Reciprocal-Space up-Sampling from Real-Space Oversampling in x-Ray Ptychography. *Phys. Rev. A* **89.** 00029, 043812 (Apr. 9, 2014).

151. Fannjiang, A. Raster Grid Pathology and Other Ptychographic Ambiguities. 00000 (Oct. 1, 2018).

152. Mir, J. A., Clough, R., MacInnes, R., Gough, C., Plackett, R., Shipsey, I., Sawada, H., MacLaren, I., Ballabriga, R., Maneuski, D., O'Shea, V., McGrouther, D. & Kirkland, A. I. Characterisation of the Medipix3 Detector for 60 and 80keV Electrons. *Ultramicroscopy* **182.** 00000, 44–53 (Nov. 1, 2017).

153. Mir, J. A., Plackett, R., Shipsey, I. & dos Santos, J. M. F. Using the Medipix3 Detector for Direct Electron Imaging in the Range 60 keV to 200 keV in Electron Microscopy. *J. Inst.* **12.** 00001, C11015 (2017).

154. Tinti, G., Fröjdh, E., van Genderen, E., Gruene, T., Schmitt, B., Winter, D., M, D. A., Weckhuysen, B. M. & Abrahams, J. P. Electron Crystallography with the EIGER Detector. *IUCrJ* **5.** 00000, 190–199 (Mar. 1, 2018).

155. *Electrons Are the New Photons* 00000.

156. Faruqi, A. R. & McMullan, G. Direct Imaging Detectors for Electron Microscopy. *Nuclear Instruments and Methods in Physics Research Section A: Accelerators, Spectrometers, Detectors and Associated Equipment.* 00000. doi:`10.1016/j.nima.2017.07.037` (Aug. 9, 2017).

157. Putkunz, C. T., D'Alfonso, A. J., Morgan, A. J., Weyland, M., Dwyer, C., Bourgeois, L., Etheridge, J., Roberts, A., Scholten, R. E., a. Nugent, K. & Allen, L. J. Atom-Scale Ptychographic Electron Diffractive Imaging of Boron Nitride Cones. *Phys. Rev. Lett.* **108.** 00027, 073901 (Feb. 2012).

158. Wang, P., Zhang, F., Gao, S., Zhang, M. & Kirkland, A. I. Electron Ptychographic Diffractive Imaging of Boron Atoms in LaB 6 Crystals. *Scientific Reports* **7.** 00009, 2857 (June 6, 2017).

159. D'Alfonso, A. J., Allen, L. J., Sawada, H. & Kirkland, A. I. Dose-Dependent High-Resolution Electron Ptychography. *Journal of Applied Physics* **119.** 00000, 054302 (Feb. 7, 2016).

160. Yang, H., Rutte, R. N., Jones, L., Simson, M., Sagawa, R., Ryll, H., Huth, M., Pennycook, T. J., Green, M. L. H., Soltau, H., Kondo, Y., Davis, B. G. & Nellist, P. D. Simultaneous Atomic-Resolution Electron Ptychography and Z-Contrast Imaging of Light and Heavy Elements in Complex Nanostructures. *Nature Communications* **7.** 00001, 12532 (Aug. 26, 2016).

161. Humphry, M., Kraus, B. & Hurst, A. Ptychographic Electron Microscopy Using High-Angle Dark-Field Scattering for Sub-Nanometre Resolution Imaging. *Nat. ldots* **3.** 00000, 730–737 (2012).

162. Jiang, Y., Chen, Z., Han, Y., Deb, P., Gao, H., Xie, S., Purohit, P., Tate, M. W., Park, J., Gruner, S. M., Elser, V. & Muller, D. A. Electron Ptychography of 2D Materials to Deep Sub-Ångström Resolution. *Nature* **559.** 00000, 343–349 (July 2018).

163. Maiden, A. M., Humphry, M. J., Zhang, F. & Rodenburg, J. M. Superresolution Imaging via Ptychography. *J. Opt. Soc. Am. A. Opt. Image Sci. Vis.* **28,** 604–12 (Apr. 2011).

164. Godden, T. M., Suman, R., Humphry, M. J., Rodenburg, J. M. & Maiden, A. M. Ptychographic Microscope for Three-Dimensional Imaging. *Opt. Express* **22,** 12513–23 (2014).

165. Maiden, A. M., Morrison, G. R., Kaulich, B., Gianoncelli, A. & Rodenburg, J. M. Soft X-Ray Spectromicroscopy Using Ptychography with Randomly Phased Illumination. *Nature Communications* **4.** 00042, 1669 (Apr. 9, 2013).

166. Stockmar, M., Zanette, I., Dierolf, M., Enders, B., Clare, R., Pfeiffer, F., Cloetens, P., Bonnin, A. & Thibault, P. X-Ray Near-Field Ptychography for Optically Thick Specimens. *Phys. Rev. Applied* **3.** 00003, 014005 (Jan. 21, 2015).

167. Li, P., Batey, D. J., Edo, T. B., Parsons, A. D., Rau, C. & Rodenburg, J. M. Multiple Mode X-Ray Ptychography Using a Lens and a Fixed Diffuser Optic. *J. Opt.* **18.** 00001, 054008 (2016).

168. Morrison, G. R., Zhang, F., Gianoncelli, A. & Robinson, I. K. X-Ray Ptychography Using Randomized Zone Plates. *Opt. Express, OE* **26.** 00000, 14915–14927 (June 11, 2018).

169. Ophus, C., Ciston, J., Pierce, J., Harvey, T. R., Chess, J., McMorran, B. J., Czarnik, C., Rose, H. H. & Ercius, P. Efficient Linear Phase Contrast in Scanning Transmission Electron Microscopy with Matched Illumination and Detector Interferometry. *Nat Commun* **7.** 00000, 10719 (Feb. 29, 2016).

170. Harvey, T. R., Pierce, J. S., Agrawal, A. K., Ercius, P., Linck, M. & McMorran, B. J. Efficient Diffractive Phase Optics for Electrons. *New J. Phys.* **16.** 00015, 093039 (2014).

171. *Introduction to Electron Holography* (eds Völkl, E., Allard, L. F. & Joy, D. C.) 00310 (Springer US, 1999).

172. Verbeeck, J., Tian, H. & Schattschneider, P. Production and Application of Electron Vortex Beams. *Nature* **467.** 00410, 301–304 (Sept. 16, 2010).

173. Li, X., Zheng, S. Q., Egami, K., Agard, D. A. & Cheng, Y. Influence of Electron Dose Rate on Electron Counting Images Recorded with the K2 Camera. *J. Struct. Biol.* **184,** 251–260 (2013).

174. Pennycook, T. J., Martinez, G. T., Nellist, P. D. & Meyer, J. C. The Potential for Greater Clarity Cryo-Electron Microscopy via Ptychography. *Microscopy and Microanalysis* **24.** 00000, 878–879 (Aug. 2018).

175. Meo, J. S.-D., Liv, N. & Hoogenboom, J. P. in *Encyclopedia of Analytical Chemistry* 00000, 1–31 (American Cancer Society, 2016). doi:10.1002/9780470027318.a9473.

176. Bernhardt, M., Nicolas, J.-D., Osterhoff, M., Mittelstädt, H., Reuss, M., Harke, B., Wittmeier, A., Sprung, M., Köster, S. & Salditt, T. Correlative Microscopy Approach for Biology Using X-Ray Holography, X-Ray Scanning Diffraction and STED Microscopy. *Nature Communications* **9.** 00000, 3641 (Sept. 7, 2018).

177. Pohl, V., Yang, F. & Boche, H. Phase Retrieval from Low Rate Samples. *arXiv Prepr. arXiv1311.7045,* 1–21 (2013).

178. Carmeli, C., Heinosaari, T., Kech, M., Schultz, J. & Toigo, A. Stable Pure State Quantum Tomography from Five Orthonormal Bases. *EPL* **115.** 00009, 30001 (2016).

179. Carmeli, C., Heinosaari, T., Schultz, J. & Toigo, A. How Many Orthonormal Bases Are Needed to Distinguish All Pure Quantum States? *Eur. Phys. J. D* **69.** 00017, 179 (July 1, 2015).

180. Wang, Y. & Shang, Y. Pure State 'Really' Informationally Complete with Rank-1 POVM. *Quantum Inf Process* **17,** 51 (Mar. 1, 2018).

181. Shlezinger, N., Dabora, R. & Eldar, Y. C. Measurement Matrix Design for Phase Retrieval Based on Mutual Information. 00000 arXiv: 1704.08021. arXiv: `1704.08021 [cs, math]` (Apr. 26, 2017).

182. Shlezinger, N., Dabora, R. & Eldar, Y. C. *Using Mutual Information for Designing the Measurement Matrix in Phase Retrieval Problems* in *2017 IEEE International Symposium on Information Theory (ISIT)* 2017 IEEE International Symposium on Information Theory (ISIT). 00000 (June 2017), 2343–2347. doi:`10.1109/ISIT.2017.8006948`.

183. Bostan, E., Kamilov, U. S. & Waller, L. Learning-Based Image Reconstruction via Parallel Proximal Algorithm. *IEEE Signal Processing Letters* **25,** 989–993 (July 2018).

184. Gregor, K. & Lecun, Y. *Learning Fast Approximations of Sparse Coding* 00399 ().

185. Kobler, E., Klatzer, T., Hammernik, K. & Pock, T. *Variational Networks: Connecting Variational Methods and Deep Learning* in *Pattern Recognition* (eds Roth, V. & Vetter, T.) 00009 (Springer International Publishing, 2017), 281–293.

186. Kellman, M. R., Bostan, E., Repina, N., Lustig, M. & Waller, L. Physics-Based Learned Design: Optimized Coded-Illumination for Quantitative Phase Imaging. 00000. arXiv: `1808.03571 [cs, eess]` (Aug. 10, 2018).

187. Krehl, J., Guzzinati, G., Schultz, J., Potapov, P., Pohl, D., Martin, J., Verbeeck, J., Fery, A., Büchner, B. & Lubk, A. Spectral Field Mapping in Plasmonic Nanostructures with Nanometer Resolution. 00002 (Mar. 12, 2018).

188. Bracewell, R. N. Numerical Transforms. *Science* **248.** 00110, 697–704 (May 11, 1990).

189. in. *Wikipedia* 00001 Page Version ID: 857348431 ().